Nanoparticles for Simultaneous Near-Infrared and Magnetic Biomolecular Imaging

Amir Servati

A Thesis Submitted for the degree of Doctor of Philosophy

University College London

March 2012

Contents

List of Figures

List of Tables

Acknowledgements

First, I would like to thank my supervisors Professor Arokia Nathan, Professor Poopathy Kathirgamanathan and Dr. Stephen Lynch for all their kind guidance, support and advices through my PhD, without which this thesis would not have been possible.

It is a pleasure for me to thank all my colleagues in University College London and Brunel University, who helped me to experience a friendly and unforgettable environment all these years.

Most of all I would like to thank my mother, Mahin Ozgoli, my father, Aliasghar Servati, My brother, Dr. Peyman Servati and my sister, Sara Servati, and all other family members and friends who, as always, support me with their endless love and kindness.

Abstract

Nanoparticle probes can unlock the potential for multimodal biomedical imaging (*in vivo* and *in vitro*) with enhanced spatial resolution and penetration depth and targeted visualization of complex organisms. This thesis demonstrates synthesis and characterization of magnetic upconversion Gd_2O_3 nanoparticles that can serve as bimodal probes for optical imaging in near infrared (NIR) biomedical window, where minimal tissue autofluorescence is expected, as well as magnetic resonance imaging. More specifically, Gd_2O_3:Yb^{3+},Tm^{3+} and Gd_2O_3:Yb^{3+},Er^{3+} nanoparticles are synthesized using urea-based homogeneous precipitation method (UHP) as well as Y_2O_3:Yb^{3+}/Er^{3+} micro and nanoparticles using conventional combustion and thermal synthesis methods. The morphological and compositional properties of nanoparticles as well as their photonic and magnetic responses are systematically analyzed to understand the role of synthesis methods and initial synthesis materials including the concentrations of Tm and Er dopants and urea solution on the properties of the synthesized particles. The upconversion nanoparticles synthesized using UHP method are spherical and monodisperse with a size distribution in the range of 60 to 150 nm and controllable dopant concentration through manipulation of initial synthesis chemistry. When excited with 975 nm NIR radiation, Gd_2O_3:Yb^{3+},Tm^{3+} nanoparticles show a pure near infrared emission centered at around 810 nm (i.e., NIR-to-NIR upconversion) in NIR biological window with potential for high depth optical imaging while Er^{3+} doped particles emit light mainly in visible

red centred at around 661 nm. The photoluminescence and transient optical decay measurements demonstrate distinctly different energy transfer mechanisms for Er and Tm doped samples. While these measurements signify a dominant role for Yb^{3+} dopants in strong upconversion emission of Tm^{3+} samples with a double exponential decay behaviour, they show less important role of Yb^{3+} in Er^{3+} samples with a single exponential decay. Systematic magnetic characterization demonstrate strong paramagnetic behaviour for the optically active upconversion nanoparticles, demonstrating their potential for bimodal optical and magnetic resonant imaging.

Chapter 1

Introduction

1.1 Opportunities for Molecular Imaging in Nanomedicine

Molecular imaging is the ability to visualize biological, physiological and pathological processes by non-invasive acquisition of quantitative temporal images of a target of interest (often enhanced by using targeted nanoparticles) in a culture medium (*in vitro*) or living conditions (*in vivo*) [20]. Although conventional medical imaging methods provide anatomical information that is important to diagnosis, surgical guidance, and treatment monitoring, they suffer from lack of sensitivity and specificity to specific target areas, resulting in wrong diagnosis, high percentage of false positives or negatives and limited success in early detection. Recent advances in genomics, proteomics, biotechnology, nanomedicine, molecular biology and biochemistry have resulted in the opportunity to significantly enrich conventional anatomical images with targeted functional molec-

ular imaging of tissues and cells. These advances provide a pathway for much-needed improved sensitivity and specificity and have been investigated for several conventional modalities such as X-ray imaging, magnetic resonant imaging (MRI), computed tomography (CT), positron emission tomography (PET), single-photon emission computed tomography (SPECT), Ultrasound (US), photoacoustic imaging and optical imaging, which will be summarized in more details in part 1.2 of this thesis[21, 22, 31]. Advantages of molecular imaging are independent of the modality and include early non-invasive detection of diseased tissues and cells, functional monitoring of therapeutic effects on cells in patient or animal models, improving the ability to investigate cell processes and interactions *in vivo*, targeted drug delivery for more effective treatments with less adverse effects, and whole-body safe molecular imaging.

Synthetic nanoparticles play a critical role in enabling targeted molecular imaging in the field of "nanomedicine"; although since almost all interactions that occur in human biology is at nanoscale, one can easily argue that all medicine is "nanomedicine". Figure 1.1 illustrates the size of biological elements is in micro/nano scale, signifying the role of nanoparticles and nanostructures for interactions in medical and biological processes. Nanomedicine is defined as the application of novel synthetic nanostructures for improving our ability to diagnose and treat diseases [32].

New applications of nanotechnology in medicine are being introduced every day, which have the potential to revolutionize the medical and pharmaceutical sciences. Examples of these applications include: (i) Nanoparticles are used

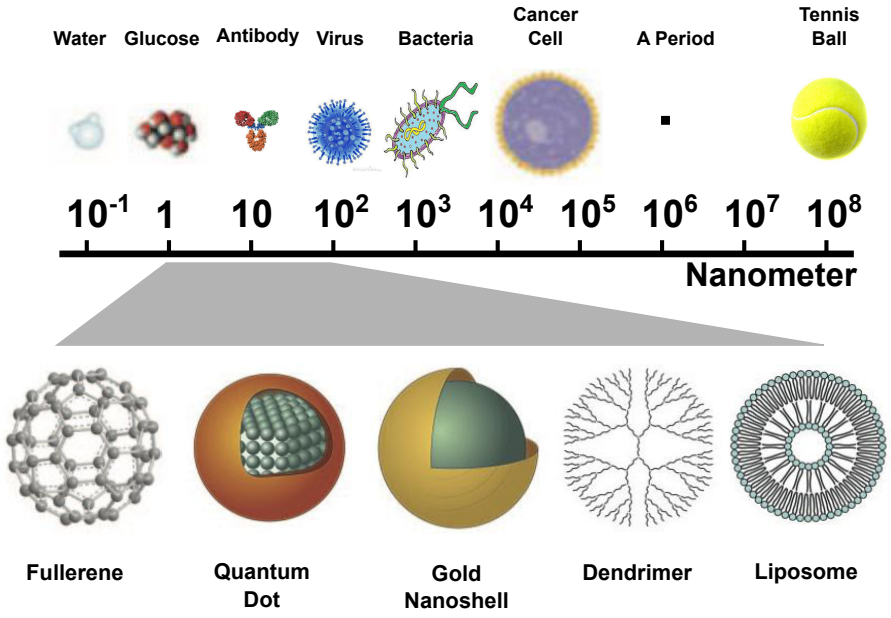

Figure 1.1: Schematic diagram for comparison of the size of synthetic nanoparticles and other familiar building blocks of human biology [1].

as targeted detection agents, as targeted carriers of therapeutic materials and drugs, and targeted contrasts agents in tissues. The small size of these particles allow their transfer through biological barriers such as blood brain barriers. (ii) The ability to acquire quantitative information from biological and physiological processes *in vitro* or *in vivo* can dramatically enhance our understanding about the these complex system of processes involved in healthy and diseased tissues and organisms. (iii) Engineered nanostructures can be used in targeted regenerative medicine, tissue engineering and wound healing. (iv) There is a significant potential to enhance specificity and reduce delay in diagnosis by transferring our paraclinical abilities to small, affordable and mobile electronic chips that can be used in remote areas even by amateur users. (v) The ability to perform complex biological experiments on small scale and with improved

resolution has an overreaching potential for cost saving in research and development for a more efficient pharmaceutical industry. (vi) All these advantages can play a revolutionary role in medicine in future to change the "one-size-fits-all" approach in medicine toward more patient-specific methods known as "personalized medicine" [33].

1.2 Molecular Imaging Modalities

Classification of the modalities of molecular imaging methods are based on energy and modality of the (externally excited or self emitting) imaging agent or probe used for detection of a target of interest. Table 1.1 summarizes these modalities and common probes, as well as their advantages and disadvantages. Currently, molecular imaging is mostly performed using nuclear imaging such as PET or SPECT. Optical and US imaging methods are real-time, inexpensive and safe, but these methods need advances in technological aspects of nanoparticles probes, detectors and instrumentations. Considering the imperfections of each modality in providing resolution, specificity and sensitivity, an efficient and practical molecular imaging may be achieved by using more than one modality (i.e., multimodality) for one investigation.

Nuclear imaging (e.g., PET and SPECT) is the most popular molecular imaging modality currently used in clinical applications. Gamma-ray emitting particles circulate in body generate the required contrast when aggregate on the desired target with no need for an external excitation source and unlim-

ited penetration depth. Extremely sensitive imaging has been demonstrated by PET/SPECT for detection of radionuclides with concentration as small as 10^{-11} moles/L, equivalent to detection of a single cell by only two to three labelled antibody molecules [34]. Nuclear imaging modalities have been combined with CT or MRI for multimodal imaging, so as to have anatomical and molecular information simultaneously with functional images provided by PET/SPECT. SPECT has been also merged with some treatments methods such as radiotherapy for guided treatments. Nuclear modality suffers from disadvantages such as: (1) limited spatial resolution (1 mm) which is determined by the resolution of detector and imaging system, (2) poor anatomical resolution, (3) exposure of tissues to radiation, particularly with potential for high radiation damage to kidneys because of the pharmacokinetics, (4) long acquisition time (minutes to hours), and (5) the required direct or indirect access to a cyclotron facility for PET [22].

Magnetic resonant imaging and spectroscopy (MRI and MRS) are widely used in clinical imaging in view of their high spatial resolution. The resolution of MRI is dependent on the strength of the magnetic field; a 3 T magnetic source commonly used in most MRI centres provides a millimeter resolution. A more powerful magnetic sources such as 5-8 T improve the resolution of MRI for smaller samples by increasing the signal to noise ratio [35], as an example using a 8 T MRI enable imaging with resolution of less than 100 μm from brain tissue *in vitro* [36]. Other factors determining spatial and contrast resolution of MRI include imaging sequence and signal sampling rate [22]. In addition to having a high resolution, MRI has a deep tissue penetration depth, no exposure

to radiation, possibility of whole body imaging and excellent soft-tissue contrast. One of the most important drawbacks of MRI, especially for molecular imaging application, is its low sensitivity. The detection limit of gadolinium in MRI is 10^{-5} moles/L, while detection limit is 10^{-11} for PET/SPECT and 10^{-8} in optical imaging [37]. This low sensitivity also leads to slow data acquisition (approximately an hour for a good quality image). New technologies like chemical exchange saturation transfer (CEST) and paramagnetic chemical exchange saturation transfer (PARA-CEST) are expected to enhance the sensitivity of MRI [38, 39]. Another important drawback of MRI for molecular imaging is the cost and availability of MRI systems. Magnetic nanoparticles have the potential for playing a critical role in addressing these drawbacks for magnetic modality in molecular imaging as discussed in Section 1.4 of this thesis.

Historically, a major turning point in medical imaging has been the invention of X-ray and its usage in computed tomography (CT) scan for clinical diagnosis applications. Unlike X-ray imaging, in CT scan the source rotates around the sample to provide a 3 dimensional (3D) replication of the sample. Advantages of CT scan includes high spatial resolution (1-2 mm) [40], high penetration depth, possibility for whole body imaging, fast data acquisition and high quality anatomical data. Disadvantages of CT scans are exposure to high level of X-ray radiation, low sensitivity, poor soft tissue contrast and resolution and being moderately expensive. Due to the presence of these disadvantages and lack of proper imaging probes, application of CT in molecular imaging is very limited at the moment. The effective resolution of an X-ray image is limited by the hardware, object size and object geometry and can be improved by using

Table 1.1: Advantages, disadvantages, energy range and commont contrast probes for different modalities of molecular imaging [20, 21, 22, 23].

Imaging modality	Detection energy	Common contrasts	Advantages	Disadvantages
Positron emission tomography (PET)	Gamma-rays	^{11}C, ^{18}F, ^{64}Cu, ^{68}Ga, ^{18}FDG and ^{15}H2O	High sensitivity Unlimited depth penetration Whole body imaging possible Can be combined with MRI or CT for anatomical data	Low spatial resolution (1-2mm; 4-8 mm^3) Need access to cyclotron Radiation exposure Long acquisition time (min-hours)
Single photon emission computed tomography (SPECT)	Gamma-rays	^{99m}TC, ^{123}I, ^{111}In and ^{177}Lu	High sensitivity Unlimited depth penetration Whole body imaging Theranostic(can combined imaging and radiotherapy) Can combined with CT or MRI for anatomical data	Low spatial resolution (0.3-1mm, 12-15 mm^3) Radiation exposure Long acquisition time (min-hours)
Magnetic resonance imaging (MRI)	Magnetic field	Gadolinium (Gd^{3+}), Iron oxide particles (SPIO, USPIO), Manganese oxide and ^{19}F	High spatial resolution (<1mm) Deep tissue imaging No exposure to radiation whole body imaging possible Excellent soft-tissue contrast	Low sensitivity Slow data acquisition (min-hours) Expensive
Magnetic resonance spectroscopy (MRS)	Magnetic field	Choline,Creatine,Lactate, Lipids, Polyamines and N-acetyl-aspartate	Whole body imaging possible No ionizing radiation	Expensive Long data acquisition (min-hours) Low sensitivity
Ultrasound (US)	Ultrasonic waves	Contrast microbubbles	High spatial resolution Low cost No ionizing radiation Real time imaging Highly sensitive	whole body imaging not possible Limited to vasculature for molecular imaging Operator dependant
Computed tomography (CT)	X-ray	Barium, Iodine, krypton and xenon	High resolution Unlimited tissue depth penetration Whole-body imaging possible Short data acquisition (minutes) Provide anatomical images	Radiation exposure Low sensitivity Poor soft tissues contrast Moderately expensive limited applications in molecular imaging
Optical imaging	Light	Fluorescence molecules and dyes Light absorbing nanoparticles (gold nanoparticles, QDs)	No ionizing irradiation Real-time imaging/short acquisition time (min) Relatively high spatial resolution Can be applied externally and internally (endoscopic) Inexpensive Highly quantitative and sensitive Can be applied in multimodality	Limited depth penetration ($\leq 1cm$) Whole body imaging not possible Low signal to noise ratio because of autofluorescence

flat panel detectors and gold nanoparticles as contrast agents [41].

Two other modalities, which can be named as the safest amongst other modalities, are optical and ultrasound (US). Optical modality will be described in the next section. Ultrasound is one of the safest methods in medical imaging as it uses propagation of low intensity ultrasonic waves. Advantages of US imaging include high spatial resolution, low cost, non-ionizing radiation, real-time imaging and high sensitivity. However, for ultrasound, whole body scans are not possible and the quality of the imaging is highly dependent on the experience of the operator. The resolution of ultrasound imaging is dependent on the frequency (usually 5-15 MHz) [42]. Nanoparticles have not been able to play an important role for improving performance for this modality, since for detecting particles with the size in the range of less than 1000 nm, frequency of the ultrasound wave must increase to more than 30 MHz with a tissue penetration depth of a few millimeters [22]. The application of US for molecular imaging is just limited to detecting intravascular targets by using microbubbles, usually more than 5 μm in diameter, as the imaging contrast.

1.3 Optical Modality

It is possible to argue that the first experience of molecular imaging was performed in the field of histology and pathology by using simple haematoxylin and eosin (H&E) staining in light microscopy, which has revolutionized medical pathology and is still one of the main methods used. H&E enables detection of

molecules inside tissue cultures according to their affinity to these two dyes. The capabilities in optical microscopy have improved radically by novel approaches in biotechnology and optical instrumentation such as indirect labelling using antibodies, availability of monoclonal antibodies, antibody fragments, enzyme tracers, confocal scanning laser microscopy and two-photon microscopy. These techniques combined with new advances in optical nanoparticles revive the role of optical modality for *in vitro* and *in vivo* imaging. An example for this revival is the possibility to view specific targets in living cells at high spatial and temporal resolution (sub-micrometer, microseconds) and to track them for days without any significant damage to the cells [22].

Optical imaging is a versatile, non-invasive imaging method, where quantitative contrast can be generated through modulation of intensity, wavelength, polarization, coherence, interferences, lifetime and nonlinear effects. Advantages of optical modality include: (1) non-ionizing radiation, (2) fast data acquisition (minutes), (3) possibility of real-time imaging, (4) relatively high spatial resolution, (5) miniaturization for internal use on endoscopes, (6) highly quantitative and sensitive (as low as 10^{-8} moles/L) and (7) possibility of multimodality by simultaneous optical and for example MRI. In spite of all these advantages, optical imaging suffers from some draw backs such as limited penetration depth (1 cm), difficulty in performing whole-body scans, and low signal-to-noise ratio by virtue of autofluorescence. In addition, optical microscopy has; drawbacks including short focal lengths that narrows the application to samples smaller than a few millimetres and toxicity of most conventional dyes and agents that do pass the required pharmacokinetics for *in vivo* imaging [23].

1.3.1 Fundamentals of the Interactions of Light with Cells and Tissues

Biological samples and tissues contain a mixture of different biomolecules and cells with size ranging from submicron to over 20 μm. While the fundamentals for interaction of light with biological samples are similar to those with other bulk material, some critical differences are present that we will explain in this section. In general, as conceptually illustrated in Figure 1.2, an incident light beam undergoes four phenomena when travelling through material interfaces including reflection, refraction, scattering and absorption. As shown, Snell's law governs the refraction by

$$n \sin\theta = n' \sin\theta', \tag{1.1}$$

where n and n' denote refractive indices for the two mediums, describing the change in the speed of light travelling through the medium $c = c_0/n$, where c_0 is the speed of light in vacuum. The refractive index of individual tissue constituents varies from 1.33 for water to 1.55 for fat and concentrated protein solutions [43], resulting in an overall refractive index of around 1.4 typically used for biological tissues [44].

Reflection is mainly defined by three factors including refractive index of the medium of interest, polarization of light and the angle of incidence. In bioimaging applications, as the excitation sources are often collimated non-polarized lasers, the effect of polarization is limited. The effect of angle of

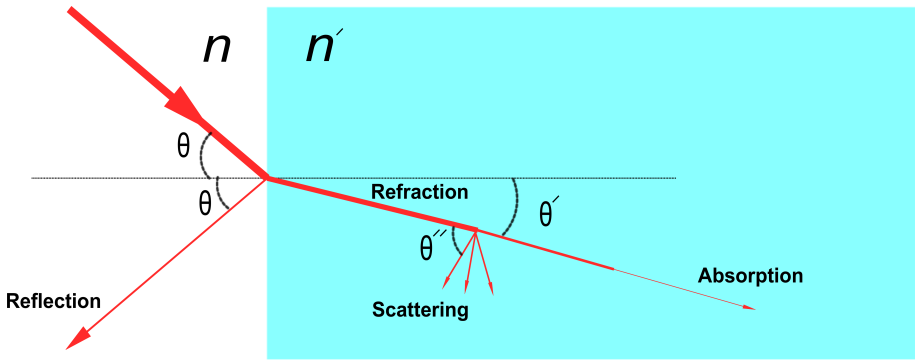

Figure 1.2: Propagation of light from one medium with refractive index n to another one with refractive index of n' ($n < n'$).

incidence on reflection is linear and the greater the angle of incidence the larger the reflection from the surface. Therefore, maximum light penetration achieved when the light beam is perpendicular to the tissue. In propagation from air ($n \approx 1$) to a tissue with a refractive index of n', the reflectance R, defined as the intensity of reflected to the incident light, is given by

$$R = \left(\frac{n' - 1}{n' + 1}\right)^2. \tag{1.2}$$

The absorption and scattering phenomena are discussed in more details in the following.

Absorption Absorption is the transfer of energy from the incident radiation to the propagation medium. If a collimated beam of light of intensity I_0 and wavelength of λ propagates through a non-scattering medium with width x, intensity of the emerging light is given by

$$I = I_0 e^{-\mu_a(\lambda)x}, \tag{1.3}$$

where $\mu_a(\lambda)$ is the absorption coefficient of the medium. The absorption coefficient is the number of absorption events happened per unit of length of the medium and its reciprocal is the distance in which the intensity falls to $1/e$ of the original intensity. It is also possible to say that for an absorbing material dissolved in a non-absorbing medium the absorption coefficient is proportional to the concentration c of the solution or

$$\mu_a = \alpha c, \tag{1.4}$$

where α is a constant known as specific absorption coefficient that defines the amount of absorption by a unit absorption concentration per unit length of beam penetration.

In a biological sample absorption occurs in a number of different individual chromophores with different absorption coefficients. In this case, the total absorption coefficient $B(\lambda)$ is expressed as the sum of the multiplication of concentration of each chromophore c_n with its specific absorption coefficient α_n or

$$B(\lambda) = \sum_n \alpha_n(\lambda) c_n. \tag{1.5}$$

Absorption in tissues can cause many photophysical and photochemical processes which could be classified to two major groups; radiative and nonradiative processes. An important example of radiative process is autofluorescence that will be described in Section 1.3.3 of this thesis. Examples of nonradiative processes include: (i) thermal effects such as protein denaturation and water vaporization, (ii) photochemical processes like photorearrangement and

photoaddition, and (iii) photoablation that means direct breaking of cellular structures usually caused by high energy UV radiation [7].

Scattering As illustrated in Figure 1.2, scattering is the optical phenomenon that changes the direction of radiation within a medium described by a scattering coefficient μ_s. In the case of collimated beam scattering coefficient is given by

$$I = I_0 e^{-\mu_s x}, \tag{1.6}$$

where I is the intensity of the non-scattered light after passing thorough a non-absorbing medium with the width of x. The main difference between absorption and scattering is that scattering leads to propagation of photons in different directions. Thus, if the medium is absorbing, the increased travelling distance of photons caused by scattering must be included through a differential path length factor DPF_x. In general DPF is a function of the scattering coefficient μ_s, the anisotropy of the scattering medium, the absorption of the medium and the geometry of the medium. Therefore, the attenuation of the scattered light can be described using the modified version of absorption equation as

$$I = I_0 e^{-\mu_a(\lambda) DPF_x + G}, \tag{1.7}$$

where G represents losses due to the geometry of the medium.

The anisotropy of the scattered beam is defined by anisotropy factor g which is the mean cosine of the scattering angle θ'' (shown in Figure 1.2). The anisotropy factor is given by

$$g = \int_{4\pi} d(\cos\theta'')\cos\theta'' d\theta'', \tag{1.8}$$

and depends on morphology, size and refractive index mismatches of the scattering centers. Depending on the medium, if $g = 0$ then scattering is isotropic, if $g = 1$ the scattering is completely forward and if $g = -1$ the light is back scattered. The isotropy factor in biological samples varies between 0.69 and 0.99 [45] and therefore it is mainly in a forward scattering mechanism. By considering the effect of isotropy on scattering, the reduced scattering coefficient μ_s' is given by

$$\mu_s' = \mu_s(1 - g), \tag{1.9}$$

where the reciprocal of μ_s' is the distance that a collimated light has a $1/e$ probability of an isotropic scattering event.

The most important kind of scattering in bioimaging is referred to as elastic scattering, which describes a scattering where the incident and scattered photons are of the same frequency. There are two different kind of elastic scattering including Rayleigh scattering and Mie scattering. Rayleigh scattering is caused by particles smaller than the wavelength of light and depends on wavelength of light with the factor of λ^{-4}, and therefore is significantly higher for blue than for near infrared. Mie scattering happen with particles of size comparable to the wavelength of light, it is less wavelength dependent (λ^{-x} with $0.4 \leq x \leq 0.5$) [7].

1.3.2 Optical Properties of Bulk Tissues

All the optical properties discussed in previous sections have been discussed with the assumption that a medium is, for example, only absorbing light, while in reality the optical property of a tissue is a mixture of different phenomena interacting with light. Therefore, the total intensity attenuation in a tissue sample is given by:

$$I_z = I_0 e^{-(\mu_a + \mu_s')z}, \tag{1.10}$$

where z is the measurement depth in the tissue. An important term arising from this equation is the optical penetration depth δ, defined as the distance that light can travel in a tissue by which the intensity of light drops to a fraction $1/e(\sim 0.37)$ of the original intensity of the beam. Equation (1.10) shows that the penetration depth δ is equal to $\frac{1}{\mu_a + \mu_s'}$. Therefore the optical penetration depth is mainly dependent on the type of tissue, concentration of cellular constituents, vascularity of the tissue, and wavelength of the incident light.

Measured optical properties of different tissue samples published in literature are summarized in Table [45, 46, 47, 48, 49, 50]. The measured values of absorption and scattering coefficient is an average value in a constant condition, while in reality tissues are alive and dynamic materials and therefore the optical properties are changing by conditions such as the amount of blood pumping into the tissue, the oxygenation of the blood and the presence of tissue chromophores and fluorophores. Note that the refractive index for all the tissues is assumed to be between water and lipid (n$\approx$ 1.4).

Water is one of the most abundant constituents of tissues, therefore significantly contributing to their optical properties. Although water absorbs light in infra red region ($> 1.3\mu$ m), but as illustrated in Figure 1.3, the absorption coefficient of water over the wavelength range of 660 to 920 changes from 0.0005 to 0.008 mm^{-1}, and it is 0.0022 mm^{-1} at 800 nm. Note that the water concentration of tissues usually remains unchanged, and therefore, water can be treated as a constant absorber [51].

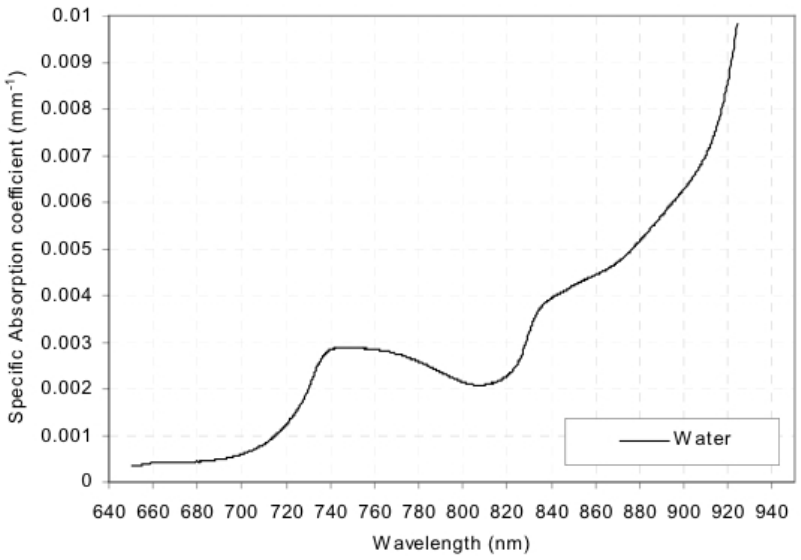

Figure 1.3: Absorption spectrum of water in red and near infrared region .

The most abundant chemical species in cells and tissues are proteins mainly built from amino acids. Amino acids have strong absorption in ultra violet (UV) region of the spectrum but proteins have absorption in other spectral region as well owing to their structural bondings . Proteins may also contain a chromophore, which provide a strong absorption, an important example being

hemoglobin. Hemoglobin is located in red blood cells (RBC) and is responsible for delivery of oxygen through our body. Deoxy-hemoglobin attaches to an oxygen molecule in our lung to become oxy-hemoglobin and therefore the ratio of this oxy-hemoglobin to total hemoglobin is a measure of blood oxygenation. Figure 1.4 depicts the absorption spectra of oxy- and deoxy-hemoglobin in red and near infrared (NIR) region. Although hemoglobin has absorption peaks around 280 nm, 420 nm, 540 nm and 580 nm the absorption coefficient of both oxy- and deoxy- hemoglobin decreases dramatically in red and NIR region [2]. The absorption spectra of melanin, skin pigment, covers almost all the visible region but decreases dramatically as wavelength increases.

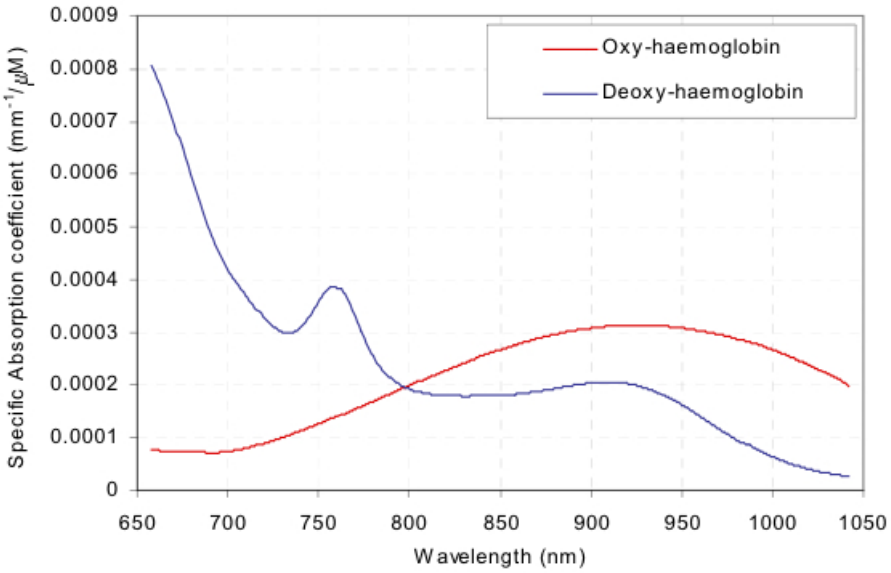

Figure 1.4: The absorption spectra of oxy- and deoxy-hemoglobin in red and NIR region [2].

1.3.3 Autofluorescence and Effect of Near Infrared Spectrum

One of the possible outcomes of light absorption in tissues is the occurrence of photochemical processes. Several cellular constituents fluoresce when excited by light or by transfer of chemical energy from other constituents in their proximity. Figure 1.5 illustrates the absorption and emission spectra of important endogenous fluorophores responsible for autofluorescence observed from typical tissue samples.

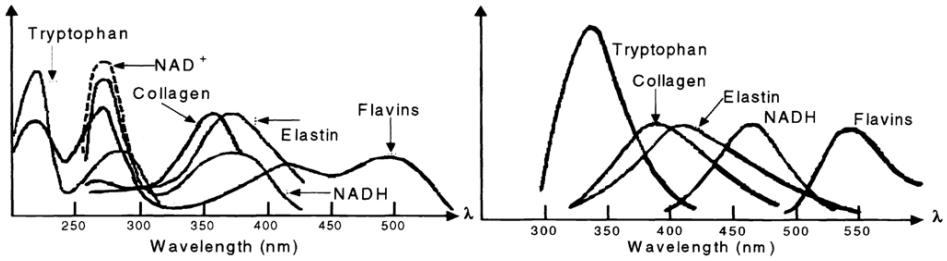

Figure 1.5: The absorption (a) and emission (b) spectra of important tissue fluorophores responsible for autofluorescence in aqueous solution. [3]

Although clinical fluorescence microscopes employ autofluorescence, this phenomena is detrimental to the signal to noise ratio (SNR), quality and resolution of optical molecular imaging. As depicted in Figure 1.5, the absorption spectra of important fluorophores are in the wavelength range of less than 500 nm and their emission spectra are located in blue to green region. The typical autofluorescence emission and absorption spectra signifies the underlying interest in low energy red or NIR spectra for optical imaging in view of minimum autofluorescence intensity, leading to increased SNR and image quality [52].

1.3.4 Near Infrared Optical Imaging

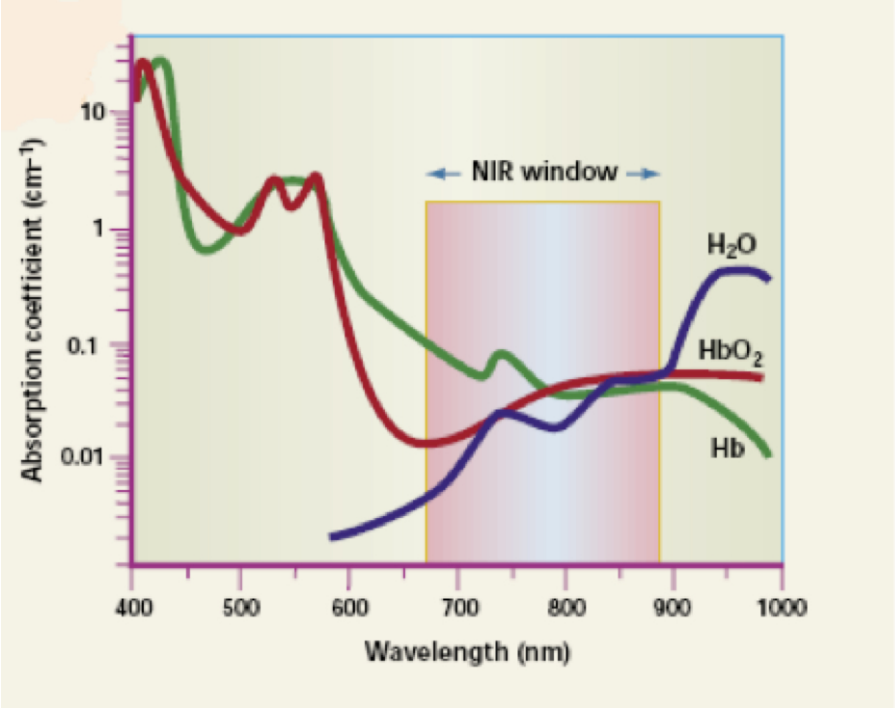

Figure 1.6: NIR biological window (650-900 nm) provides the maximum penetration depth in tissues for optical imaging [4] .

Despite all the advantages mentioned, the major drawbacks of optical molecular imaging are limited penetration depth due to absorption and scattering of excitation signal, tissue autofluorescence that suppresses SNR and image quality, and cellular phototoxicity and photodamage in exposure to ultraviolet (UV) or other high energy excitation sources. Light absorbance, scattering and autofluorescence is substantially dependent on excitation wavelength. The UV and visible (Vis) spectra are strongly absorbed by the most relevant tissue chro-

mophores (e.g., oxy- and deoxy-haemoglobin, myoglobins, lipids and melanin), reducing the penetration depth to only a few micrometers. In contrast, red and near infrared (NIR) spectra (650-1000 nm) have the minimum absorption and scattering in tissues, as shown in Figure 1.6, to be referred to as NIR biological window [4]. Theoretically, NIR radiation can go as deep as several centimeters depending on the type of tissue. For example, $\approx$ 10 cm in breast tissue and 4 cm for skull/brain and muscles [53]. The use of optical nanoparticles such as dye-doped nanoparticles, QDs and upconversion nanoparticles promise unparalleled improvements in NIR for optical imaging, which will be described in more detail in Section 1.5.

1.4 Magnetic Modality

One of the most important and clinically used modalities for molecular imaging is magnetic modality including magnetic resonance imaging (MRI) and magnetic resonance spectroscopy (MRS). Basically, MRI systems construct an image from relaxation response of living subjects to a strong static magnetic field. This modality provides high spatial resolution ($<$ 1 mm), high tissue penetration depth, no exposure to ionizing radiation, possibility of whole body imaging and excellent soft-tissue contrast [20, 21, 22]. Disadvantages of this modality include low sensitivity, slow data acquisition and infrastructure costs. The practical usage and performance of magnetic modalities can be enhanced by using conventional and novel contrasts and magnetic nanoparticles. In the following, we present fundamentals of magnetism and MRI, followed by the magnetic prop-

erties of bulk tissues and the methods that we used in this work for magnetic characterization of nanoparticles.

1.4.1 Fundamentals of Magnetic Materials

Magnetic properties of materials arises from superposition of the magnetic moment $\vec{\mu}_m$ of all electrons in the material. This moment comprises of both the orbital magnetic moment $\vec{\mu}_{orb}$ that is proportional to angular momentum of the electron $\vec{L}$ and the spin magnetic moment $\vec{\mu}_{spin}$. The magnetic moment for complete atomic shells reduces to zero as orbital and spin moments of opposite signs cancel each other [54]. However, for some magnetic materials the unpaired spins and orbital moments lead to a macroscale magnetic moment that can be measured. The atomic magnetic moments of a magnetic material can align in the direction of an external magnetic field, generating a magnetization vector and additional magnetic field according to

$$B = \mu_0(H + M), \tag{1.11}$$

where μ_0 is the magnetic permeability of free space, H the strength of the external magnetic field and the magnetization vector M is the average total magnetic moment per unit volume. The relative magnetic permeability of the material μ_r is then defined as

$$\mu_r = \frac{B}{\mu_0 H}, \tag{1.12}$$

and the magnetic susceptibility as

$$\chi = \frac{M}{H}. \tag{1.13}$$

Depending on magnetic susceptibility χ and response to an external magnetic field, materials are classified as diamagnetic, paramagnetic, ferromagnetic and superparamagnetic materials, as schemactically illustrated in Figure 1.7 [5, 55, 56]. Diamagnetic materials (e.g., Si, Ge, Cu, Au, Ag, water, organic materials and polymers) have a small, negative and temperature-independent susceptibility (-10^{-6}), due to the non-cooperative behaviour of orbiting electrons exposed to an external magnetic field. Paramagnetic materials (e.g., O_2, Li, Mg and Mo) show a partial alignment of the magnetic moments of unpaired electrons in the direction of the external field, resulting in a small positive magnetization and susceptibility (10^{-5}). The efficiency of the external field in aligning the magnetic moments reduces by the randomizing effects of increasing temperature, leading to a susceptibility that is inversely proportional to temperature according to Curie's law $\chi \propto 1/T$. Ferromagnetic materials (e.g., Fe, Co and Ni) have large susceptibility and maintain a large magnetization in the absence of the external field. The atomic moments exhibit strong interactions due to electronic exchange forces, resulting in parallel or antiparallel alignment of the moments in uniformly magnetized domains. The relationship between M and H is highly non-linear and magnetization saturates to M_{sat} at high field. The magnetization vanishes for temperatures above a Curie temperature (T_c).

1.4.2 Fundamentals of Magnetic Resonance Imaging

Magnetic resonance imaging (MRI) is a powerful noninvasive diagnostic tool for visualizing soft tissues. A biological tissue is placed in a large magnetic field B_0

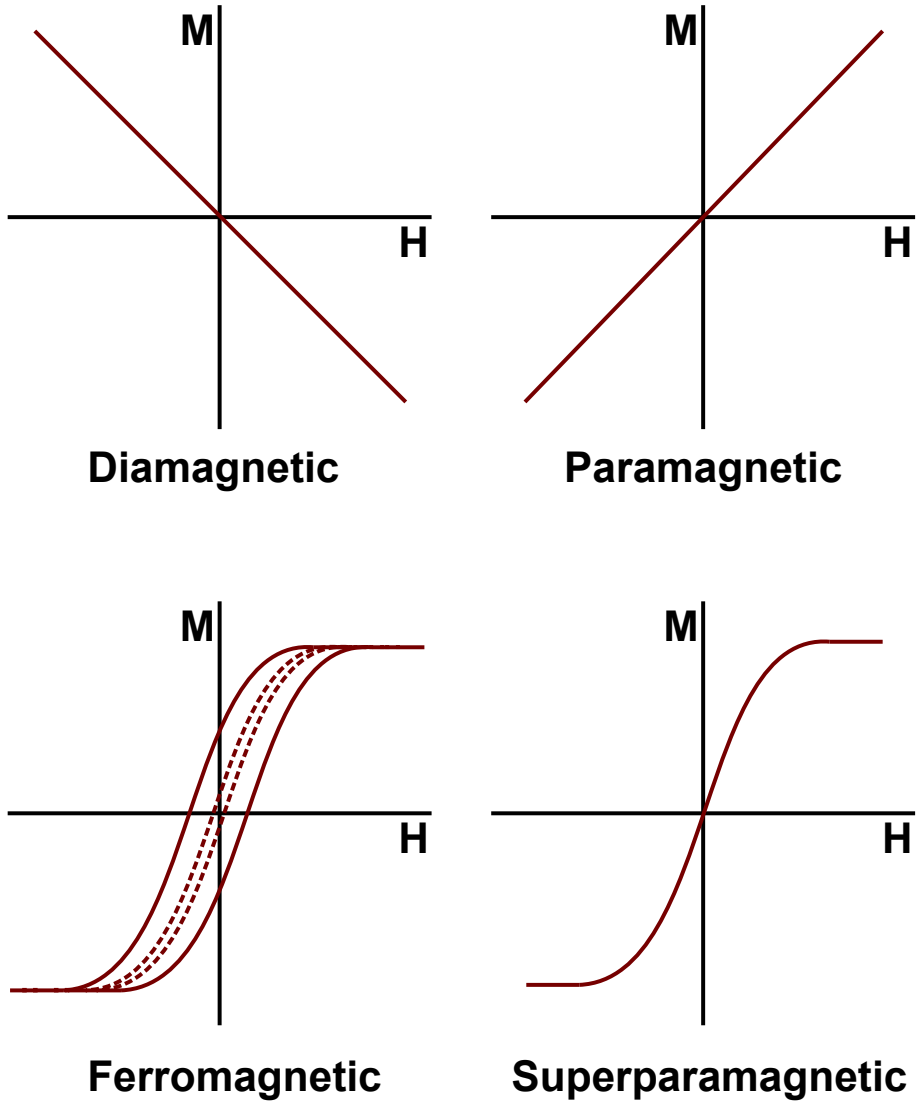

Figure 1.7: Magnetic responses (M-H curves) associated with different classes of magnetic materials: diamagnetic, paramagnetic, ferromagnetic and superparamagnetic materials. Dashed lines illustrates the hysteresis of ferromagnetic materials [5].

to align the spin of protons of molecules in biological tissues or body [57, 24]. As shown in Figure 1.8, a pulsed radio frequency (RF) electromagnetic wave in a plane perpendicular to B_0 is used to flip the proton magnetization, which relaxes back to its original direction with a Larmor precession frequency (ω_0) given by

$$\omega_0 = \gamma B_0. \tag{1.14}$$

Here, γ is the gyromagnetic ratio of protons and is equal to 2.67×10^8 rad $\mathrm{s}^{-1}\mathrm{T}^{-1}$, yielding a Larmor precession frequency of $\frac{\omega_0}{2\pi} = 42.57$ MHz at $B_0 = 1$ T. A RF signal is emitted during relaxation that is detected by the MRI scanner to construct an image [5, 6].

As illustrated in Figure 1.8 for the static magnetic field in z direction, the magnitude of M_z and M_{xy} are given by

$$M_z = M(1 - e^{\frac{-t}{\tau_1}}) \tag{1.15}$$

and

$$M_{xy} = m\sin(\omega_0 t)e^{\frac{-t}{\tau_2}}, \tag{1.16}$$

respectively, where τ_1 is the longitudinal (spin-lattice) relaxation time and τ_2 the transverse (spin-spin) relaxation time. The time constant τ_1 is related to the energy loss from the magnetic moment to its surrounding lattice and is related to the coupling of the proton moments to the surrounding materials. The transverse relaxation time τ_2 is relatively fast and is driven by the loss of phase coherence in the precessing protons due to their magnetic interactions

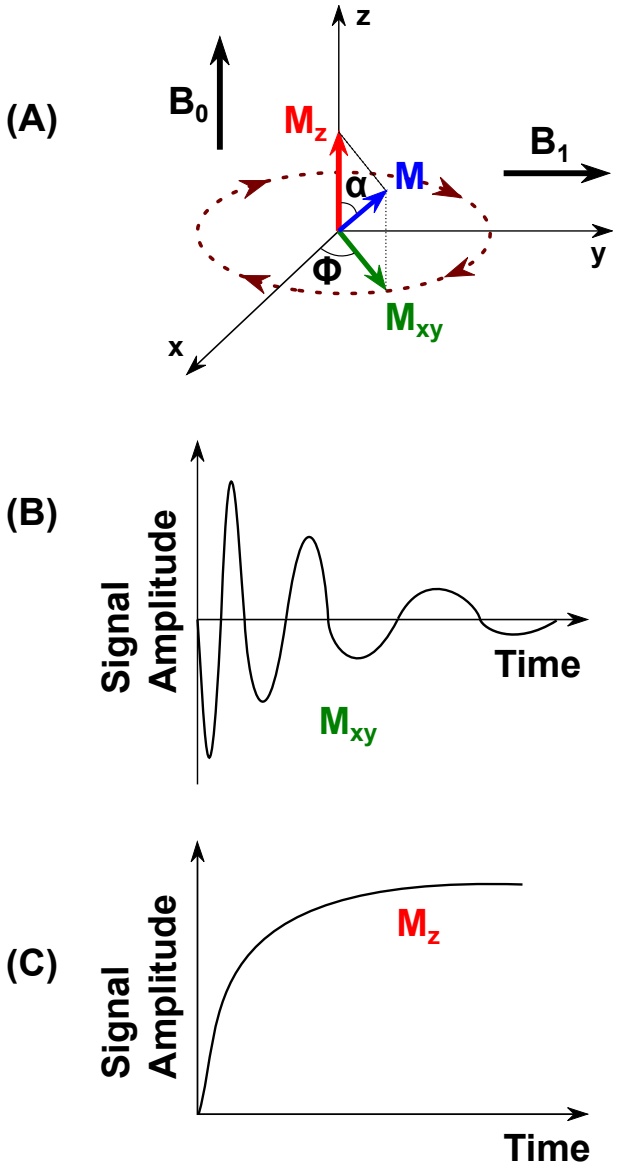

Figure 1.8: (A) Magnetization vectors of a sample with original moment M in the presence of a static external magnetic field B_0 and resonant magnetic field pulse B_1, perpendicular to B_0. (B) When the oscillating field B_1 is removed at time 0, the in-plane magnetization M_{xy} rotates around z with a decreasing amplitude while (C) M_z gradually reaches its maximum (redrawn using [5, 6])

with each other and other fluctuating moments in the tissue. Dephasing can also be affected by local inhomogeneities and causing the replacement of τ_2 with a shorter relaxation time τ_2^*, given by

$$\frac{1}{\tau_2^*} = \frac{1}{\tau_2} + \gamma \frac{\Delta B_0}{2}, \tag{1.17}$$

where ΔB_0 is the variation in the field caused by distortions in the homogeneity of the applied field or by local variations in the magnetic susceptibility of the system [58].

Magnetic contrast agents are used to shorten the relaxation times of the selected tissue, increasing the contrast of the surrounding tissues. These contrast agents are classified as T_1 and T_2 agents employed for enhancing the contrast for longitudinal and transverse relaxation processes, respectively. The strength of the contrast agents is usually measured as the relaxivity $R_i = 1/\tau_i$ at 20 °C and $i = 1$ and 2 for longitudinal and transverse processes, respectively. The T_2 agents are mainly iron oxide nanoparticles which exhibit superparamagnetic with magnetic susceptibility many times higher than paramagnetic nanoparticles. Paramagnetic T_2 agents are also available but less effective. Because the T_2 agents decrease the magnitude of the signal in order to produce contrast they are famous as negative contrast agents that require a small r_2 for being effective. The negative nature of T_2 agents causes confusion between pathologic dark areas like bleeding or metal deposits with normal dark areas like air in the lung. Another drawback of T_2 agents is their high susceptibility causing distortion in the image from the surrounding tissues, what is referred to as the booming effect [59].

T_1 contrast agents are usually paramagnetic metal ions based on gadolinium (Gd), dysprosium or manganese [60]. The magnetization strength of the agents is dependent on the number of metal ions. An advantage of T_1 agents over T_2 agents is that they produce bright signal in MRI images and therefore are better to distinguish small changes in contrast. Magnetic nanoparticles will be discussed in more detail in Section 1.5.3.

1.4.3 Magnetic Properties of Bulk Tissues

As mentioned in the previous section, there are two type of relaxation mechanisms T_1 and T_2 enabling a MRI system to produce signal. T_2 relaxation depends on how fast protons in a specific tissue lose their phase coherence, and consequently, this relaxation mechanism is highly dependent on the density of protons. A higher proton density means a faster relaxation. T_1 relaxation depends on the efficiency of energy transfer to the tissue, and this efficiency is related to the vibrational frequencies and the physical composition of a specific tissues [24]. Different tissues in the body have different compositions, and as a result, different magnetic behaviour.

Due to the dependence on the density of protons for T_2 relaxation, fluids with low density of protons provide less dephasing and a long T_2 relaxation, whereas solid tissues have the highest density of protons and therefore produce a short T_2 signal. In the case of fat and protein rich tissues, the dephasing is at a medium level, thus providing an intermediate T_2 signal. The T_1 relaxation is

related to the efficiency of energy transfer and vibrational states of the protons. Fluids vibrates at higher frequency therefore the energy transfer is inefficient, resulting in a very long T_1 relaxation. For fat and protein rich tissues, the rotational frequency around the C–C bonds is near the Lamor frequency, and consequently, energy transfer is efficient, producing a short T_1 relaxation signal. The approximate lifetime values of T_1 and T_2 relaxation mechanisms for some human tissues are summarized in Table 1.2 [24].

Table 1.2: The approximate lifetime values of T_1 and T_2 relaxations for some human tissues, under an external magnetic field of 1.5 T [24].

Tissue type	τ_2 (ms)	τ_1 (ms)
Adipose tissues	60–80	240–250
Whole blood (oxygenated)	200	1350
Cerebrospinal fluid	500–1400	2200–2400
Grey matter	100	920
White matter	90	780
Liver	40	490
Kidney	60–75	650
Muscle	50	860–900

1.5 Nanoparticles for Molecular Imaging

1.5.1 Role of Nanoparticles in Bioimaging

As mentioned before, the requirements of an efficient and practical molecular imaging system can be summarized as suitable modality for the imaging application, availability of agents for targeted detection and finally availability of targets that can facilitate better, faster and non-invasive detection of an illness or a physio-pathological processes. Conventionally, some dyes and contrasts agents have been used to enhance the clarity of different imaging modalities. This includes barium for X-ray imaging or ^{99m}Tc for nuclear imaging. Nanoparticles can bring revolutionary effects as materials in nanoscale behave differently than the bulk. The first specific feature of nanoparticles is their high surface to volume ratio, resulting in greater functionality sites on the surface for the same amount of material. Second, different functional substitution for enhancing contrast and/or targeting specific molecules can be added to a single nanoparticle for multi-target, multi-purpose and multimodal imaging. Finally, in the area of bioimaging small nanoparticles are less hindered by biological barriers [20, 21, 22]. Nanoparticles also suffer from some important drawbacks such as interaction with plasma proteins, being digested by phagocytic agents or reticuloendothelial systems, and acute or chronic toxicity.

The design criteria for practical nanoparticles that can be used in molecular imaging are manyfold:

First, multifunctional particles in the range of 30 to 150 nm are preferred [22], since smaller particles are filtered rapidly through kidney and larger parti-

cles will be trapped in reticuloendothelial system (RE) including lymph nodes, liver and spleen. Particles in this range can remain in body circulation for long enough time in order to get accumulated in the place of interest for improved signal to noise ratio. Larger size particles not only decrease the possibility for targeted imaging by getting trapped in the RE system, but also intervene in kinetics of these organs and cause serious toxicology issues. Note that surface modification chemicals such as polyethylene glycol (PEG) or silica can prevent or decrease the possibility of trapping in RE, and therefore, particles smaller than 30 nm can be potentially used with surfactants, but unfortunately this method has little effect on liver accumulation and toxicity of particles [61].

The second criterion in designing a nanoparticle for molecular imaging is the concentration of agents required for generation of a measurable signal. This feature is completely dependent on the modality and sensitivity of imaging method used. For example, usually one or two radionuclide molecules per particle are enough for a measurable contrast in PET. Also each quantum dot (QD) contains one exciton, while for fluorochromes doped particles; a single particle may need up to 100 dye molecules [22].

Third criterion is the number of targeting groups that can be attached to a single particle. This feature is important for targeting efficiency of the particle and is related to the type of target and ligands as well. One of the most important ligands and targets with clinical application in molecular imaging is antibody-antigen complexes. To increase the detection efficacy of a nanoparticle, it must be attached to many antibodies that can bond to antigens. For an

efficient targeting, a 50 nm nanoparticle is tagged by at least 10 antibodies [22].

Mechanical properties of nanoparticles are the fourth important criterion. Nanoparticles used in molecular imaging will be exposed to different biological conditions, and as such they should be structurally and chemically stable and not get affected by the environment. While this stability is required for the particle to tolerate flow turbulence in blood streams, a highly stable particle cannot be removed from the body unless by phagocytes, which means exceeding toxicity level. Therefore, the ideal nanoparticle for *in vivo* imaging is the one that is stable enough to remain in blood stream to reach the target and provide signal for detection, and then disintegrates and excretes through kidney [22].

Another important factor is the biocompatibility of the surface of a nanoparticle. Almost all nanoparticles need to have surface modification after synthesis because body considers them as foreign entities and tries to get rid of them. The larger the particle the more likely it will be trapped in the body so they should be covered by some inert material such as silica or polyethyleneglycol (PEG) to be "stealth" in the body [62, 63] . Surface modification also helps to reduce nanoparticles toxicity and improve their stability.

Several nanoparticles with different matrix materials have been used for different molecular imaging modalities as summarized in the following. Schematic of some of the available nanoparticles are presented in Figure 1.1:

1. Liposomes are self-organized nanoparticles that consist of amphiphilic

compounds which can encapsulate dyes and medical materials [64]. A successful example of clinical applications of nanoparticles for drug delivery is the liposomal daeunorubicin that has been approved by FDA for treatment of Kaposi sarcoma [65].

2. Metal oxide nanoparticles are used in molecular imaging as imaging agents for MRI, but optical metal oxide particles are now being researched for optical modality. superparamagnetic iron oxide (SPIO) [66] and Y_2O_3 upconversion nanoparticles [67] are examples of MRI and optical modality agents, respectively. Since metal oxides do not have surface functionalities, they have to be coated with functional molecules to be of use in drug delivery applications.

3. Dendrimers are made from small building blocks for engineering nanoparticles with a high control over their size, composition, shape, weight, branching length and density using lego and click chemistry. Their controlled size and composition lead to designable biocompatibility and pharmacokinetics [68].

4. Polymer particles have been used for conjugation of drugs and imaging dyes, for example poly-L-glutamic acid-paclitaxel conjugates (Xyotax^{TM}) or cyclodextrin-camptothecin conjugate (IT-101) [69].

5. Proteins can be used as the matrix material of nanoparticles. Famous examples of this kind of nanoparticles are albumin and gelatine nanoparticles or other types of proteins which are generally referred to as "protein cages", which have been used for drug delivery [70].

6. Metal nanoparticles such as gold [71] and silver nanoparticles [72] have

applications in optical imaging, while bismuth nanoparticles [73] have been used in CT molecular imaging.

7. Viruses can be used as a scaffold for imaging agents and drug delivery [74].

8. Carbon-based nanoparticles such as carbon nanotubes (CNT) have been investigated for imaging and drug conjugation, but there are some important toxicity issues for CNTs [75].

Other optical and magnetic particles will be described in the next two sections in more details.

It is important to note that the process of getting approval for using a nanoparticle in clinical application is laborious, costly and difficult like any other pharmaceutical product. The process consists of several steps including: (i) Identify and validate a molecular target to be targeted by the nanoparticle by using microarrays, immunostaining, blotting, genomics and proteomics. (ii) Binding compound should be identified and tested while attached to the particle by using *in vitro* experiments. (iii) Third step is the preclinical and optimization step where specificity, stability, off-target effects, bio-distribution and pharmacokinetics of targeted nanoparticles is tested by *in vivo* animal tests. (iv) Clinical development step, in which toxicity tests, clinical examination phase I, II and III is performed to approve the elements checked in step 3 this time in human. (v) FDA approval and after that finally nanoparticle can be used in clinical applications [20].

1.5.2 Optical Nanoparticles

There are two different types of optical imaging agents used in optical molecular imaging, namely, endogenous and exogenous contrasts. Endogenous agents work on the basis of an enzyme-mediated process in cells and tissues to emit the optical signal for detection. There are two important examples for endogenous probes: luciferin/luciferase bioluminescence systems [76] and fluorescent proteins such as green fluorescent protein (GFP) [77]. Important drawbacks of fluorescent proteins are the need for genetical modification of targeted cells and low emission wavelength (510 nm) overlapping the autoflourescent signal of surrounding tissues. Luciferin/luciferase systems also suffer from positional uncertainty due to inhomogeneous scattering, limited light penetration, dependence on environmental parameters such as pH and temperature and the apparent need for a stable expression of luciferase [23]. Other types of optical imaging agents are exogenous contrasts such as organic fluorophores, quantum dots (QDs) and upconversion particles, which are inserted in to the bio-system from outside.

Conventional organic fluorescent dyes are one of the most important optical agents with applications in clinical, paraclinical and research. Some examples of organic fluorophores are fluorescein iso thiocyanate (FITC), carboxyfluorescein diactatesuccinidyl ester (CFSE) and IRG-023 Cy5 [78]. These kind of optical imaging dyes suffer from disadvantages such as rapid photo-bleaching, chemical instability and biodegradation in biological environment due to their typical sensitivity to pH and interacting local ions. As such, these agents are not suitable for long term cell tracking and time-resolved detection (TRD) methods.

These agents are usually not soluble in aqueous solutions, leading to poor interactions with biomaterials and their toxicity. Conventional dyes are mainly excited by UV-Vis light spectrum that has limited penetration depth, have low signal to noise ratio due to auto-fluorescence, and cause photodamage to the cells. Organic dyes are not suitable for simultaneous multicolour imaging, as their emission are mostly overlapped with each other or overlapped with autoflourescent produced by nicotinamide, flavins, collagen and elastin as shown in Figure 1.5 (Page 18). Although the problem of autofluorescence can be curtailed by using NIR emitting dyes such as cyanine particles, but these dyes suffer from low quantum yield (low brightness) and poor photostability [23, 78, 79, 80]. As a result, conventional dyes are far from an ideal candidate for optical imaging, with attributes such as high signal to noise ratio, good photochemical stability, absence of interfering compounds, low toxicity, rapid signal generation, high quantum yield, high absorbance, low cost synthesis, excitation and emission in NIR region and adequate dispersibility in a biological environment. Table 1.3 summarizes the effort for curtailing the disadvantages of conventional optical nanoparticles including organic dye-doped nanoparticles, QDs and upconversion nanoparticles [81, 25].

Organic-doped nanoparticles are one of the novel solutions to overcome problems of conventional dyes. These kind of nanoparticles usually made from silica and sometimes from other polymers such as poly (D, L-lactic-co-glycolic acid) (PLGA) [82]. The size of these particles is in the range of 2 to 200 nm. They have advantages such as increased *in vitro* and *in vivo* stability, acceptable chemical stability, low possibility of photobleaching as dyes are protected by

Table 1.3: Comparison of novel optical nanoparticles and conventional organic dyes [25].

Parameters	Conventional organic dyes	Organic dye-doped nanoparticles	QDs	Upconversion nanoparticles
Size	-	50-500 nm	2-10 nm	50-200 nm
Autofluorescence	High	High	High	Low
Light penetration depth	Low	Medium/high	Medium/high	High
Photodamage	Medium	Medium/low	Medium/low	Low
Photostability	Low	Low/medium	High	High
Excitation wavelength	UV/Vis/NIR	UV/Vis/NIR	UV/Vis/NIR	NIR
Cytotoxicity	Medium	Medium	High	Low
Synthesis cost	Medium	Low/medium	High	Low
Multicolour assays	NA	NA	Good	Good

a silica layer, increased hydrophilic properties, bright emission as each particle include large number of dyes and diversity of silica chemistry for synthesis and bioconjugation. The disadvantage of this kind of particles is that encapsulation can alter fluorescent emission of the dyes [23, 25].

As another novel optical nanoparticle, quantum dots (QDs) are important candidates for *in vitro* optical molecular imaging. QDs are semiconductor crystals with dimensions in the range of 1 to 10 nm and luminescence properties due to quantum confinement effects. The emission is size dependent and typically in a narrow band with 30 to 40 nm full width half maximum (FWHM), whereas the absorption spectrum is broad from UV to NIR [25, 83]. Two main categories of QDs are II-VI particles such as CdS, CdSe and CdTe and III-V QDs such as GaAs, InP and InAs [23]. III-V QDs are toxic but generally less toxic and more biocompatible than II-VI QDs, but III-V particles are difficult to synthesise and also suffer from much lower quantum efficiency than II-VI counterparts. In comparison to conventional organic dyes, the emission band of QDs can be tuned over a wide range by changing the size and composition of the particles. Examples include UV-blue emission from ZnS QDs, visible emission from CdE (E=S, Se or Te) and NIR emission from CdS/HgS/CdS, InP and InAs QDs. In addition, QDs have a broad excitation and narrow emission spectra. This is particularly attractive for multicolour imaging using a single excitation source, where overlapping of emission wavelength is not desired. QDs are resistant to photobleaching, but prone to blinking when used without surface modification. Consequently, to improve photostability and reduce toxicity of QDs, they are often covered with a surface shell, made from ZnS,

ZnSe or GaAs. The shell can also improve water-dispersibility and resistance to metabolic degradation. Examples of materials used for the surface include mercaptoacetic acid, phosopholipid micelles, silica and amine modified poly(acrylic acid). These surface modifications significantly suppress toxicity, as proven by experiments where the cells loaded with these QDs remain alive for more than 12 days [84]. An important advantage of QDs is their large extinction coefficient ($0.5 - 5 \times 10^{-6}$ $M^{-1}cm^{-1}$) which means that they are very bright probes [85]. QDs also have long fluorescent lifetime on the order of 20 to 50 ns, which allows them to be distinguished from background noise for increasing imaging quality. Finally, QDs have a high quantum yield (up to 85%) which is not affected by protein conjugation [23].

Although QDs provide many advantages and novel NIR-emitting QDs open a new platform for *in vivo* molecular imaging [86, 87], they suffer from some important issues including toxicity and dependence on high energy excitation sources that decreases the signal to noise ratio (SNR) due to tissue autofluorescence. Considering these problems upconversion nanoparticles have attracted attention as the next generation of optical molecular imaging probes.

1.5.3 Magnetic Nanoparticles

Iron oxide nanoparticles are the first and most commonly used magnetic nanoparticles used as MRI contrast. Some of the main advantages of iron oxide particles for bio-applications include chemical stability, lack of toxicity and biodegradability. It is also important to mention that iron oxide nanoparticles have been

through regulatory processes and could be used legally and safely in human. Basically, iron oxide particles are superparamagnetic and classified as a T_2-relaxivity-based dark or negative contrast agents. To increase the applicability of iron oxide particles they usually need to be covered and functionalized to make them more biodegradable and help these particles to reach their targets easier. Covering iron oxide particles with dextran or with carbodextran is the most common way for surface modification of these particles [26]. Another useful method is the encapsulation of iron nanoparticles in other nanoparticle structures such as liposomes and dendrimeres [88, 89]. Superparamagnetic iron oxide (SPIO) particles for biomedical applications exist in many forms defined mostly by their hydrodynamic diameter, for example, Oral-SPIO (300 nm – 3.5 μm), Standard-SPIO (SSPIO, 60 – 150 nm), Ultrasmall-SPIO (USPIO, 5 – 40 nm), a subset of USPIO called monocrystalline iron oxide nanoparticles (MION) and MIONs with a chemically crosslinked polysachharide shell are termed cross linked iron oxide (CLIO) [27, 28].

Another important type of magnetic nanoparticles is cobalt nanoparticle. Cobalt nanoparticles have much higher room temperature saturation magnetization (1422 emu cm^{-3}) as compared to iron oxide (395 emu cm^{-3}), and therefore, cobalt nanoparticles have larger effect on proton relaxation so even ultra-small particles can be used as MRI contrast agents without sacrificing sensitivity [29]. Like iron oxide particles, cobalt nanoparticles are also classified as a negative contrast as they mainly affect T_2 relaxation. Although cobalt is routinely prescribed for treatment of some illnesses such as refractory anemia, and there is connection with receiving high amount of cobalt and cardiomyopa-

thy [90], but still there is no accurate data available on the toxicity of cobalt nanoparticles and application of these kind of nanoparticles for MRI imaging is dependent on the toxicology results of these particles [91].

The applicability of iron oxide nanoparticles as MRI contrasts is limited by their physicochemical properties as the magnetisation of these particles depends on their size and their surface chemistry. For example, it has been proven that larger iron-oxide particles exhibit larger T_2 effect [92]. To overcome this problem different spinel ferrite nanoparticles are introduced with high and tunable magnetisation. The spinel ferrites nanoparticles are MFe_2O_4, where M is a +2 cation of Mn, Fe, Co or Ni. The $MnFe_2O_4$ has the highest magnetic susceptibility and the strongest R_2 relaxivity value of 358 $mM^{-1}s^{-1}$ [93]. Another reported mixture is spinel $Zn_{0.34}Fe_{0.66}Fe_2O_3$ with a R_2 relaxivity value of 294 $mM^{-1}s^{-1}$. Another way to overcome the above-mentioned problem is the idea of making core-shell magnetic nanoparticles such as Fe_3O_4:$mSiO_2$ a superparamagnetic particle with a 15 nm core size and 3.4 $mM^{-1}s^{-1}$ and 245 $mM^{-1}s^{-1}$ for R_1 and R_2 relaxivity values, respectively [94].

The other important group of magnetic nanoparticles is the T_1 contrast agents which are usually paramagnetic metal nanoparticles based of Gd, dysprosium or manganese [24, 60]. The magnetisation of these nanoparticles are directly related to the number of metal ions in their structure. In order to reduce possible toxicity effect of heavy metals such as Gd, conventional T_1 contrasts are built by attaching Gd ions to a chelate molecule. This problem is greatly reduced by using novel surface modified nanoparticles. For example,

novel Gd based nanoparticles is the Gd:$C_{82}(OH)_{22\pm2}$ paramagnetic nanoparticles that show T_1 relaxivity 10 times more than commercially avaialble contrast Gd-DTPA [30]. A list of commercial and novel contrast agents with some of their magnetic properties is presented in Table 1.4.

Table 1.4: Commercial and novel MRI contrast agents and some of their magnetic properties. [5, 26, 27, 28, 29, 30]

Name	Coating materials	Average size (nm)	R_2 ($mM^{-1}s^{-1}$)	R_1 ($mM^{-1}s^{-1}$)	R_2/R_1
Feridex	Dextran	80 – 150 nm	100	10	10
Resovist	Carbodextran	62	151	–	–
Combidex	Dextran	20 – 40	53	–	–
CLIO or MION	Dextran	10 – 30	69	–	–
Magnevist	–	–	4.6	4.6	1
Fe_3O_4	DMSA, PEG	15	218	4.6	47.4
$MnFe_2O_4$	DMSA	15	358	1.1	325.5
Gd_2O_3	D-glucuronic acid	100	10.9	9.9	1.1
Gd:$C_{82}(OH)_{22\pm2}$	–	100	–	14.1	–

1.5.4 Toxicology Issue of Nanoparticles Used in Molecular Imaging

One of the most important issues in clinical applications of nanoparticles used in molecular imaging is their unknown acute and chronic toxicity. Generally, nanoparticles can interact with cells in different ways to produce toxic effects.

Firstly, nanoparticles can produce toxic materials, ions or can generate reactive oxygen species (ROS) when contacting cells. Secondly, the probability for decomposition of materials is higher at nanoscale than in bulk. Thirdly, nanoparticles can remain in a cell membrane or go into a cell and impair its functions. Finally, morphology of nanoparticles can have toxic effects, for example, such effect has been observed for carbon nanotubes (CNT) [95]. Another example is CdTe QDs that can have different levels of toxicity dependent on their size. While spherical particles exhibit limited or no toxicity, rod shape nanoparticles increase cell proliferation and platelet particles are cytotoxic [96].

Important features of nanoparticles that are critical to toxicity effects are the chemical core and surface composition of nanoparticles. For example, bare polystyrene nanoparticles are less toxic than when they are covered with carboxylic acid (-COOH) groups [96]. The crystal phase and structure are also important for toxicity. For example, anatase phase TiO_2 is hundred times more toxic than rutile phase TiO_2 particles. One important advantage of upconversion nanoparticles over other types of optical nanoparticles is that lanthanides used in these particles are considered relatively safe and non-toxic [97]. Some other issues about nanoparticles toxicity and catabolism will be discussed in Section 5.4.

1.6 Upconversion

In Section 1.5.2, we discussed different types of nanoparticles for optical molecular imaging. Almost all of these nanoparticles and dyes have excitation and emission through normal fluorescence in which a high energy (shorter wavelength, commonly UV-Vis) excitation used to excite the probes followed by relaxation to ground level and lower energy emission (longer wavelength). Typical fluorescent imaging has been used for a long time in florescent microscopes. Introduction of nanoparticles such as QDs improves the resistivity of the probes to photo-bleaching and increases the sensitivity and specificity of the imaging by providing a narrow and distinguishable emission signal. But as discussed earlier, there are two major problems with normal fluorescent imaging: first, the high energy excitation source leads to an intense autofluorescence from cells and tissues, which overlaps the signal emitted from nanoparticles or dyes, leading to a low signal to noise ratio (SNR). Second, UV-Vis excitation has limited penetration depth, and therefore, limited application for *in vivo* imaging to surface areas like skin and surface organs.

To overcome these major issues of fluorescent imaging, novel methods use other optical phenomenon such as two-photon absorption and upconversion. Figure 1.9 illustrates the schematic of three different optical phenomena, namely fluorescence (down conversion), two-photon absorption and upconversion. In a down conversion process, a high energy photon excites the material from the ground level (G) to E2 energy level, followed by a nonradiative relaxation to E1 state and an emission with a lower energy. In a two-photon absorption, the low-energy photons simultaneously excite a sample at a focal point by the

sum of the energy of both photons (i.e., from G to E2), and therefore, a high energy photon is emitted. Finally, in an upconversion process, two or more low energy photons are absorbed by the sample in order to excite the sample to E2 level, by a ladder like energy absorption process, and finally when the electron reaches the emitting energy level, a higher energy emission signal is produced [9]. The possibility of using low energy excitation sources in upconversion and two-photon absorption enables us to avoid autofluorescence in bio imaging with significant potential for *in vivo* imaging. The advantage of upconversion over two-photon microscopy is that for two-photon absorption expensive femtosecond lasers must be used to achieve a small focal point but with upconversion it is possible to use economical continuous wave laser diodes.

1.6.1 Upconversion Phenomena and Mechanisms

Upconversion is a nonlinear optical phenomenon characterised by conversion of low energy (long wavelength) radiation, for example near infrared (NIR), to a high energy (short wavelength) radiation, for instance visible. Although the concept of upconversion was first introduced in the mid 1960s [8], it has attracted a high level of interest in the recent years because of their versatile applications in different fields such as photochemistry, photonics, biophysics, solid state physics, material science and optical molecular imaging. The key point in this optical phenomenon is the sequential absorption of photons into ladder like energy states and therefore lanthanide materials play a crucial role in the upconversion phenomenon.

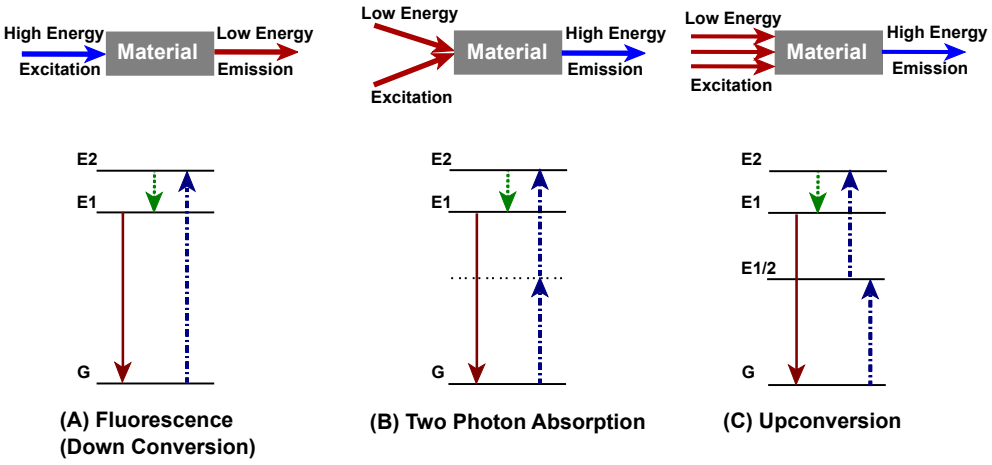

Figure 1.9: Schematics of different optical phenomena and corresponding energy levels: (A) Normal fluorescence (down-conversion), (B) Two photon absorption and (C) Upconversion. The dashed/dotted (blue), dashed (green) and full arrows (red) represent photon excitation, non-radiative relaxation and emission processes, respectively (redrawn using [7, 8]).

Figure 1.10 depicts mechanisms of upconversion phenomenon, where an anti-stoke lower wavelength emission is resulted from a material excited with a higher wavelength excitation source, through four different mechanisms: excited state absorption (ESA), energy transfer upconversion (ETU), photon avalanche (PA) and energy migration-mediated upconversion (EMU) [9, 98, 10]. The energy of the emitted photon in all these mechanism is based on a sequential absorption of at least two photons by one or more metastable excited energy states between the ground and the emitting states of the ion. In this sense, the upconversion is different from the other anti-stokes luminescence phenomenon such as multi-photon absorption and the second harmonic generation, in which simultaneous absorptions of the photons is required [9, 8]. In contrast to virtual states in

two-photon absorption and second harmonic phenomena, upconversion emission happens through physically existing states that are more efficient [19].

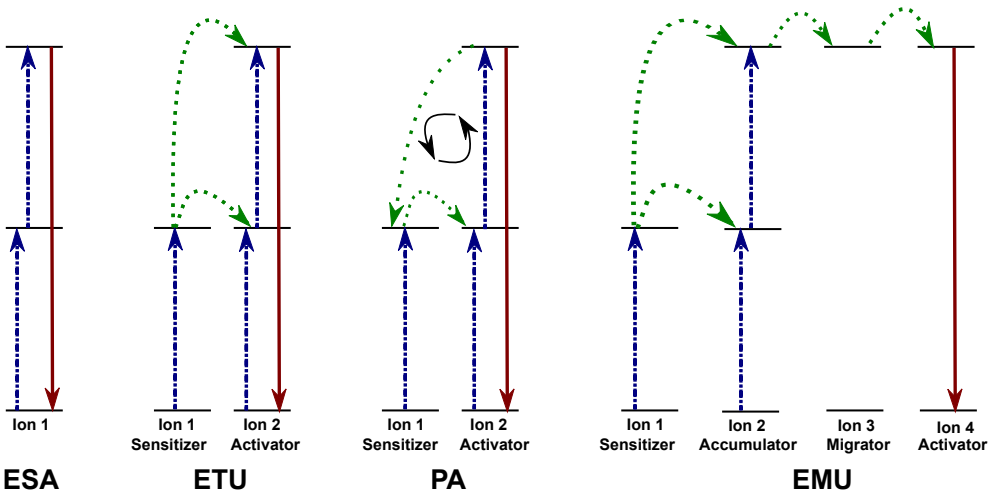

Figure 1.10: Schematic of different upconversion mechanisms excited state absorption (ESA), energy transfer upconversion (ETU), photon avalanche (PA) and energy migration-mediated upconversion. The dashed/dotted (blue), dashed (green) and full arrows (red) represent photon excitation, energy transfer or relaxation and emission processes, respectively [9, 10].

ESA upconversion mechanism is a single ion mechanism based on a sequential absorption of two photons. As shown in Figure 1.10, an electron is excited from a ground state (G) to a metastable intermediate state (E1) during a ground state absorption (GSA) process. Subsequently, a second photon excites the electron from the intermediate state to a higher exited state (E2), resulting in an upconversion emission when electron is transferred from E2 back to G. The two photons involved in an ESA upconversion can have different energies, which is different from two photon phenomenon in which the photons should be exactly

the same. ESA is the simplest upconversion mechanism and is not dependent on the concentration of rare earth (RE) ions, consequently, this is the most probable mechanism in samples with low concentration of rare-earth (RE) ions [9].

ETU mechanism in principle is similar to ESA since it requires at least two sequential photons, with the difference that in ETU two ions participate in producing the upconversion emission, as shown in Figure 1.10. The first ion, sensitizer (energy donor), is responsible for absorption of excitation photons, and the second ion, activator (energy acceptor), emits the upconversion photon. First, the sensitizer ion is excited to energy state E1 through a ground state absorption. Second, the sensitizer ion energizes the activator ion to E1 state through a nonradiative transfer, while itself relaxes to the ground level. Third, the excited sensitizer transfers another photon to the activator through a second nonradiative transfer which excites the activator from E1 to E2. Consequently, the upconversion emission relaxes the activator ion back to G. The upconversion efficiency in ETU is related to dopant concentration that is related to the average distance between neighbouring sensitizer and activator ions [9, 99].

The third upconversion mechanism is PA in which an unusual pumping mechanism that requires excitation intensity above a certain threshold leads to an upconversion emission. As illustrated in Figure 1.10, a non-resonant weak GSA populates the excited state E1 of the first ion, which is followed by a resonant ESA that populates the excited state E2. Next step in PA is the cross-relaxation between an excited and a neighbour ion at the ground state,

resulting in the transfer of both ions to their E1 intermediate state. Then, electrons from both ions get promoted to the E2 excited state. Series of further cross relaxation processes between the two ions will occur after-ward resulting in an exponentially increasing population of E2 which can produce a strong upconversion emission [9, 8].

The recently proposed upconversion mechanism, EMU as depicted in Figure 1.10, is a core-shell engineered upconversion system which enables tuning upconversion emission wavelength. Lanthanide ions designed to be used in this system are classified into four classes: sensitizers (Ion 1), accumulators (Ion 2), migrators (Ion 3) and activators (Ion 4). Like previous mechanisms, the sensitiser is used to harvest pump photons through GSA absorption, which promotes a neighbouring accumulator ion to an excited state. The accumulator ions receive electrons from the sensitiser or rarely by absorbing the pump photon to reach the highest excited level from which energy is transferred to a migrator ion thorough a non-radiative relaxation. This step is followed by a series of random hops of energy between migrator ions until the activator ion receives the energy thorough a non-radiative transfer from migrator to activator. The final step is the radiative relaxation of the activator ion resulting in an upconversion emission. An important features of EMU is that the excitation energy collected by sensitizer can be amassed in the accumulator ions by successive energy transfers, while enabling one step energy transfer to the activator. Second point is that EMU provides high conversion efficiency for low energy excitation. And finally it provides tunable upconversion emission possible by replacing activator ions with different activator ions [10].

With respect to the efficiency of the upconversion emission, these mechanisms are distinctly different. The least efficient upconversion mechanism is ESA, which is favourable only when single ion doping is needed. PA is one of the most efficient upconversion processes, but it suffers from drawbacks such as its dependence on the excitation power and the delay in response to excitation (up to several seconds) because of the numerous ESA and cross relaxation processes. In contrast, ETU is instant and independent of the excitation power and its upconversion efficiency is at least two orders of magnitude higher than ESA. EMU is a really efficient method especially for low energy excitation, but it needs state of the art structural engineering of the particles with core shell structure. Consequently, ETU is the preferred and practical mechanism for producing upconversion with more than one dopant ions [9].

1.6.2 Lanthanide Materials

The lanthanide ions, also called rare-earth, are placed separately from the other elements at the bottom of the periodic table. They include elements from lanthanum with atomic number of 57 through lutetium with atomic number of 71. The first element from lanthanide group first discovered at 1794 by Johann Gadolin [97], but it took years for scientists to classify them as it is now. These materials have some unique properties, because of which, they have found many applications in different technologies including catalysis [100, 101, 102], batteries [103], optics [104, 105], displays [106] and bioimaging [19, 107, 108, 11].

Some of the important and unique chemical and optical properties of lanthanides can be listed as:

1. They have a wide range of co-ordination numbers (generally 6 – 12, but numbers of 2, 3 or 4 are known).

2. Their $4f$ electrons are completely covered by outer $5s$ and $5p$ orbitals and are barely involved in chemical bonding and therefore their spectroscopic, optical and magnetic characteristics are not affected by ligands and environmental effects.

3. The transition between the $4f$ electrons are parity forbidden, although they do occur because of the mixing with allowed transitions such as $4f$–$5d$ transitions. When happened, the transitions between the $4f$ happens within the above-mentioned shell and therefore they are photostable.

4. As a result of number 2 and 3 the lanthanide ions possess low extinction coefficients ($< 10\ \mathrm{M^{-1}cm^{-1}}$) and long lifetime (up to several milliseconds) [11].

5. Lanthanide materials have a wide range of electronic [Xe]$4f^n$ configurations ($n = 0$ – 14), and the number of electronic levels is given by

$$\frac{14!}{n!(14-n)!} \tag{1.18}$$

and therefore as an example Gd^{3+} has 3432 energy levels. Figure 1.11 illustrates some of the energy levels of lanthanide ions [11].

6. They prefer anionic ligands with donor atoms of rather high electronegativity (as an example O and F).

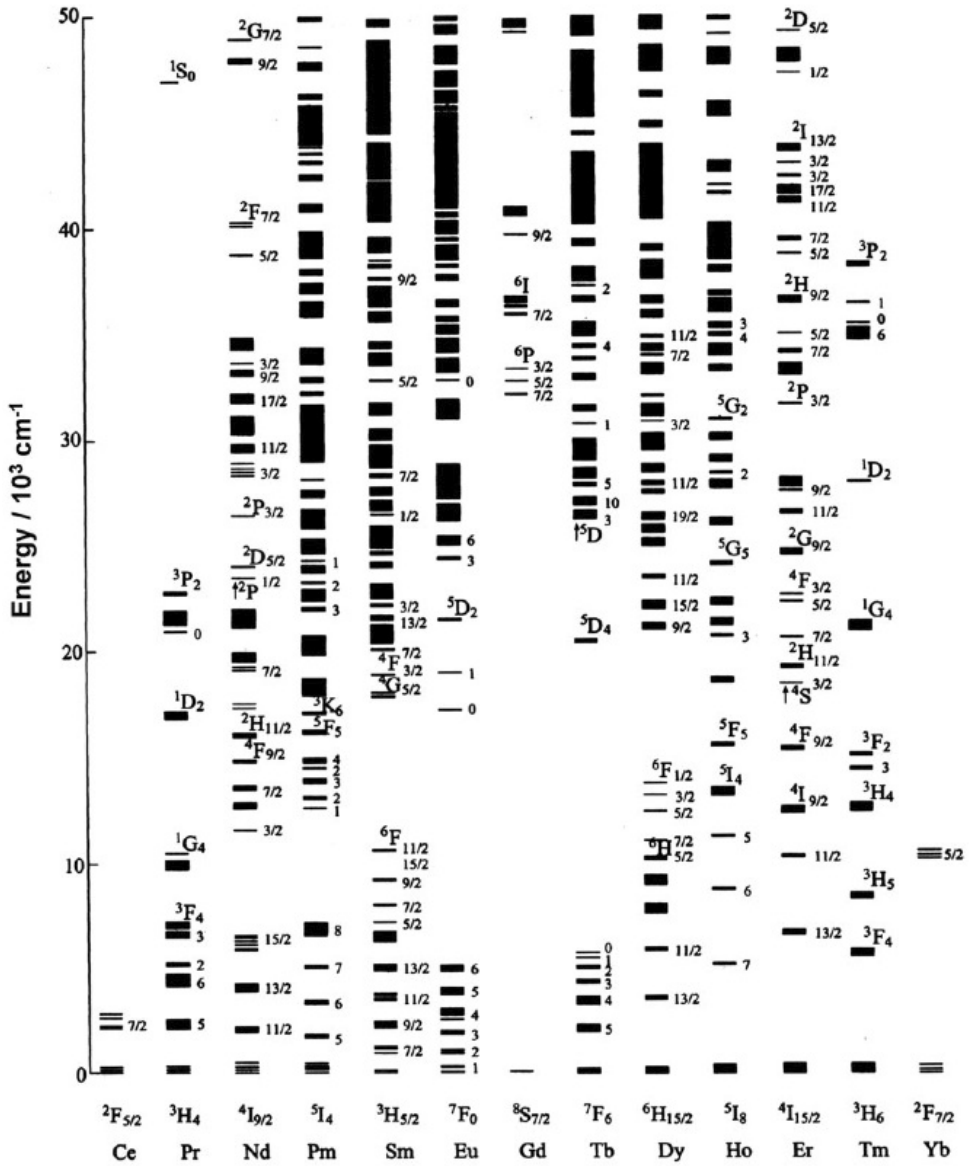

Figure 1.11: Energy level diagram for some of the Ln^{3+} ions [11].

7. All lanthanide ions show similar reactivity because of the same valence electrons.

8. Unlike organic chromophores, lanthanide ions usually have several luminescent excited states [11].

9. In lanthanide materials, from La to Lu, as the atomic number increases both atomic and ionic radii decrease, especially at the start of the series, this is called lanthanide contraction. Because of this effect lanthanide ions behave very similar in chemical reactions in which the $4f$ are conserved although they behave differently in reactions in which $4f$ electrons are not conserved [109, 97, 110].

10. All lanthanide ions, except La^{3+} and Lu3+, have unpaired electrons and show paramagnetic properties [97].

1.6.3 Structure of Upconversion Systems

An efficient upconversion happens in a system that is composed of a crystalline host with a low concentration of lanthanide ions. In ETU upconversion, selection of a proper host, activator and sensitizer is crucial for producing an efficient upconversion. The proposed theoretical energy transfer of Yb:Er and Yb:Tm systems excited with 980 nm laser beam is illustrated in Figure 1.12.

The host material plays a crucial role in the upconversion efficiency and emission profile. An ideal host material is transparent to the wavelength range of interest, has a low phonon energy, high optical stability and similar lattice structure to that of the dopant ions. Trivalent rare-earth (RE) ions, alkaline

earth ions (Ca^{+2}, Sr^{+2} and Ba^{+2}) and some transition metal ions (Zr^{+4}, Ti^{+4} and Zn^{+2}) have similar size to RE and can be used as the host material. Another important feature of a host is a low phonon energy to minimize the nonradiative energy losses. Heavy halides including chlorides, bromides and iodides exhibit low phonon energy (less than 300 cm^{-1}). Oxides have high chemical stability but suffer from relatively high phonon energy (generally more than 500 cm^{-1}) because of the stretching vibration of the host lattice. In comparison to other hosts, fluorides show an acceptable chemical stability and a low phonon energy ($\approx$ 350 cm $^{-1}$). Another important factor is the compatibility of crystal structure of the host material to that of the dopant, for example hexagonal-phase $NaYF_4$:Yb,Er is one order of magnitude more efficient in upconversion emission than the cubic form with the same dopant concentration. Considering all these issues the most efficient reported host for upconversion is the hexagonal $NaYF_4$ [9, 19].

Activator dopants, in an upconversion system, should have multiple metastable states that are available in most lanthanide ions, with the exception of La^{+3}, Ce^{+3}, Yb^{+3} and Lu^{+3}. Lanthanide ions such as Er^{+3}, Tm^{+3} and Ho^{+3} have ladder-like energy levels (see Figure 1.12) that are close to their ground levels so as to facilitate a step-by-step absorption and energy transfer required for the upconversion processes. Another important factor is the nonradiative multiphoton relaxation rate between different energy levels as given by

$$K_{nr} \propto \exp\left(-\beta \frac{\Delta E}{h\omega_{max}}\right) \tag{1.19}$$

where β is an empirical constant of the host material, ΔE the energy gap be-

tween the populated energy levels and the next lower energy level of a lanthanide ion, h the Planck's constant, and ω_{max} the highest vibrational mode of the host lattice. For example, ions such as Er^{+3} and Tm^{+3} with relatively large energy gaps, and thus, low probabilities of nonradiative relaxation are suitable activators in an upconversion system [9].

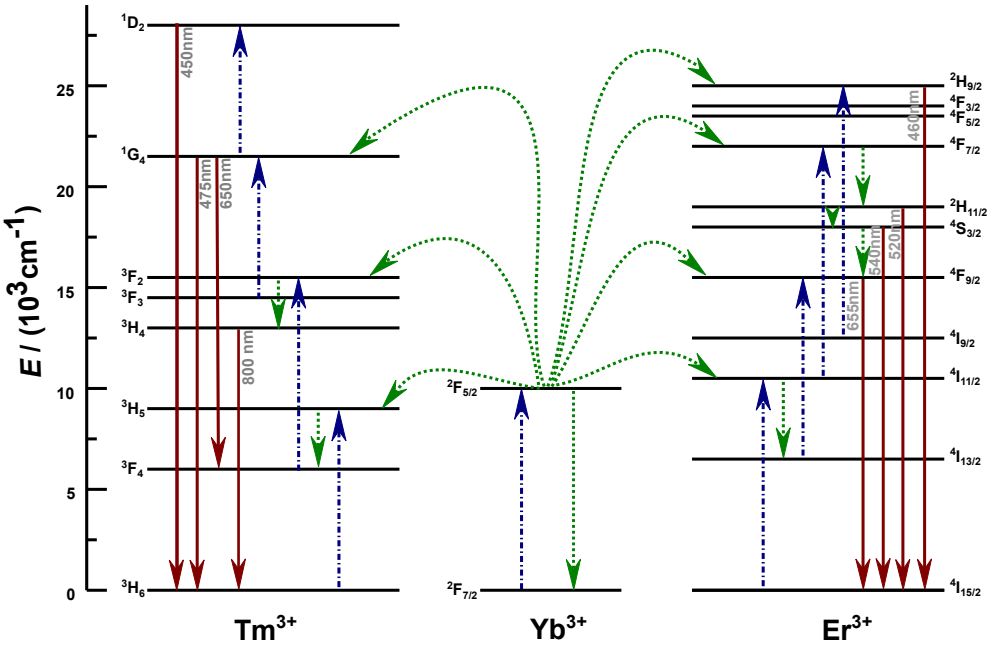

Figure 1.12: Schematic diagram of the proposed energy transfer mechanisms between Yb^{+3} as sensitizer and Tm^{+3} or Er^{+3} ions as activators. The dashed/dotted (blue), dashed (green) and full arrows (red) represent photon excitation, energy transfer or relaxation and emission processes, respectively (redrawn using [9, 12]).

In ESA mechanism with singly doped crystals, upconversion efficiency is dependent on the distance between two neighbouring activator ions and the ab-

sorption cross-section of the ions. The concentration of the activators is low and carefully adjusted due to the mutual quenching effects of the ions. In order to take advantage of a highly efficient ETU upconversion mechanism, a sensitizer ion with a sufficient absorption cross-section in the NIR region is often co-doped with the activators in the host lattice. For example, a trivalent Yb ion with only one energy level in $4f$ level of $^2F_{5/2}$ (as seen in Figure 1.12) has a large absorption cross-section located at around 980 nm and a good resonance with f-f transition of activators ions, making it a suitable sensitizer. To get an efficient upconversion, the concentraion of sensitizer is chosen to be high (20 mol %), in comparison to the low activator content ($<$ 2 mol %) [9].

Figure 1.12 illustrates the schematic of upconversion mechanism by co-doping Yb^{+3} with Er^{+3} or Tm^{+3}. The main emission peaks of Erbium doped particles are located at 520, 540 and 655 nm corresponding to $^2H_{11/2} \rightarrow^4 I_{15/2}$, $^4S_{3/2} \rightarrow^4 I_{15/2}$ and $^4F_{9/2} \rightarrow^4 I_{15/2}$ transitions, respectively. For Thulium doped particles typical emission peaks are at 450, 475, 649 and 800 nm associated with $^1D_2 \rightarrow^3 H_6$, $^1G_4 \rightarrow^3 H_6$ and $^3H_4 \rightarrow^3 H_6$ transitions, respectively. The blue emissions of the Tm^{+3} doped particles are 4- and 3- photon processes, while Er^{+3} and other Tm^{+3} emissions are often two-photon processes [9, 12].

1.7 Multimodalities

As described in Section 1.2, different modalities have been applied for the purpose of molecular imaging including nuclear modality, magnetic modality and

optical modality. Table 1.1 (Page 7) summarizes advantages, disadvantages and some other properties of these different modalities. An important point is that any of these modalities have some unique advantages not provided by other modalities, which are accompanied by some important limitations. For example, optical imaging is a highly sensitive and fast method, while it suffers from low spatial resolution and poor tissue penetration. On the other hand, magnetic resonant imaging provides a high spatial resolution and no tissue penetration limit, but suffers from relatively low sensitivity and slow image acquisition time. Therefore, by mixing these two modalities, it is possible to overcome the limitations of each and achieve more efficient molecular imaging for particular specimen.

Figure 1.13 demonstrates the concept of multimodality. Different type of information is retrieved using different imaging modalities. Magnetic resonant imaging provides comprehensive anatomical images, but it lacks biochemical, physiological and especially molecular information. Nuclear imaging (e.g., PET) or optical imaging, on the other hand, are highly sensitive for molecular, biochemical and physiological information, while they lack anatomical information. Thus, by adopting multimodal systems such as MRI/optical or MRI/PET, it is possible to have a comprehensive imaging that provides both anatomical and biochemical information on the subject. Note that for an efficient multimodal imaging, a modality with a high sensitivity, such as PET or optical, is combined with a modality with a high spatial resolution, for example MRI or CT, and modalities with similar properties should be avoided as the combined data may make the analyses and understanding of the result more complex [111, 112].

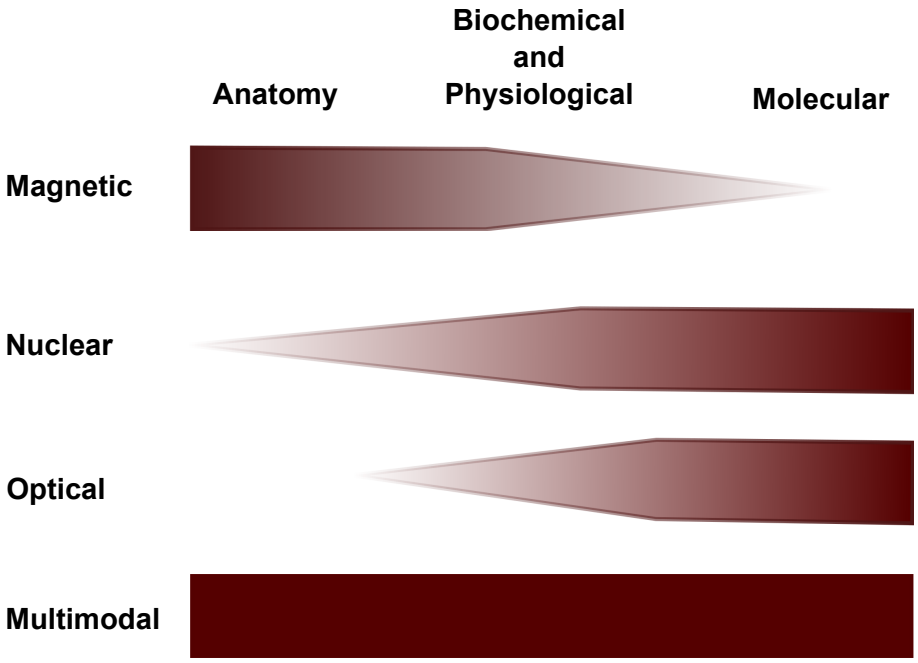

Figure 1.13: Schematic of informaiton retrieved from different imaging modalities and how multimodality can be used to cover limitations of each modality to provide more complete information.

1.8 Potential Targets for Optical Molecular Imaging

The main objectives of molecular imaging, including early disease detection, better and more accurate screening and diagnosis, targeted therapy and drug delivery, targeted therapeutic monitoring and treatment follow-ups are never feasible without proper molecular targets and tags with high affinity and specificity [20, 22]. Development of target molecules and targeted nanoparticles suit-

able for molecular imaging is a laborious and multidisciplinary research area. In this section, before introduction of some possible targets for clinical application, we look at targeting molecules or tags which can be attached to nanoparticles through polyethylene glycol (PEG), avidin-biotin and streptavidin.

Antibody molecules are the classical targeting agents in immunohistochemistry and also in molecular imaging with nanoparticles. Although novel methods for production of rodent monoclonal antibodies, rodent recombinant monoclonal antibodies, and partly humanised antibodies have improved purity and availability of these antibodies, the relatively large size (12 nm) and the immunogenicity of their fragment crystallisable region F_C (i.e., the tail of an antibody that interacts with cell surface receptors and complement system and eventually activates the immune system) have encouraged the development of antibody fragments for molecular imaging applications [22]. Normal antibodies are approximately 150 kDa in size and therefore are slowly removed from circulation and can accumulate in normal tissues. Antibody fragments, in contrast, have molecular weight of around 25 kDa which better accommodate *in vivo* requirements. Recently, synthetic antibody fragments have been produced [113, 114], which eliminate the need for animals and can increase their production speed.

Oligonucleotides (aptamers), another possible targeting molecules, are small synthetic nucleic acid molecules, either DNA or RNA, with molecular weight as low as 5-10 kDa, which can act as ligands for proteins. Advantages of aptamers are rapid and inexpensive synthesis, high homogeneity and stability over time [115, 116]. Peptides are another class of novel targeting molecules,

which provide all advantages of aptamers. Examples of peptides targeting molecules are arginine-glycine-aspartic acid sequence (RGD) to detect integrins [117, 118, 119], NC-1900 for vasopressin [120] and trans-activating transcriptional activator (TAT) peptides for enhancement of cellular internalization and mitochondrial detection [121, 122]. Lectins are the last important targeting groups that have a molecular weight between 12 to 150 kDa and can pass blood-tissue barriers [22, 123].

There are many possible targets for molecular imaging in clinical applications and basic biomedical research. Molecular imaging is attractive in many clinical areas including oncology, cardiovascular disease and neurology. Targets for detecting cancer in oncology include detecting cancer phenotypes such as increases in metabolism, proliferation, angiogenesis, hypoxia and apoptosis, and detection of specific protein markers on tumour cells and tumour associated cells, such as tumour angiogenic vessels and stroma. Some examples of targets for tumour phenotypes are increases in protein synthesis, glucose transporters and choline transporters and thymidine uptake in DNA/RNA synthesis (target for tumour cell proliferation). Examples of tumour specific proteins are integrins, somatostatin receptors, oestrogen receptors and androgen receptors related to angiogenesis, neuroendocrine tumours, breast cancer and prostate cancer.

In cardiovascular field there are many examples of readily available targets with clinical applications. Some important examples are cathepsin K, collagen, elastin, fibrin and VCAM-1 for detecting atherosclerosis, adrenergic neurotransmitters for heart failure and cardiac sympathetic neurones for cardiac

sympathetic innervations [124, 125]. Neurological imaging is another important clinical area using molecular imaging and although the blood brain barrier is a major obstacle to overcome, there are many possibilities in this field that can have crucial effects on our understanding and treatments of neurological problems. Examples of useful targets are dopamine receptors, β-amyloid, NK-1 receptors, dopamine transporters and dopamine metabolism with clinical application in schizophrenia, Alzheimer's disease, depression, anxiety and addiction [126, 127, 128, 129].

Integrins are one of the most important and interesting targets of molecular imaging for detection of cancer and cardiovascular diseases. Integrins are a large group of surface receptors with important responsibilities in normal and pathological cells. Some of the important roles of integrins in tumour cells include increasing tumour cell migration, invasion proliferation and survival. Also integrins play an important role in angiogenesis and regulation of tumour cells by managing crosstalks between growth hormones and tumour cells or tumour-associated cells. Because of these important roles that integrins have in cancer physiology, they can be employed as targets for detection and even treatment of cancers. Different integrins are associated to different tumours: for example, expression of $\alpha_v\beta_3$, $\alpha_5\beta_1$ integrins in Melanoma increase lymph node metastasis, in Breast cancer, $\alpha_6\beta_4$ expression enhances tumour size and grade and decreases patient survival, and $\alpha_v\beta_3$ causes bone metastasis. Consequently, detection and suppression of integrins can facilitate early detection, better staging and screening and better treatment. Important integrins in angiogenesis are $\alpha_v\beta_3$, $\alpha_1\beta_1$, $\alpha_2\beta_1$, $\alpha_4\beta_1$, $\alpha_5\beta_1$, $\alpha_6\beta_1$, $\alpha_9\beta_1$ and $\alpha_6\beta_4$. Nanoparticles can be

used for molecular imaging by functionalization with targeting molecules. For instance, arginine-glycine-aspartate (RGD) peptide can be used to detect $\alpha_v\beta_3$ integrins [130, 131, 132].

1.9 Conclusion

As described in this chapter, molecular imaging could have revolutionary effect on biomedical *in vivo* and *in vitro* imaging. For an efficient molecular imaging it is important to choose a desirable modality, apply targetable probes and select a crucial target. Between all different modalities optical and magnetic are the safest and most favourable, but because of technological difficulties these two modalities are the least clinically applied for molecular imaging. As an example optical modality suffers from lack of penetration depth which limits its application to superficial targets. This problem could be address by using the NIR biological window in which absorption and scattering of light in tissues are limited. On the other hand both optical and magnetic modalities needed biocompatible, specific, sensitive and stable probes to provide enough signal to be detected. Nanoparticles, because of their unique properties have the potential to replace conventional contrasts and enhance the applicability of molecular imaging. Although in recent years discoveries of novel nanoparticles with unique properties, such as QDs, overcome many limitations of the conventional imagining contrasts, but these nanoparticles also have some drawbacks that opens the necessity of discovery of new nanoparticles.

Upconversion nanoparticles apply non-linear optical phenomenon and therefore could be excited by light in near infrared (NIR) portion of spectrum to emit photons in NIR or visible ranges. NIR excitation not only enable deeper penetration depth but also eliminate autofluorescence problem. Quenching autofluorescence has a significant beneficial effect on the signal-to-noise ratio (SNR) and can significantly enhance potential for efficient molecular imaging. Other optical advantages of upconversion nanoprticles are narrow emission, high photostability, no bleaching, no blinking and possibility of having multicolour imaging using same NIR excitation source. On the other hand as lanthanides are the main building blocks of most upconversion systems and because these elements are considered biocompatible therefore upconversion nanoparticles are non-toxic and biocompatible. The other important aspect of upconversion nanoparticles are their applicability as potential multimodal particles. Many of the rare-earth materials have paramagnetic properties and therefore theoretically it is predictable that by using lanthanides as host and dopants for synthesis of upconversion nanoparticles it is possible to have multimodal (optical/magnetic) nanoparticles.

In conclusion, Synthesis of novel upconversion nanoparticles which could be excited in NIR and emit in NIR and have additional magnetic properties is necessary for answering to ever-increasing need for a better replacement of conventional imaging contrasts. In this work I tried different synthesis methods and characterization methods, which will be described in details in the next chapter in order to examine the possibility of having such an imaging probe.

Chapter 2

Synthesis and Material Characterization

As discussed in previous chapter, upconversion nanoparticles have the potential to play an important role as probes for *in vivo* and *in vitro* optical and multimodal molecular imaging. Although these type of nanoparticles attracted huge attention in recent years and many different synthesis methods have been reported by different groups, Section 2.1, but there is still a gap for a practical, economical and scalable method for synthesis of these kind of nanoparticles. It is also important to mention that to use the advantages of NIR biological window for bioimaging, nanoparticles with intense NIR to NIR upconversion is necessary, and this important requirement rarely been addressed. Therefore the ultimate goals of this work is to find a practical synthesis method which could provide a real solution for the above mention problem. Therefore I tried three different synthesis methods in this work which will be discussed in this chapter.

The first section of this chapter provides a review of different synthesis methods reported for upconversion nanoparticles with a discussion of advantages and disadvantages of each of them. This followed by a comprehensive description of three different synthesis method experienced in this work and the morphological and material characterization performed for them.

It is important to mention here that all the synthesis processes performed by myself in a chemistry lab at The Wolfson Centre in Brunel University. The scanning electron microscopy performed by myself using a Carl Zeiss EVO MA10 SEM located in London Centre for Nanotechnology (UCL). The transmission electron microscopy performed by a lab technician using a Hitachi H7600 system located in University of British Columbia (UBC). The dynamic light scattering experiment (DLS) measurements performed by my self using DynaPro Titan systems located in University of British Columbia (UBC). The ICP-OES experiments performed by MEDAC ltd and XPS experiments performed by our collaborator in The University of Birmingham.

2.1 Synthesis of Upconversion Nanoparticles

A vast number of methods including coprecipitation, thermal decomposition, hydro(solvo)thermal synthesis, sol-gel processing, combustion synthesis and urea homogeneous precipitation have been reported for synthesis of upconversion nanoparticles [9, 19, 12]. Table 2.1 summarizes common hosts, advantages and

disadvantages of each method. In some cases a mixture of two methods are used for synthesis of specific of nanoparticles. Post synthesis processes are used as well for development of upconversion nanoparticles with controlled particle size, chemical composition or surface functionalization.

Table 2.1: Synthesis methods of upconversion nanoparticles and their advantages and disadvantages [9, 19, 12].

Method	Example Hosts	Advantagess	Disadvantages
Coprecipitation	LaF_3, $NaYF_4$, $LuPO_4$, $YbPO_4$	Fast growth No need for costly equipment Easy procedure	Post-heat treatment required Ultra-small particles produced
Thermal decomposition	LaF_3, $NaYF_4$ GdOF	Narrow size distribution High quality particles Monodisperse particles	Expensive precursors Hydrophobic final product Toxic by-products
Hydro(solvo)thermal	LaF_3, $NaYF_4$, $La_2(MoO_4)_3$ and YVO_4	Economic precursors No need for post heat treatment Excellent control over size and shape	Autoclave required
Sol-gel preocessing	ZrO_2, TiO_2, $BaTiO_3$, $Lu_3Ga_5O_{12}$ YVO_4	Economic	High temperature annealing required High aggregation rate
Combustion	Y_2O_3, Gd_2O_3 La_2O_2S	Time saving Easy to perform	Considerable aggregation Poor morphology control
Flame Synthesis	Y_2O_3	Time saving Low cost	Sensitive to flame temprature
UBHP	Y_2O_3	Low cost No specific equipment required	Heat treatment required Hydrophobic products

Perhaps the easiest and most convenient method for producing ultra-small particles is co-precipitation, which has been used by several groups for synthesis of nanoparticles (5-10 nm) with a narrow size distribution. While having no need for costly equipment and complicated procedures, this method has a fast growth rate and requires post-annealing processes. In a typical process, solution of lanthanide salts is injected into a solution of the host material. Ex-

amples of hosts used in this method are LaF_3, $NaYF_4$, $LuPO_4$ and $YbPO_4$ [9, 133]. Particle size and growth rate can be regulated by using capping ligands or chelating agents such as polyvinylpyrrolidone (PVP), polyethylenimine (PEI) or ethylenediaminetetraacetic acid (EDTA) [134]. In particular, PEI provides a good platform for direct surface functionalization of nanoparticles with bioligands [135]. A heat treatment step is required as post processing, which is one of the disadvantages of this method.

Thermal decomposition is another synthetic method that produces highly monodispersed particles with no need for post-annealing processes. In a typical procedure, metal precursors, mostly trifluoroacetat, are thermolysed together with oleic acid and octadecene. Oleic acid acts as the primary solvent that prevents agglomeration of particles and octadecene acts as the high boiling solvent (350 °C). The advantages of oleate-based synthesis include narrow particle size distribution, high luminescence efficiency and the high phase purity of the particles. Although this method produces high quality particles, it requires expensive air sensitive precursors, results in mostly hydrophobic particles and has toxic by-products [44, 54] . Examples of the reported hosts for this method are LaF_3, $NaYF_4$ and GdOF [11, 53, 136].

The hydro(solvo)thermal method is a good method for preparation of highly crystalline materials at much lower temperature and with no need for post annealing. The process is performed in an autoclave reaction vessel that maintains the required temperature and pressure for a desired period of time. By keeping solvents in temperatures and pressure above their critical point, the autoclave

enhances the solubility of solid and increase the reaction rate between solids. Since the reaction happens in a closed cylinder, growth monitoring is virtually impossible. Particle size and morphology can be manipulated in this method by using polyol- or micelle-mediation. Some of the popular hosts reported for this method include LaF_3, $NaYF_4$, $La_2(MoO_4)_3$ and YVO_4 [137, 138].

Another synthesis method used for production of upconversion materials especially for thin-film coating is sol-gel process. This method is based on hydrolysis and polycondensation of metal alkoxide or acetate precursors. To enhance the quality of crystal formation of the particles post synthesis high temperature annealing is required. Particles derived from sol-gel method are not suitable for bio-purposes due to the tendency of the crystals to aggregate [7, 57]. This method has been reported for different hosts such as ZrO_2, TiO_2, $BaTiO_3$, $Lu_3Ga_5O_{12}$ and YVO_4 [9, 139].

In contrast to time consuming sol-gel and solvo(hydro)thermal methods, combustion synthesis is fast and provides oxide particles by exothermic chemical reaction (temperatures ranging between 500 °C and 3000 °C) which spreads through the reaction material in an autonomous way. Draw backs of combustion synthesis include substantial particle aggregation and formation of amorphous particles. The particles size and shapes depend on the reaction temperature which is governed by the ratio of the metal ions to chemical fuel ratio. In a typical combustion synthesis, hydrazine or glycine are used as fuel or reducing agents. Examples of reported hosts include Y_2O_3, Gd_2O_3 and La_2O_2S [140, 141, 142].

Another fast and time-saving synthesis method reported is flame synthesis. Flame synthesis is a one-step and continuous method for low-cost synthesis of nanomaterials. The typical host for this method is Y_2O_3 and its main drawback is the sensitivity of the particle size, morphology and photoluminescence intensity to the flame temperature [143].

Finally, the urea homogeneous precipitation method is a fast and low cost method with no need for expensive equipments. This method will be described in details in the following section. The drawbacks of this method is the requirement of heat treatment and the hydrophobic nature of the final products. The typical host used for this method is Y_2O_3 [144].

2.2 Urea Homogeneous Precipitation Method

Urea homogeneous precipitation (UHP) method is used for synthesis of several metal oxide complexes. This method was first reported by Tang *et al.* in 1937 [145] for synthesis of near monodispersed aluminium sulfate particles. The first report of synthesis of metal oxide nanoparticles using UHP was by Salutsky and Quill in 1950 [146]. Owing to its low cost and low processing temperature and the possibility of getting finer particles in comparison to the other methods, many groups investigated synthesis of metal oxides including rare-earth oxides using UPH [147, 148, 149, 150]. Recently, UHP method has been used for synthesis of mixed lanthanide oxide nanoparticles [151, 144, 152]. In general, UHP

takes advantage of a slow release of anions (mainly OH^- and $CO_3{}^{2-}$) from urea decomposition at temperatures above 83 °C. The release of anions in a solution containing metal cations form precipitation through nucleation and growth mechanisms explained by La Mer model [153]. The La Mer model emphasises that a single burst of nucleation happens above the point of supersaturation of reaction solution, which is then followed by a slow progressive growth, therefore defining a strict separation between nucleation and growth steps. This model does not hold for all cases as it is reported that aggregation of fine particles can produce structures with different size and morphology by varying the synthesis condition [150, 144].

The proposed reaction mechanism for synthesis of Gd_2O_3 particles is assumed to have two steps [150], namely:

1. Urea Decompostion:

$$(NH_2)_2CO \rightarrow NH_4^+ + OCN^- \tag{2.1}$$

$$OCN^- + 2H_2O \rightarrow CO_3^{2-} + NH_4^+ \tag{2.2}$$

$$CO_3^{2-} + H_2O \rightarrow HCO_3^- + OH^- \tag{2.3}$$

$$HCO_3^- + H_2O \rightarrow H_2CO_3 + OH^- \tag{2.4}$$

$$H_2CO_3 \rightarrow CO_2(g) + H_2O \tag{2.5}$$

2. Precipitation:

$$Gd^{3+} + OH^- + CO_3^{2-} + 1.5H_2O \rightarrow Gd(OH)CO_3 \cdot 1.5H_2O \tag{2.6}$$

Therefore, the overall reaction can be summarized as

$$Gd^{3+} + 1.5(NH_2)_2CO + 5H_2O \rightarrow Y(OH)CO_3 \cdot 1.5H_2O + 3NH_4^+ + 1/2CO_2(g) \tag{2.7}$$

The important factor in any chemical precipitation is the supersaturation degree S, given by [144]

$$S = a_A a_B / K_{sp} \tag{2.8}$$

where a_A and a_B are the activity of the partially hydrolyzed cation ($[\mathrm{Ln(OH)}_x(\mathrm{H_2O})_y]^{3-x}$, $x + y$=6, Ln=any Lanthanide atom) and anion ($\mathrm{CO_3}^{2-}$), respectively, and K_{sp} the solubility product constant. The nucleation starts only if S reaches the critical supersaturation S^* and as the aqueous solubility of a lanthanide complex increases with decreasing ionic radii of $\mathrm{Ln3}^{3+}$. As a result of the lanthanide contraction law, i.e., a lanthanide with a smaller ionic radii has larger K_{sp} (for example, Y has a larger K_{sp} than Gd), the possibility of a stable precipitation is higher for Gd than for Y [144]. In a mixed-lanthanide synthesis process, the average ionic radii and concentration of the ions define the supersaturation value.

The homogeneous nucleation rate, R_N, is another important factor related to supersaturation S^* via

$$R_N = A \exp\left(\frac{-16\pi\sigma_{sl} v^2}{3k^3 T^3 \ln^2 S}\right) \tag{2.9}$$

where R_N is the number of nuclei formed per unit time per unit volume, σ_{sl} the surface tension at the liquid solid interface, v the atomic volume of the solute, k the Boltzmann constant and T temperature [151]. Consequently, if all synthesis parameters are kept constant, a lanthanide with a larger ionic radii is more likely to precipitate through nucleation than through growth and therefore it produces smaller and denser particles.

In a practical sense, factors that will significantly affect size and shape of the Y_2O_3 particles in UHP method are [150, 151, 144]:

1. Concentration of the rare-earth solution: This can dramatically change the particle size, varying from 65 to 140 nm in concentration range between 0.005 and 0.025 M by increasing nucleation rate. But the lanthanide concentration can also increase the growth rate and therefore concentrations higher than 0.025 M cause severe agglomeration of the particles. At concentrations lower than 0.02 M the zeta potential is about 13 mV, but as concentration increases the zeta potential drops dramatically and saturates to a value of 2-3 mV. The reduced zeta potential implies rapid agglomeration of the precipitated particles. As a result, the lanthanide concentration has to be between 0.005 and 0.02 M and the solution needs to be subjected to forced dispersion to increase critical upper concentration in order to get homogeneous monosipersed particles.

2. Urea concentration: By increasing urea concentration from 0.04 to 4 M particle size decreases from 220 to 100 nm. The underlying mechanism is the increase in concentration of anions such as $CO_3{}^{2-}$ and OH^- in more concentrate urea solution, leading to higher nucleation and less subsequent growth due to lower concentration of cations. Extremely high urea concentration can cause rapid precipitation and inter-particle aggregation. The precipitation rate increases with urea concentration increases of up to 3 M and saturates beyond this value.

3. Reaction temperature has significant effect on precipitation rate, but has minimal effect on the size and shape of the particles.

4. Solution pH is a controlling factor for the particle morphology as severe coagulation occurs at pH < 2. By increasing the reaction pH to more than 3, it

is possible to produce well-separated monodispersed particles. The precipitation rate is low at low pH, increases with pH and reaches a plateau at pH > 3.

2.2.1 Synthesis of Gd_2O_3:Yb^{3+}/Er^{3+}, Gd_2O_3: Yb^{3+}/Tm^{3+}, Y_2O_3:Yb^{+3}/Er^{3+} and Y_2O_3:Yb^{3+}/Tm^{3+}

As illustrated in Figure 2.1 in a typical synthesis process, 10 mmol of $Gd(NO_3)_3$, 3 mmol of $Yb(NO_3)_3$ and 0.25 mmol of $Er(NO_3)_3$ are dissolved in 150 ml of distilled (DI) water in a 500 ml flask. Another flask is used to make a 2 molar aqueous solution of urea. Both solutions are placed in an ultrasonic bath and ultrasonicated at room temperature for 30 minutes to get homogeneous and clear solutions. The rare-earth solution is then heated in a water bath to 60°C followed by adding 150 ml of 2 M urea solution. The reaction temprature is raised to 88°C and maintained for about 20 minutes in which the color of the solution changes from clear to bluish tint and finally to milky white. The total reaction time including the time for the solution to reach the reaction temperature is 40 minutes. The milky mixture is then crash cooled using an ice bath and stored at room temperature for 48 hours. The sedimented white nanoparticles are separated by centrifugation at 8000 rpm for 10 minutes. Then, the supernatant liquid is decanted off and nanoparticles are further purified by centrfugation wash with DI water twice, isopropyl alcohol (IPA) once and again with DI water. Finally, the nanoparticle precipitates are dried in a vacuum oven at 100°C for 3 hours, followed by a final heat annealing step at 900°C for one hour in a furnace. The white powder is cooled down to room temperature and used in characterization experiments.

Table 2.2: Synthesis molar ratio of Gd_2O_3: Yb^{3+}, Tm^{3+} samples.

	T1	T2	T3	T4	T5	T6
Gd (mmol)	10	10	10	10	10	10
Yb (mmol)	0.6	3	0.6	0.6	3	3
Tm (mmol)	0.1	0.25	0.1	0.25	0.1	0.25
urea (M)	1	1	2	2	2	2

Table 2.3: Synthesis molar ratio of Gd_2O_3: Yb^{3+}, Er^{3+} samples.

	E1	E2	E3	E4	E5	E6
Gd (mmol)	10	10	10	10	10	10
Yb (mmol)	0.6	3	0.6	0.6	3	3
Er (mmol)	0.1	0.25	0.1	0.25	0.1	0.25
urea (M)	1	1	2	2	2	2

For synthesis of Tm^{3+} doped nanoparticles $Tm(NO_3)_3$ is used instead of $Er(NO_3)_3$. Similar process is used for making different molar ratio of Gd_2O_3:Yb^{3+}/Er^{3+} and Gd_2O_3:Yb^{3+}/Tm^{3+} by changing the molar ratio of the precursors used in the synthesis. We synthesise samples with 1 molar urea solution to examine the effect of urea concentration on synthesis of nanoparticles. Similar methods are also used for synthesis of Y_2O_3: Yb^{+3}/Er^{3+} and Y_2O_3: Yb^{+3}/Tm^{3+} by replacing $Gd(NO_3)_3$ with $Y(NO_3)_3$. Tables 2.2 and 2.3 summarize different molar ratio of dopants and urea used for synthesis of different samples prepared in this work.

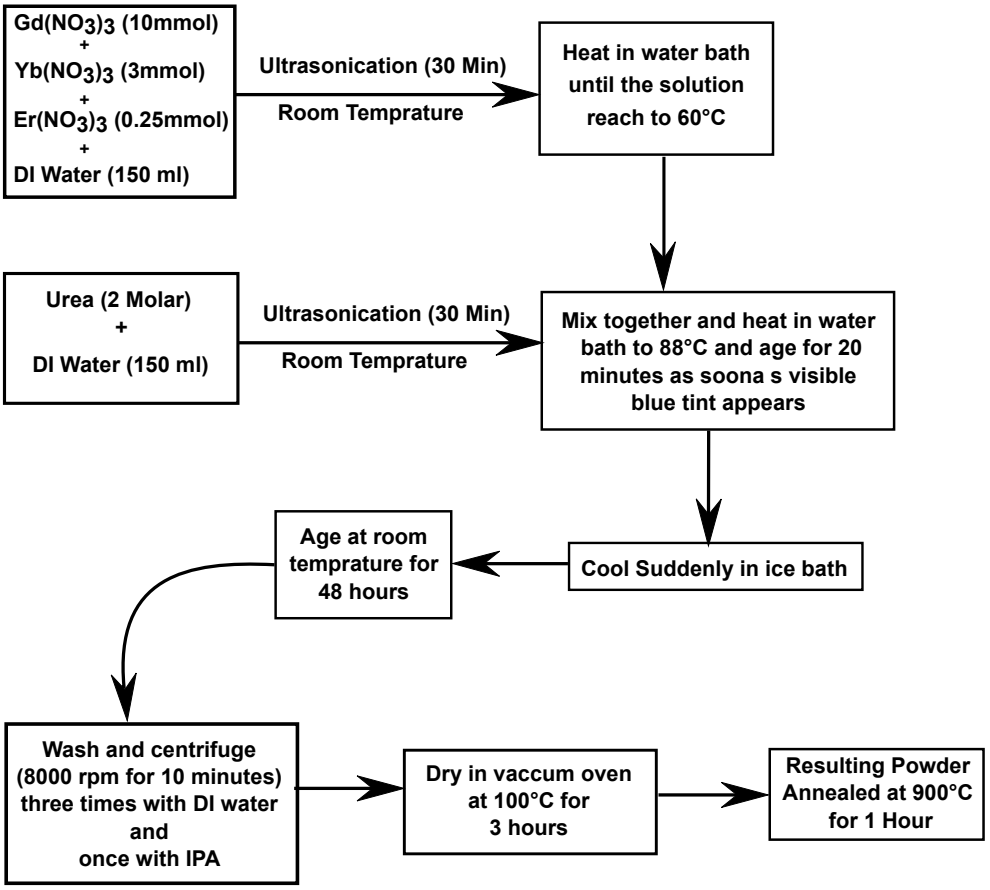

Figure 2.1: Synthesis flowchart of upconversion nanoparticles using urea homogeneous precipitation method.

2.2.2 Electron Microscopy Results

Figure 2.2 and the left part of Figure 2.4 illustrate the scanning electron microscope (SEM) photomicrographs and the size distribution of Gd_2O_3:Yb^{3+}/Er^{3+} samples (E1-E6) synthesized using urea method. Sample E1 and E2 are synthesized using 1 molar urea stock and have different concentration of dopants. E1 is doped with 0.6 mmol of Yb^{3+} and 0.1 mmol of Er^{3+} ions, while E2 is doped with 3 mmol of Yb^{3+} and 0.25 mmol of Er^{3+}. The other samples E3,

E4, E5 and E6 are synthesized with 2 molar urea solutions. The pre-synthesise dopant (Yb:Er) molar ratios are 0.6:0.1, 0.6:0.25, 3:0.1 and 3:0.25 for E3, E4, E5 and E6, respectively. As seen in the size distribution figure in addition to SEM micrographs, the Er doped particles are spherical and monodispersed and the size distribution of the particles are between 60 nm to 200 nm, depending on the precursor and urea concentration, as other synthesis parameters including reaction pH, temperature, time and annealing process are kept constant for all of them. For the sample E1, the size distribution are between 100 and 180 nm with an average particle size of 160 nm, while for the sample E2 particles have narrower size distribution (80 to 100 nm) with an average size located around 80 nm. The smallest particle size in this set of samples belongs to sample E6 with size range of 60-100 and the average particle size of 80 nm. Sample E4 has the widest size distribution between 80 and 200 nm with the average size at 120-140 nm.

Figure 2.3 and the right side of Figure 2.4 demonstrate the SEM photomicrograph and the size distribution of Tm^{3+} doped Gd_2O_3:Yb^{3+} samples. Sample T1 is doped with 0.6 mmol of Yb^{3+} and 0.1 mmol of Tm^{3+} ions, while T2 is doped with 3 mmol of Yb^{3+} and 0.25 mmol of Tm^{3+}, but both synthesised using a 1 molar urea solution. Sample T3, T4, T5 and T6 are synthesised with 2 molar urea solution with dopant molar ratio (Yb:Tm) of 0.6:0.1, 0.6:0.25, 3:0.1 and 3:0.25, respectively. Similarly to Er doped samples, Tm doped samples are spherical and monodisperse with size range of 60 to 180 nm. sample T1 have the largest particles with an average size of 160 nm and the widest size distribution, while sample T6 has the smallest particles with an average size of 70 nm.

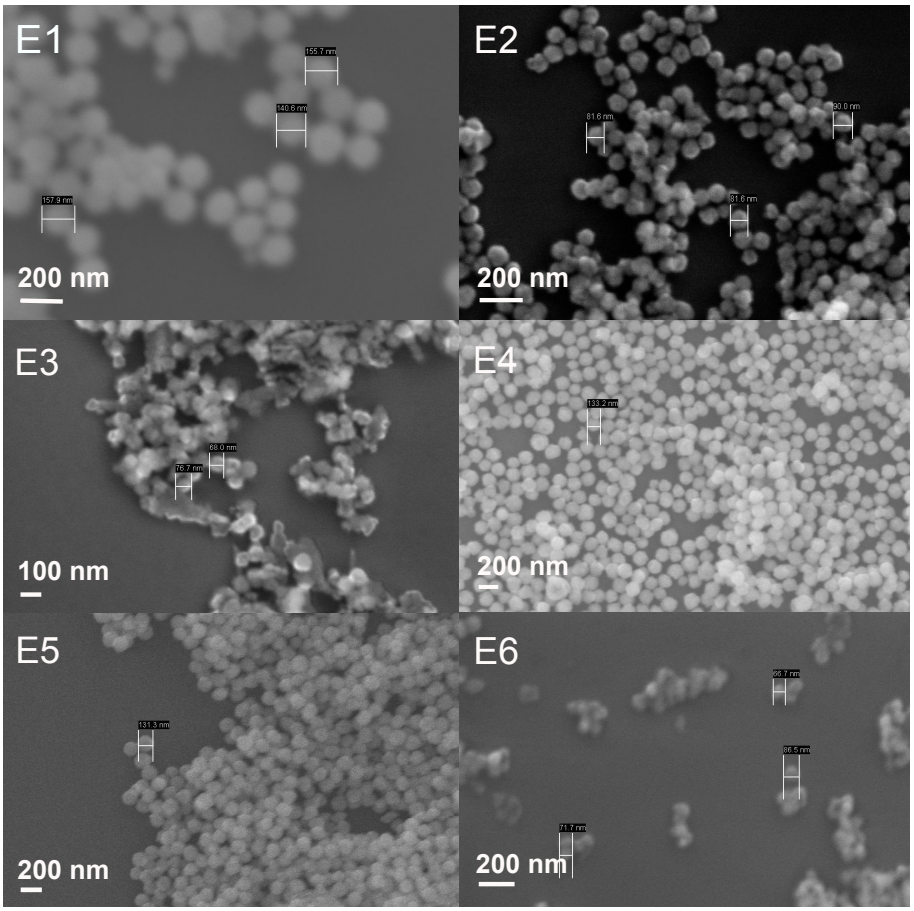

Figure 2.2: SEM photomicrographs of Gd_2O_3:Yb^{3+}, Er^{3+} samples synthesized using UHP method. Samples E1 (10:0.6:0.1 mmol) and E2 (10:3:0.25 mmol) are synthesized using 1 M urea solution, while samples E3 (10:0.6:0.1 mmol), E4(10:0.5:0.25 mmol), E5 (10:3:0.1 mmol) and E6 (10:3:0.25 mmol) are synthesized using 2 M urea solution.

The transmission electron microscopy (TEM) images of sample E4 is illustrated in Figure 2.5. TEM photomicrographs confirm spherical monodispersed nanoparticles with rough surfaces and size of 100 nm attached to the TEM

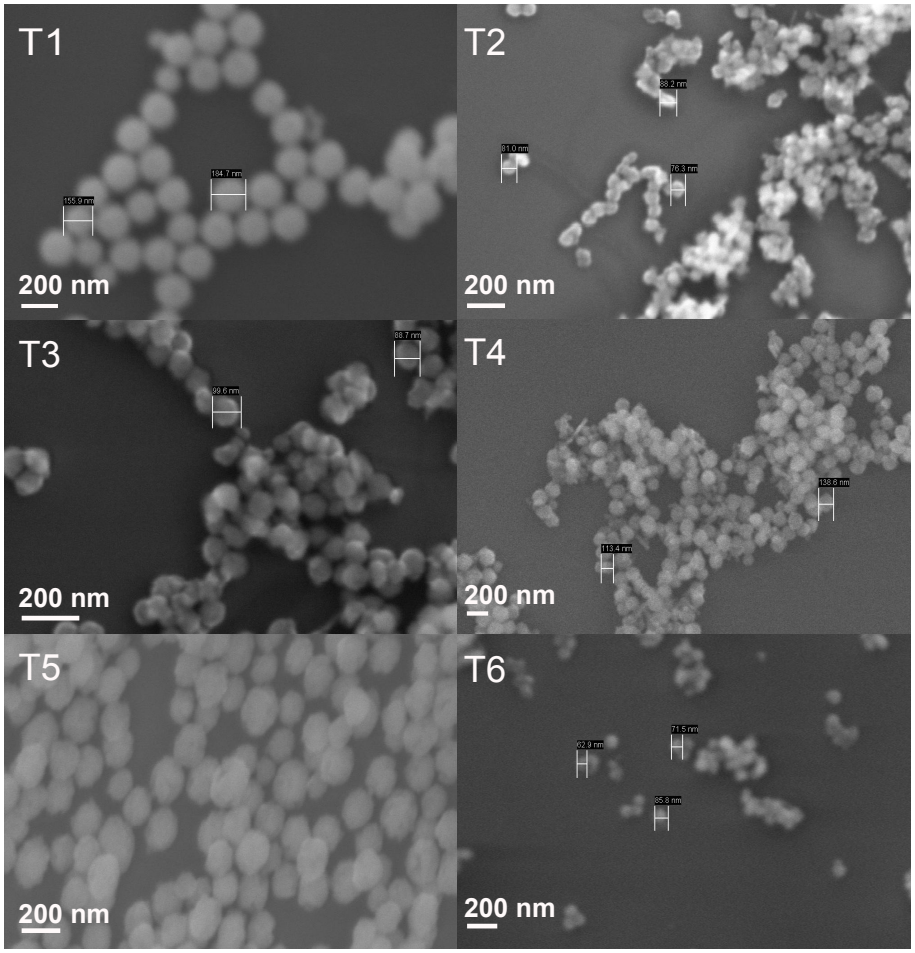

Figure 2.3: SEM photomicrographs of Gd_2O_3:Yb^{3+}, Tm^{3+} samples synthesized using UHP method. Molar ratios of Gd:Yb:Er / Urea are 10:0.6:0.1 mM / 1 M for T1, 10:3:0.25 mM / 1 M for T2, 10:0.6:0.1 mM / 2 M for T3, 10:0.6:0.25 mM / 2 M for T4, 10:3:0.1 mM / 2 M for T5 and 10:3:0.25 mM / 2 M for T6.

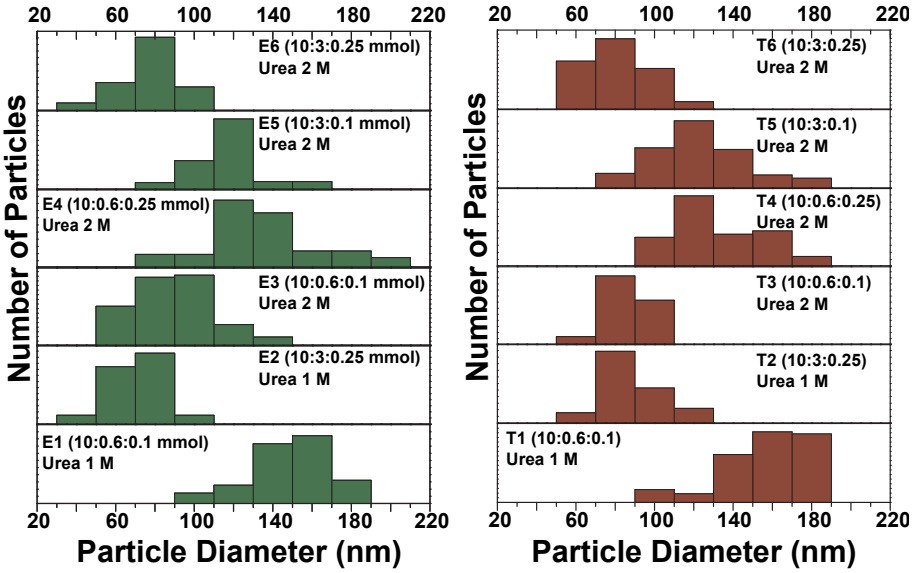

Figure 2.4: Size distribution diagram for Tm^{3+} and Er^{3+} doped Gd_2O_3 samples produced from analysis of typical SEM photomicrographs of samples E1-E6 and T1-T6.

grid. The high resolution TEM (HR-TEM) images show a crystal lattice for sample E4, Gd_2O_3:Yb^{3+}, Er^{3+} (10:0.6:0.25) with a lattice plane constant of 4.6 Å. Figure 2.6 illustrates TEM and HR-TEM photomicrographs of samples T5, Gd_2O_3:Yb^{3+}, Tm^{3+} (10:3:0.1), showing ovoid particles with size of 60 nm. T5 nanoparticles are smaller than E4 particles in TEM photomicrographs but sample E4 are more monodisperse. The HR-TEM image of T5 sample is also depicted in Figure 2.6, showing a crystal lattice constant of about 4.1 Å.

Considering the sample based nature of particle size and agglomoration analysis based on SEM and TEM photomicrographs, size distribution analysis is performed on dispersion of particles in aqueous solution using dynamic light

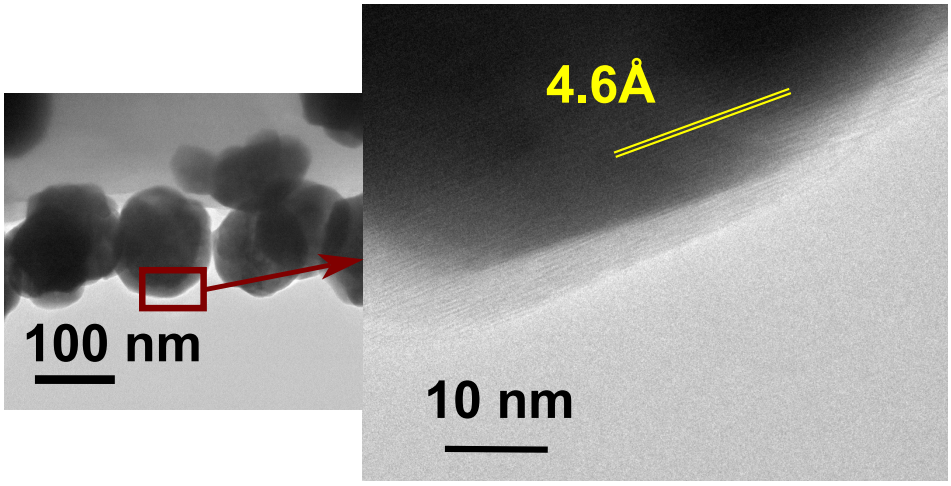

Figure 2.5: TEM photomicrograph of sample E4 Gd_2O_3:Yb^{3+},Er^{3+} (10:0.6:0.25), showing spherical particles with size range of about 100 nm and the HR-TEM photomicrograph showing the crystal structure of a particle.

scattering (DLS) using a DynaPro Titan system on samples E3, E4, T5 and T6, as shown in Figure 2.7. These samples are selected as they have the highest upconversion emission intensity and performance. Scattering of light by small particles in a solution, described in details in Section 1.3.1, is the basis priniciple for DLS measurements. A small particle in a solution scatters incident light in all directions according to Rayleigh scattering. The time-dependent fluctuations of scattered light intensity is measured and related to particle size, distribution and the monodispersity of the particles. Due to the sensitivity of DLS measurements, preparation of a dilute, well-dispersed and dust-free solution is critical.

DLS samples are prepared by mixing 1 mg of each sample in 5 ml filtered DI water. The mixtures undergo an intensive ultra-sonication using Sonic Ultra-

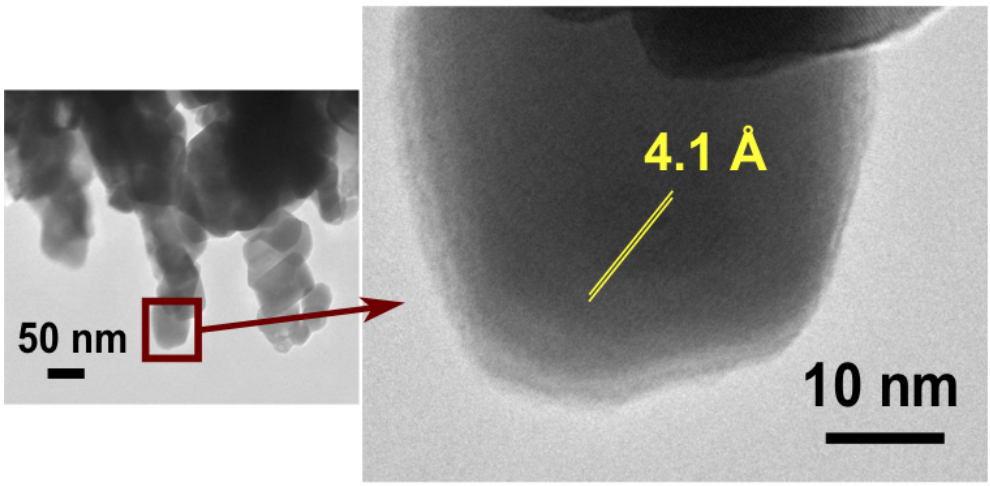

Figure 2.6: TEM photomicrograph of sample T5 Gd_2O_3:Yb^{3+},Tm^{3+} (10:3:0.1), showing spherical particles with size range of about 60 nm and the HR-TEM photomicrograph showing the crystal structure of a particle.

sonicator VX750 for 10 minutes to prepare a well-dispersed and homogeneous solution. The solution were then diluted 10 times and filtered again for DLS measurements. Figure 2.7 illustrates the size distribution results for selected samples. Tm^{3+} doped samples T5 and T6 provide very similar distribution graph with a size range of 50 to 500 nm although the main peaks are at around 100 and 125 nm. Samples E3 and E4 show smaller particles in comparison to T5 and T6 with the highest peak for particles with diameter of less than 100 nm for sample E3 and at around 100 nm for sample E4. Er^{3+} doped samples show a narrower size distribution with not many peaks located more than 300 nm in comparison to samples T5 and T6 that demonstrate an exponential decrease in the number of particles as the diameter increases from 150 to 500 nm. These results signify that the particles have acceptable aqueous dispersibility that is important for bioimaging applications. To reduce agglomeration issues for

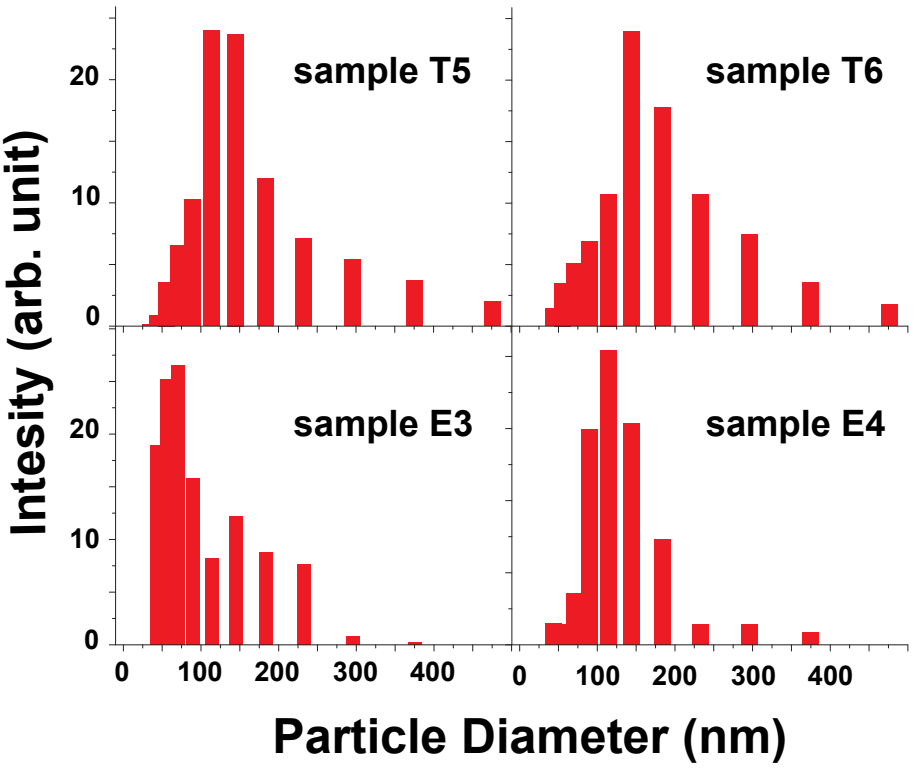

Figure 2.7: Size distribution diagram for sample T5, T6, E3 and E4 measured using dynamic light scattering.

bioimaging, surface modification methods such as those reported by Zako *et al.* [154] can be used.

In our experiments, we also tried Y_2O_3 as host to synthesise upconversion nanoparticles using UHP method. Figure 2.8 illustrates the SEM photomicrographs form the Y_2O_3:Yb^{3+},Tm^{3+} and Y_2O_3:Yb^{3+},Er^{3+}. Both samples are synthesized using 1 M urea stock and molar ratio of 10:0.6:0.1 for Gd:Yb:Tm or Gd:Yb:Er, respectively. The particles are spherical with similar morphology and size of Gd_2O_3 nanoparticles described previously. The issue with using

Y_2O_3 as the host for upconversion nanoparticles is that the emission is far less intense as compared to Gd_2O_3 particles, and the Tm doped Y_2O_3 do not emit in the range detectable by our detectors.

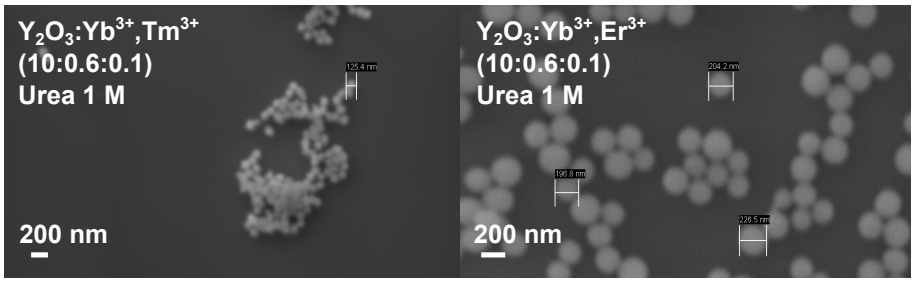

Figure 2.8: SEM photomicrograph of Y_2O_3:Yb^{3+}, Tm^{3+} and Y_2O_3:Yb^{3+}, Er^{3+} samples synthesized using UHP method. Molar ratio for both samples are 10:0.6:0.1 with 1M urea, showing similar particle shape as that of Gd_2O_3 samples.

2.2.3 ICP Spectroscopy

Inductively coupled plasma optical emission spectrometry (ICP-OES) can provide important information regarding the elemental composition of our samples. ICP is performed on all samples using a Varian Vista MPX ICP-OES system (Medac Ltd). ICP-OES is one of the most commonly used sensitive elemental analysis tools for determining trace concentrations of elements of a sample by using electromagnetic (light) radiation emitted from or absorbed by atoms of a sample. Every element has its own characteristic set of electronic energy levels and therefore its own unique set of absorption and emission wavelengths. In optical emission spectrometry (OES), the sample is subjected to high temper-

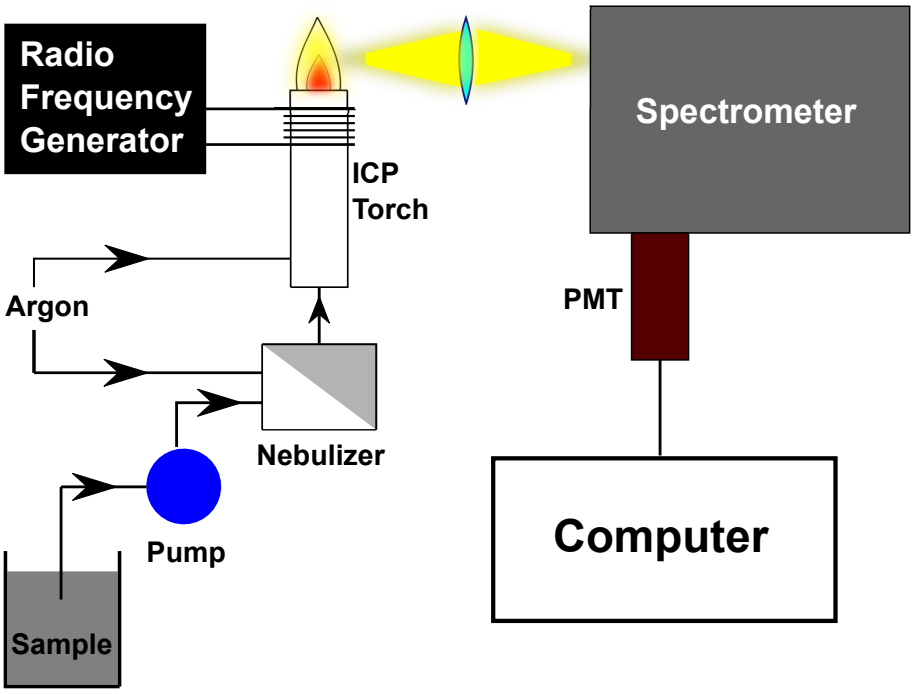

Figure 2.9: Schematic of the major components of a typical ICP-OES spectroscopy system (adapted from [13]).

atures that lead to excitation and ionization of atoms in the sample. Excited atoms decay to lower energy states through non-radiative or radiative energy emission. In OES, the intensity and spectrum of the emitted energy is used to determine the concentrations of the elements of interest [13]. Figure 2.9 illustrates the schematic of major components of a typical ICP-OES instrument. One of the most important advantages of ICP-OES over other spectroscopy and elemental methods is that the thermal excitation can populate a large number of different energy levels for different elements at the same time. All of the excited atoms and ions can emit their characteristic radiation at nearly the same time, enabling selection of different emission wavelengths for an element and simulta-

neous measurement of emission from different elements.The detection limits for different elements are generally given by μg/L (ppb) range [13].

Table 2.4: ICP spectroscopy results and calculated elemental atomic ratio of Gd_2O_3: Yb^{3+}, Er^{3+} samples.

		E1	E2	E3	E4	E5	E6
ICP Results (%)	Gd	70.97	74.74	78.91	76.42	60.6	66.02
	Yb	10.28	6.13	5.25	6.42	23.89	15.24
	Er	1.76	1.9	0.68	1.78	0.6	0.89
	O	16.99	17.23	15.16	15.38	14.91	17.85
	C	< 0.1	< 0.1	< 0.1	< 0.1	< 0.1	< 0.1
	H	< 0.1	< 0.1	< 0.1	< 0.1	< 0.1	< 0.1
	N	< 0.1	< 0.1	< 0.1	< 0.1	< 0.1	< 0.1
Calculated Atomic Ratio	Gd	0.45	0.47	0.501	0.485	0.385	0.42
	Yb	0.059	0.035	0.03	0.037	0.138	0.088
	Er	0.01	0.011	0.004	0.01	0.003	0.005
	O	1.06	1.077	0.948	0.961	0.932	1.116

The results of the ICP-OES spectroscopy for Gd_2O_3: Yb^{3+}, Tm^{3+} and Gd_2O_3: Yb^{3+}, Er^{3+} synthesised with different concentration of dopants and urea are summarized in Tables 2.4 and 2.5, respectively. The ICP results shows the concentration of each element in each samples while the calculated atomic ratio are calculated considering atomic mass of each element. We have tested C, H and N elements in order to assure that the purification and annealing steps removed these elements from the samples and only Gd_2O_3 doped with other

lanthanide dopants remain in our samples. The reported concentration of C, H and N are less than 0.1 and could be considered as the detection limit of the system.

Table 2.5: ICP spectroscopy result and calculated elemental atomic ratio of Gd_2O_3: Yb^{3+}, Tm^{3+} samples.

		T1	T2	T3	T4	T5	T6
ICP Result (%)	Gd	70.28	74.79	72.54	73.82	55.29	66.17
	Yb	12.02	9.58	9.66	8.37	29.06	15.63
	Tm	2.55	0.79	1.85	2.85	0.86	1.02
	O	15.5	14.84	15.95	14.96	14.79	17.18
	C	< 0.1	< 0.1	< 0.1	< 0.1	< 0.1	< 0.1
	H	< 0.1	< 0.1	< 0.1	< 0.1	< 0.1	< 0.1
	N	< 0.1	< 0.1	< 0.1	< 0.1	< 0.1	< 0.1
Calculated Atomic Ratio	Gd	0.44	0.475	0.461	0.469	0.351	0.42
	Yb	0.069	0.055	0.055	0.048	0.167	0.09
	Er	0.015	0.004	0.01	0.016	0.005	0.006
	O	0.947	0.928	0.997	0.935	0.924	1.07

As seen from the results of Table 2.4 for Er^{3+} doped Gd_2O_3: Yb^{3+} samples, samples synthesised using 2 M urea solution has improved chance for getting appropriate dopant concentrations reflecting the initial ratio of the precursors used in comparison to samples synthesised using 1 M urea (E1 and E2). For example, by comparing samples E3 and E6, a gradual increase in dopant concentration of E6 is observed than that of E3, accompanied by a decrease in Gd concentration.

Table 2.5 provides the elemental analysis results for Tm^{3+} doped samples. The results show a higher dopant concentration for samples T6 in comparison to T3 that has similar molar ratio of the dopants, signifying the capability of UHP method in successful incorporation of dopants in the final product. Although the initial Gd^{3+} concentration of all Tm^{3+} or Er^{3+} doped samples are at 10 mmol, the concentration of Gd is lower for samples doped with higher concentration of Yb^{3+}, Er^{3+} or Tm^{3+}. This reduction can be attributed to the replacement of Gd^{3+} in the crystal structure with respective dopant ions. Additionally, the use of a 2 M urea solution increases the incorporation of dopants in the final product and subsequently decreases Gd^{3+} concentration.

2.2.4 X-Ray Photoelectron Spectroscopy Results

The X-ray photoelectron spectroscopy (XPS) is based on photoelectronic effect discovered by Hertz in 1887 [14]. When photons from a light source hit a solid sample, they can eject electrons from the valance band. In XPS, high energy X-ray photons are used to interact with core level electrons from any orbital of the sample. Figure 2.10 shows the different parts of an XPS system, consisting of X-ray source, the spectrometer and a high vacuum chamber. The measured energy E_{sp} of the ejected electron at the XPS spectrometer is related to the biding energy E_b and the Fermi energy E_F according to

$$E_b = h\nu - E_{sp} - q\phi_{sp}, \tag{2.10}$$

where $h\nu$ is the energy of the primary X-ray photon and ϕ_{sp} the work function

of the spectrometer (3 to 4 eV). As E_b depends on the X-ray energy, it is important to provide a monochromatic X-ray excitation for XPS measurement, often sourcing from a narrow band X-ray sources such as Al or Mg. Since XPS is a surface analysis method, the emitted photoelectrons originate from the upper 0.5 to 5 nm surface of the sample. The depth of XPS measurements is related to the electron escape depth or electron mean free path [155].

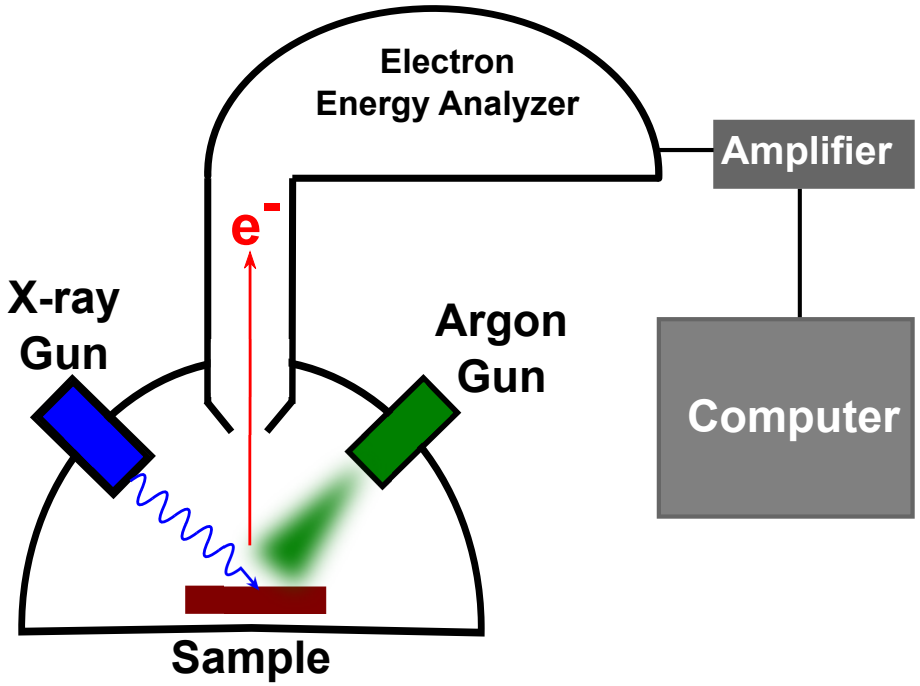

Figure 2.10: Schematic different components of a typical XPS system (adapted from [14].

In our experiments we performed XPS measurements on selected samples (T5,T6, E3 and E4) with the highest upconversion emission for both Tm^{3+} and Er^{3+} doped Gd_2O_3:Yb^{3+} samples. Figure 2.11 shows the binding energy spectrum for sample T5. The Gd 4d and O 1s peaks can be observed clearly in the

spectrum as shown in the figure. There are observed overlaps between the Gd 4p and C 1s peaks and between Yb and Tm peaks (Yb 4d with Tm 4d and Yb 4s with Tm 4s) due to similarity of the binding energy for these orbitals. An important point is the appearance of C in XPS measurements of all our samples while we did not detect any carbon in ICP-OES experiments reported in Section 2.2.3. We believe this is due to the long delay between the ICP-OES and XPS measurements and possible gradual surface absorption of CO_2 from atmosphere during this time, this is in accordance with some recently published results [156].

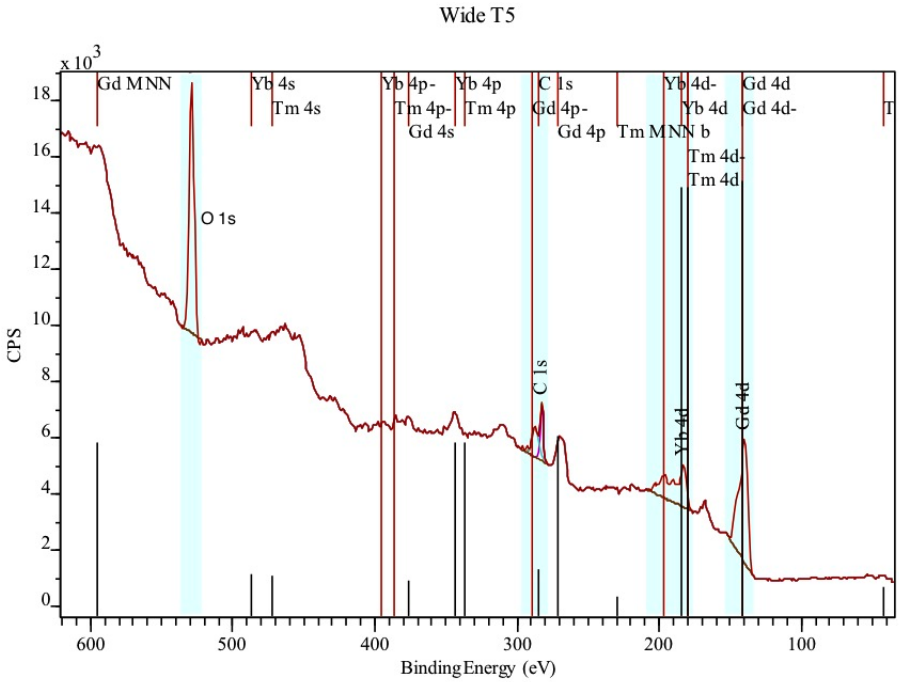

Figure 2.11: XPS result of sample T5 showing Gd 4d and O 1s peaks while there are some overlaps between Gd 4p and C 1s and also between Yb and Tm 4d peaks. The similarity and low intensity of Yb and Tm signals makes it difficult to quantify them.

Table 2.6: Atomic percentages of elements in sample T5 and T6 based on peak areas in XPS wide scan.

	Gd 4d Atomic (%)	Yb 4d Atomic (%)	O 1s Atomic (%)	C 1s Atomic (%)
T5	16.91	9.115	51.65	22.32
	18.19	9.027	53.18	19.43
	17.48	9.914	55.22	18.38
T6	16.96	4.452	46.01	32.58
	15.79	5.371	46.13	32.71
	14.16	3.752	42.58	39.5

Table 2.6 shows the atomic percentage of elements estimated from the peak areas of XPS wide scan results for samples T5 and T6. Due to small concentration of Tm dopants in these samples (0.1 mmol for T5 and 0.25 mmol for T6) and the overlap between Yb 4d and Tm 4d peaks, it is not possible to accurately quantify the atomic percent of Tm in these samples. While the XPS results generally corroborates those of the ICP-OES results (Table 2.2), some differences are observed. The average atomic percentage of Gd derived from XPS peaks is 17.52 % and 15.63 % for samples T5 and T6, repsectively. The ICP results show much higher concentration of Gd of 55.29 % and 66.17 % for samples T5 and T6, respectively. The difference in the concentrations extracted from these two experiments can be attributed to the inaccuracy of the XPS based concentrations due to the overlap between Gd 4d and C 1s peaks. Thus, Gd concentrations estimated by XPS can be significantly underestimated. More importantantly XPS measurement results provide information on the surface

composition of the particles, while ICP better represent the mass composition of the entire sample, thus the observed difference can be partly attributed to the structural differences between surface and core of the particles, as seen in the HR-TEM photomicrographs. As described in Section 2.2, during UHP method, a Gd core nucleation is followed by growth that forms the spherical particles, thus the concentration Gd is expected to decrease from core to surface. In addition, the surface is more vulnerable to absorption of CO_2 from atmosphere, affecting the Gd percentage. The atomic percentage of Oxygen in sample T5 and T6 is also higher than the estimated O_2 percentage from ICP measurements.

Table 2.7: Atomic percentages of elements in sample E3 and E4 based on peak areas in XPS wide scan.

	Gd 4d Atomic (%)	Yb 4d Atomic (%)	Er 4d Atomic (%)	O 1s Atomic (%)	C 1s Atomic (%)
E3	21.3	1.07	4.26	50.44	22.93
	20.82	1.43	2.72	53.20	21.83
	23.51	1.11	3.91	51.18	20.29
E4	22.75	0.51	3.95	53.84	18.94
	23.14	0.78	3.44	53.67	18.97
	23.67	0.92	3.54	51.78	20.09

Table 2.7 illustrates the atomic ratio of samples E3 and E4 estimated from peak areas in XPS wide scan. The average Gd percentage detected is 21.87 % for E3 and 23.18 % for sample E4, which are higher than the Gd percentage

detected by XPS for Tm doped samples (although similar molar ratios are used for Gd for both cases), but still smaller than the percentage derived from ICP results. This differences can also be attributed to the underestimation of XPS due to the overlaps between Gd 4d and C 1s. Unlike the Tm doped samples, the atomic percentage of Er dopants can be estimated at 3.63 % for E3 and 3.64 % for E4 due to better visibility of the peaks. We have detected smaller Yb atomic ratio in E3 and E4 as compared to Tm doped samples, which reflects higher Yb precursor for E3 and E4 of 0.6 mmol in comparison to 3 mmol for T5 and T6. The average atomic ratio of oxygen in sample E3 and E4 derived from XPS results is 51.6 % and 53.09 % which is much higher than the oxygen atomic percentage measured by ICP. This can be attributed to having more oxygen on the surface of the particles and also because of CO_2 absorption on the surface of the particles and overlaps between Gd 4p and C 1s peaks.

2.2.5 X-Ray Diffraction Results

X-ray diffraction (XRD) is one of the most frequently used technique for analysis of crystal structure of materials. Principally, XRD is based on Bragg's law of diffraction for an incicent X-ray beam from crystal planes with spacing d to give a constructive inteference when

$$2d \sin\theta = n\lambda, \tag{2.11}$$

where θ is the angle of incident X-ray to the surface, λ the X-ray wavelength, and n the order number of reflection. Figure 2.12 shows a schematic of X-ray diffraction system.

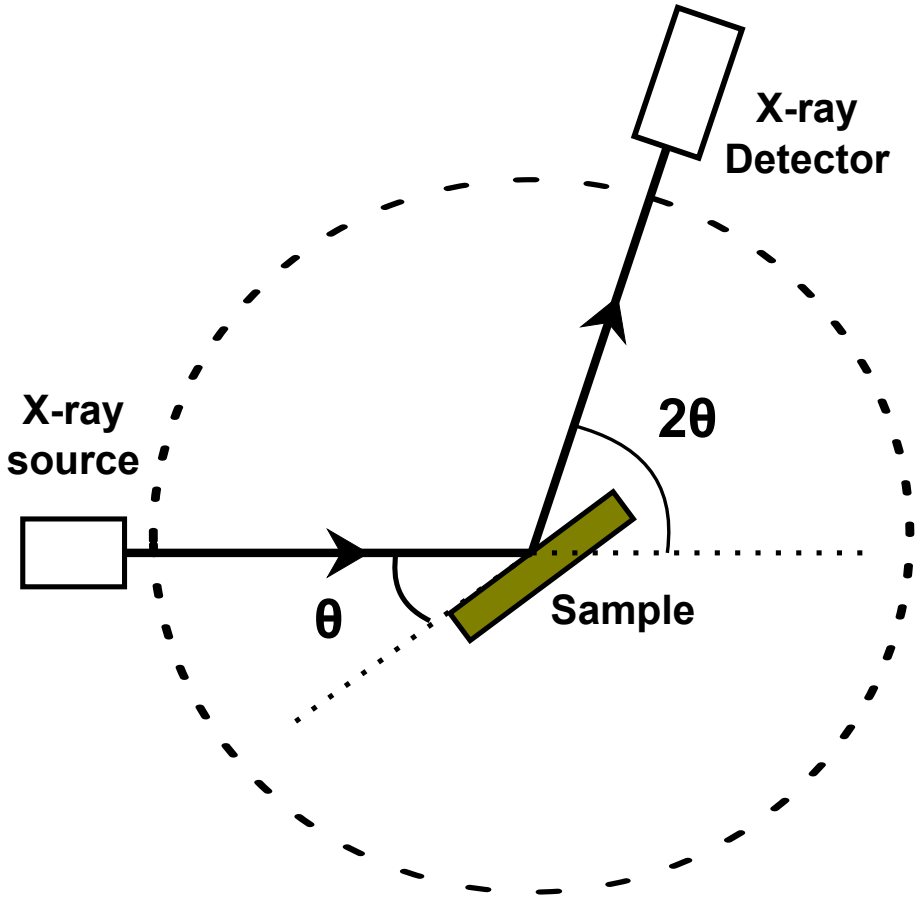

Figure 2.12: Schematic of X-ray diffraction system.

Figure 2.13 depicts the XRD results for selected Tm^{3+} doped (T1, T6) or Er^{3+} doped (E1, E6) Gd_2O_3:Yb^{3+} samples, showing peaks for crystalline Gd_2O_3 core of the particles [157, 158].

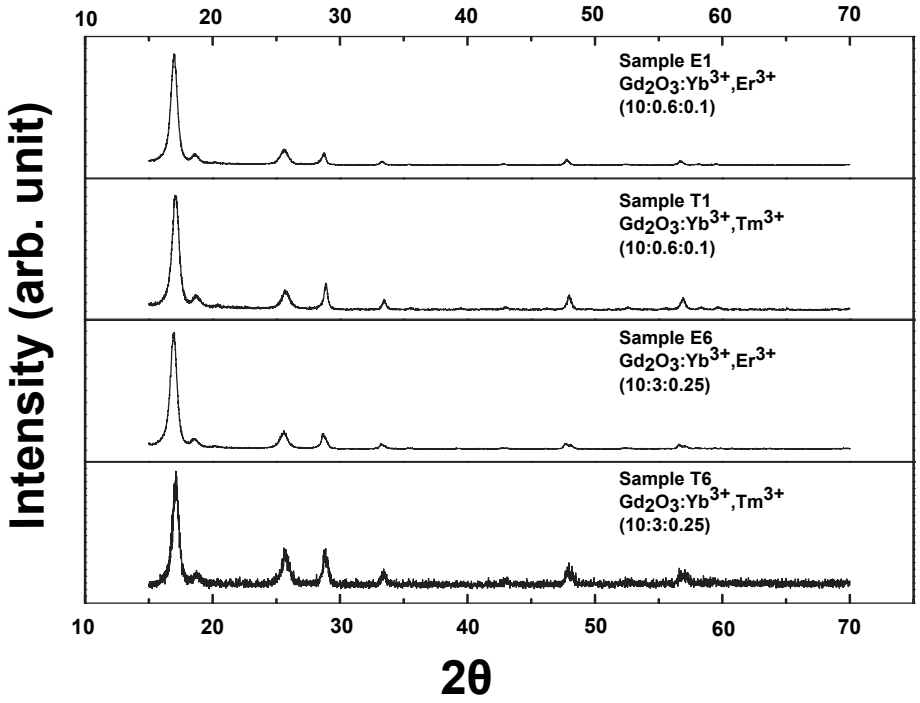

Figure 2.13: XRD results from selected Gd_2O_3:Yb^{3+} samples doped with Tm^{3+} (T1 and T6) or Er^{3+} (E1 and E6).

2.3 Organic Solvothermal Method

2.3.1 Synthesis of Y_2O_3:Yb^{3+}/Er^{3+}, Y_2O_3:Yb^{3+}/Tm3+ and ZnO:Li^{+}/ Er^{3+} Using Rare-Earth Co-ordination

The novel solvothermal method is used for synthesis of Y_2O_3:Yb^{3+}/Er^{3+}, Y_2O_3:Yb^{3+}/Tm^{3+} and ZnO:Li^{+}/ Er^{3+}. Tetramethyl heptanedionato (TMHD) rare-earth co-ordination complexes are used as metal precursors. The rare-earth co-ordination complexes are chosen because they form clear homogeneous solutions in organic solvents such as IPA. By adding ammonia to the homogeneous solution the solution becomes alkaline and therefore the organic precursours form metal hydroxides,

which subsequently convert to metal oxides during heat treatment. The proposed synthesis reactions are

$$Y(TMHD)_3 + Yb(TMHD)_3 + Er(TMHD) \xrightarrow{NH_4OH} Y(OH)_3 + Yb(OH)_3 + Er(OH)_3 + [TMHD] \quad (2.12)$$

and

$$Y(OH)_3 + Yb(OH)_3 + Er(OH)_3 + [TMHD] \xrightarrow{Heating} Y_xYb_yEr_zO_p + H_2O + NO_2 + CO_2. \quad (2.13)$$

The synthesis process is similar to the synthesis method described in the Figure 2.14, the only difference is that no surfactants are used here. In a typical synthesis 10 mmol of $Y(TMHD)_3$, 3mmol of $Yb(TMHD)_3$ and 0.25 mmol of $Er(TMHD)_3$ are mixed in 50 ml IPA in separate flasks. The solutions are vigrously stirred, heated and refluxed in an oil bath at 100°C until they become homogeneous and clear in about 30 minutes. Then all solutions are mixed in a three-necked flask and the mixture is stirred and heated at the same temperature for 1 hour, following by adding a mixture of ammonia/DI water (150/50ml) drop-wise while monitoring pH. The pH of the solution before adding any ammonia is usually about 8.10 which increases by adding ammonia and white precipitates form when pH reaches to about 12.5, at which time the sample is cooled gradually to room temperature. The big clusters and impurities are then removed using a vacuum filter and the organic solvents are removed using a rotary evaporator. Nanoparticles are then separated by centrifugation at 4000 rpm for 20 minutes. Samples are then annealed in a furnace at 800°C for 2 hours and the resulting white powder used for characterization experiments.

The same process is used for making Y_2O_3:Yb^{3+}/Tm3+ by replacing $Er(TMHD)_3$ with $Tm(TMHD)_3$. Also for producing ZnO:Li^+/ Er^{3+}, $Y(TMHD)_3$ is replaced with $Zn(TMHD)_2$ and $Yb(TMHD)_3$ replaced with Li(TMHD). Other synthesis steps remain the same for all synthesised samples.

2.3.2 Synthesis of Y_2O_3:Yb^{3+}, Er^{3+} and Y_2O_3:Yb^{3+}, Tm^{3+} with Different Surfactants (PVA, PAA, PEG)

Figure 2.14 is the flowchart of the synthesis of Y_2O_3:Yb^{3+}, Er^{3+} and Y_2O_3:Yb^{3+}, Tm^{3+} by using different surfactants including polyvinyl alcohol (PVA), polyacrylic acid (PAA) and polyethylene glycol (PEG) to manipulate size and morphology of the particles. The proposed reaction is the same as reaction 2.12 and 2.13 and the surfactant role is to cover the crystal seeds in order to limit further outgrowth of the nanostructures. Synthesis steps are similar to those used for samples with no surfactants.

2.3.3 Electron Microscopy Results

SEM photomicrographs for Y_2O_3:Yb^{3+},Er^{3+} and Y_2O_3:Yb^{3+},Tm^{3+} samples synthesised using rare-earth co-ordination precursors with no surfactant are illustrated in Figure 2.15. Both Er^{3+} doped (right) and Tm^{3+} doped (left) samples are semi-spherical microparticles with size distribution of 1 μm to 4 μm, showing much larger particles in comparison to UHP method.

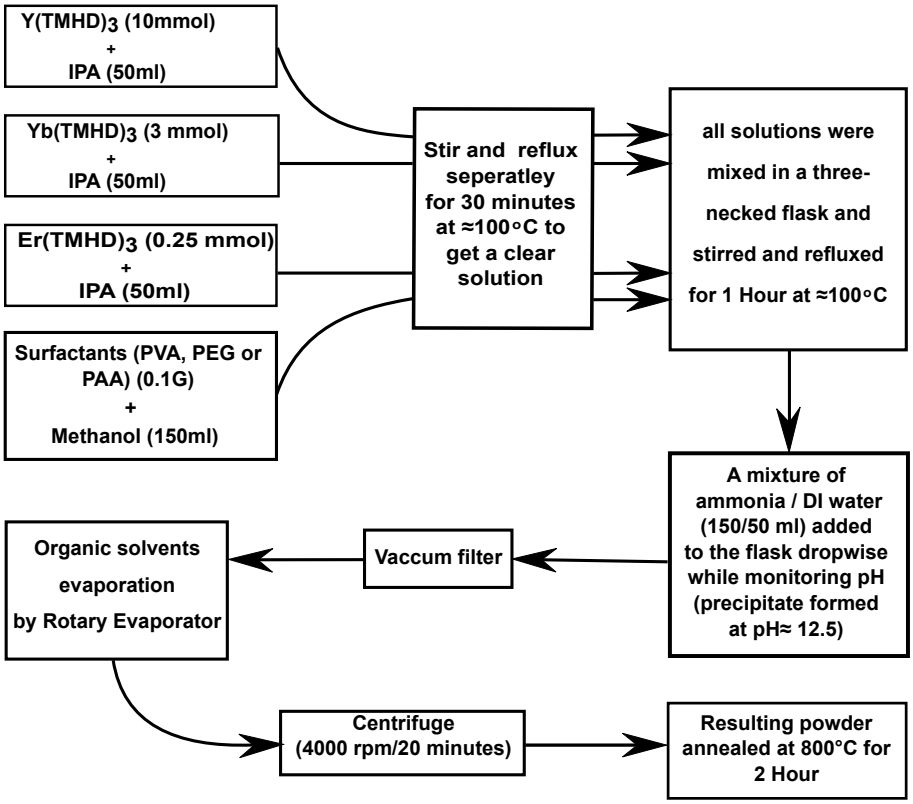

Figure 2.14: Synthesis flowchart of upconversion nanoparticles using rare-earth co-ordination as precursors with surfactants.

As described in Section 2.3.2, we have examined the effect of using surfactants to manipulate morphology and size of the nanoparticles using solvothermal method. Figure 2.16 depicts SEM photomicrographs of Y_2O_3:Yb^{3+},Er^{3+} and Y_2O_3:Yb^{3+},Tm^{3+} nanoparticles synthesised using several surfactants PAA, PVA and PEG, respectively, from top to bottom. Comparing these images with those for samples produced without surfactants shown in Figure 2.15, it is evident that surfactants dramatically reduce the size of the particles. The samples synthesised using PAA and PVA have similar morphology, consisting of clusters of particles in the size range of less than 50 nm. Samples synthesized using

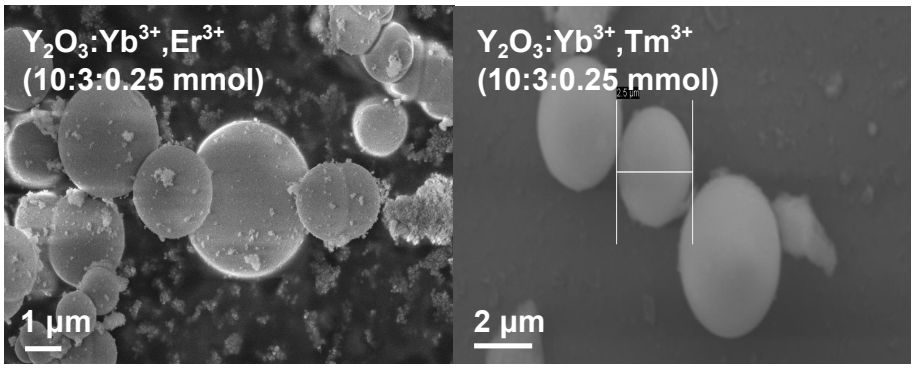

Figure 2.15: SEM photomicrograph of Y_2O_3:Yb^{3+}, Er^{3+} and Y_2O_3:Yb^{3+}, Tm^{3+} synthesized by rare-earth co-ordination precursors with no surfactants.

PEG surfactant, however, consist of far more homogeneous and monodispersed spherical and oval particles.

Figure 2.17 demonstrates SEM photomicrographs of ZnO:Er^{3+},Li^{+} samples synthesized using organic solvothermal method. For synthesis of these samples similar process to that described in Section 2.3.1 is used. But unlike spherical microparticles produced for Y_2O_3:Yb^{3+},Er^{3+} and Y_2O_3:Yb^{3+},Tm^{3+} shown in Figure 2.15, ZnO:Er^{3+},Li^{+} samples shows clusters of rod shape nanostructures with some morphological changes for different molar ratios. The ZnO:Er^{3+},Li^{+} with molar ratio of 10:0.2:0.1 mmol provides spike shape nanostructures, whereas ZnO:Er^{3+},Li^{+} with same molar ratio of Zn^{2+} and Li^{+} but doped with 0.5 mmol of Er^{3+} provide columnar rods. Figure 2.14 also display Y_2O_3 doped with Yb^{3+},Er^{3+} or Yb^{3+},Tm^{3+} demonstrating rods with diameter of about 50 to100 nm and length of more than 200 nm.

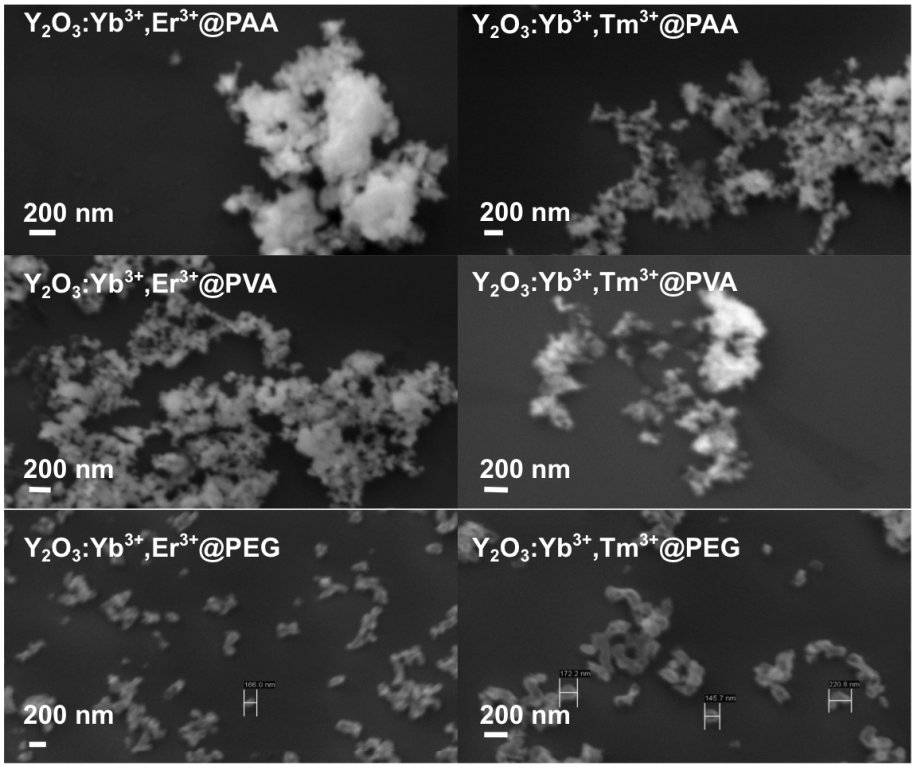

Figure 2.16: SEM photomicrograph of Y_2O_3:Yb^{3+}, Er^{3+} and Y_2O_3:Yb^{3+}, Tm^{3+} synthesized by rare-earth co-ordination precursors and different surfactants PVA, PAA and PEG for controlling size and shape of particles.

2.4 Combustion Method

2.4.1 Synthesis of Y_2O_3:Yb^{3+},Er^{3+}, ZnO:Yb^{3+},Er^{3+} Using Inorganic Precursors

Synthesis of upconversion nanoparticles are performed using combustion methods similar to what has been reported in literature [141, 140]. We synthesised a series of samples using ZnO and Y_2O_3 as the host for the nanoparticles. As dopant, we have investigated different molar concentrations and different

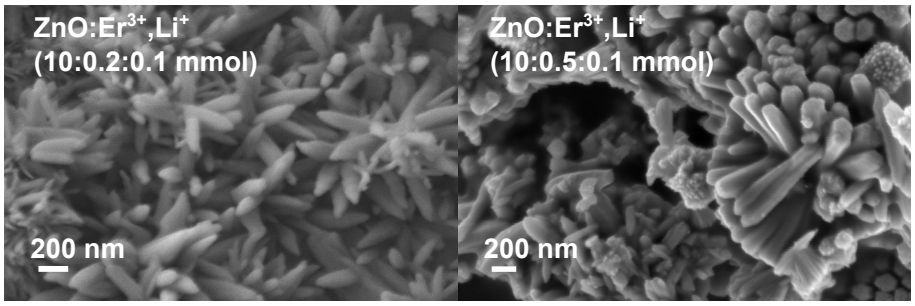

Figure 2.17: SEM photomicrographs of ZnO:Er^{3+},Li^{+} synthesized with rare-earth co-ordination precursors.

dopant combinations such as ZnO:Yb^{3+},Er^{3+} and Y_2O_3:Yb^{3+},Er^{3+}. Two molar ratios of precursor materials for ZnO:Yb^{3+}:Er^{3+} are 10:1.8:0.2 mmol and 10:3:0.25 mmol and for Y_2O_3:Yb^{3+},Er^{3+} are 10:3:0.3 and 10:3:3. The flowchart of synthesis is illustrated in Figure 2.18.

In a typical procedure, $Y(NO_3)_3$ (10 mmol), $Er(NO_3)_3$ (0.25 mmol) and $Yb(NO_3)_3$ (3 mmol) are mixed with 10 ml DI water in a flask. The mixture is magnetically stirred at room temperature for 30 minutes to form a homogenous solution. Then appropriate amounts of hydrazine or glycine is mixed with the dispersion and stirred at room temperature for an hour for Zn and Y host materials. The solvent is removed using a rotary evaporator, and the product transferred into a crucible and heated at 200°C for about 30 minutes in a furnace to remove the remaining water. Combustion occurs when the temperature is increased to 290°C in a matter of seconds. The fluffy powder that remains after the combustion is heated further to 800°C for an hour.

For the combustion synthesis of M_2O_3 samples, we use a metal nitrate (oxi-

dizer) and an organic fuel such as glycine, where M = Y, Yb or Er. The reaction is exothermic corresponding to stoichiometric reaction

$$6M(NO_3)_3 + 10NH_2CH_2COOH + 18O_2 \rightarrow$$
$$3M_2O_3 + 5N_2 + 18NO_2 + 20CO_2 + 25H_2O. \quad (2.14)$$

The molar ratio of glycine to metal nitrate compounds is 1.2:1, as suggested by literature to yield the best molar ratio for upconversion nanopowders [141]. In the case of ZnO, the synthesis conditions are kept the same, but the glycine is replaced with hydrazine as the reducing agent. The possible reaction is

$$1Zn(NO_3)_2 + 3N_2H_4 + O_2 \rightarrow 1ZnO + 6H_2O + 4N_2 \quad (2.15)$$

and the same reaction is used for other dopants including Er and Yb to produce the doped ZnO samples.

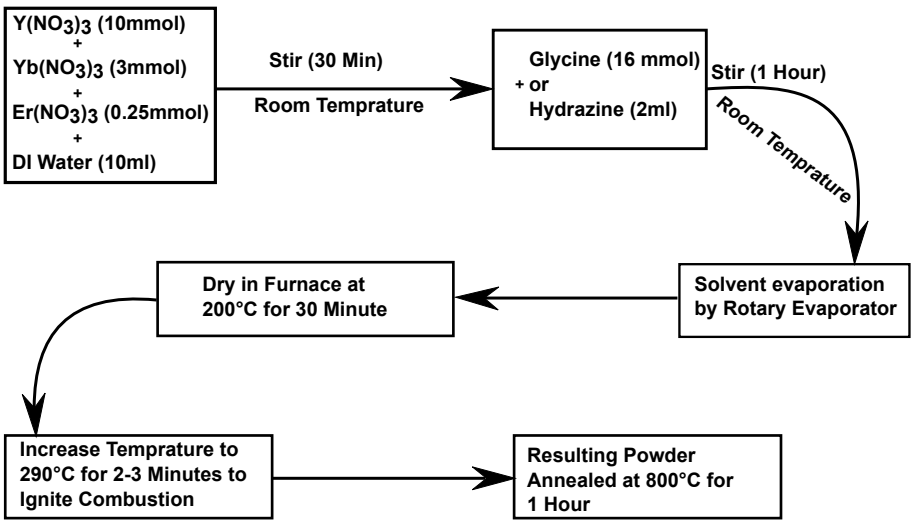

Figure 2.18: Flowchart of combustion synthesis method.

2.4.2 Electron Microscopy Results

Figure 2.19 depicts SEM photomicrographs for Y_2O_3:Yb^{3+},Er^{3+}, ZnO:Yb^{3+},Er^{3+} nanoparticles produced using combustion method. Both Y_2O_3:Yb^{3+},Er^{3+}, ZnO:Yb^{3+},Er^{3+} demonstrate clusters of bead-shaped nanoparticles with the average size of around 50 nm. From the images, it is safe to say that Y_2O_3:Yb^{3+}, Er^{3+} sample have smaller and finer nanoparticles in comparison to ZnO:Yb^{3+},Er^{3+} particles. While the combustion method is an easy and fastest method, the resultant particles suffer from severe aggregation in comparison to other methods.

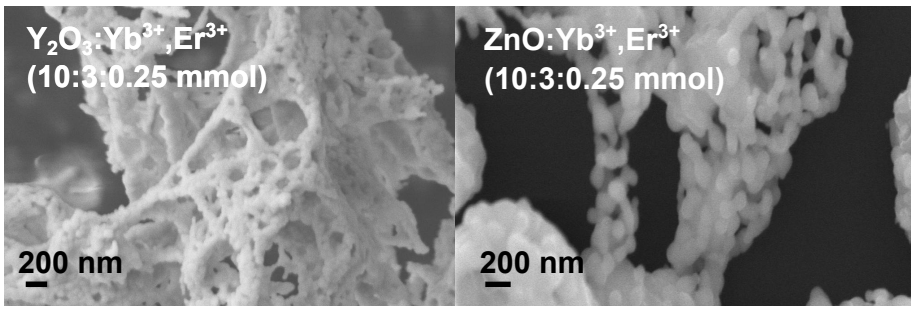

Figure 2.19: SEM photomicrographs of Y_2O_3:Yb^{3+},Er^{3+}, ZnO:Yb^{3+},Er^{3+} samples synthesized using combustion method and inorganic precursors.

2.5 Conclusion

A good synthesis method has to be easy to apply, efficient, controllable and economic. In this work I tried three different synthesis methods including urea homogenous precipitation (UHP), organic solvothermal and combustion method, in order to find the best possible way, considering synthesis equipment available. It is important to mention here that as described in Section 2.1, one of the most

common synthesis method applied for synthesis of upconversion nanoparticles by many groups recently, is hydrothermal method which have advantages such as excellent morphological control of the nanoparticles, economic process and no need for post heat treatment. The most important drawbacks of hydrothermal method is that it requires specific high pressure autoclave reactor, it is not possible to monitor synthesis process and it is not a scalable method. Because of these disadvantages and also as I did not have access to equipments required for hydrothermal method, I focused my investigation in this work on other methods described in this chapter.

UHP method is applied for synthesis of Gd_2O_3:Yb^{3+},Er^{3+}, Gd_2O_3:Yb^{3+},Tm^{3+}, Y_2O_3:Yb^{3+},Er^{3+} and Y_2O_3:Yb^{3+},Tm^{3+}. The morphological and elemental analysis performed for these samples proved that UHP method is a reliable method for producing high crystalline, monodisperse spherical nanoparticles with good correlation between dopants molar ratio in precursors and resultant particles. There were no noticeable morphological differences between samples synthesized using Gd_2O_3 or Y_2O_3 as host. Therefore, because Gd_2O_3 samples provide better optical and magnetic properties, which is discussed in the following chapters, I focused my work on synthesis of Gd_2O_3:Yb^{3+},Er^{3+}, Gd_2O_3:Yb^{3+},Tm^{3+} samples. UHP synthesis method provides several advantages such as it does not demand any fancy equipment and it uses economic precursors and water as the reaction medium, so it is an affordable, easy to apply and scalable method. The main disadvantages of this method are that it requires post heating step and the final products are hydrophobic. Thus, for bioapplications synthesized particles need to go through a surface modification

step as well.

The other method that been tried in this work was novel organic solvothermal method. The idea behind this method, that to our best of knowledge is reported for the first time, is that the rare-earth co-ordinations such as TMHD complexes are easily soluble in organic solvents such as IPA and having a homogenous mixture of dopants and host ions enhance the possibility of getting dopants in favourable places in host lattice. Using this method I synthesized different samples including Y_2O_3:Yb^{3+},Er^{3+}, Y_2O_3:Yb^{3+},Tm^{3+} and ZnO:Li^{+},Er^{3+} with different molar ratios. The synthesized particles have spherical shape with size range between 1 μm to 4 μm, with strong upconversion emission in case of Y_2O_3:Yb^{3+},Er^{3+}. As the resultant particles were larger that could be applied for bioapplications, surfactants have been tried for morphological manipulation of particles synthesized using this method. In conclusion we manage to get nanoparticles using organic solvothermal method, but as will be discussed in 3 this morphological changes also altered the optical properties of these particles. This method have advantages such as there is no need for specific equipments and the synthesis process is easy to perform. The disadvantages of this method could be named as expensive precursors, large particle size and difficulty in controlling the morphology of the particles.

Finally, I also tried combustion method for synthesis of Y_2O_3:Yb^{3+},Er^{3+} and ZnO:Yb^{3+},Er^{3+}. This conventional method is a very fast method which required inexpensive precursors and no reaction vessel. The main disadvantages of combustion method are severe aggregation and low upconversion emission.

In conclusion, considering all the advantages and disadvantages of the three different synthesis methods experienced in this work, UHP method is the most practical method with the best morphological, optical and magnetic properties for resultant nanoparticles. Morphologically, nanoparticles synthesized using UHP method are homogeneous, with acceptable narrow size distribution and good monodispersity compare with the two other methods. UHP method also is a scalable method, as reaction happened in aqueous solution, the reaction temperature is not high (83°C and there is no need for high pressure reaction condition, therefore it could be a promising method for large scale synthesis as well. At the end it is important to mention that interestingly, Gd_2O_3:Yb^{3+},Tm^{3+} samples synthesized using UHP method is the only sample synthesized in this work with pure NIR to NIR upconversion, while Tm^{3+} doped samples produced using other methods did not have detectable upconversion emission in NIR spectral region.

Chapter 3

Optical Characterization of Upconversion Nanoparticles

Optical characterization of the synthesised nanoparticles are presented in this chapter to evaluate their performance for molecular imaging in biologically significant window. As mentioned in Chapter 1 when an excitation photon is absorbed by a material, the absorbed energy takes it to an excited state,this is followed by a radiative, nonradiative or mixed relaxation process. In a radiative process, a photon is emitted during the relaxation of an electron from anThe excited to the ground state, on the other hand, in a nonradiative process is dissipated as heat generation or a chemical reaction. The radiative and nonradiative emission response of a material to optical excitation is determined by the structure and composition of materials. As a result, optical characterisation provides critical information on electronic and material properties of the synthesized materials.

In this thesis, I have described two different methods for measurement of upconversion photoluminescence in Sections 3.1 and 3.2. Measurement results for time-resolved luminescence decay are presented in Section 3.3, providing a better understanding of the optical response of the sample to pulsed excitation. Finally, upconversion multiphoton microscopy is demonstrated for synthesized samples to prove the applicability of the synthesized nanoparticles for spatially-resolved molecular imaging, as summarized in Section 3.5.

It is important to mention here that all the optical characterization experiments described in this chapter performed by my self. The FTIR system used for upconversion photoluminescence measurements was located in London Centre for Nanotechnology (LCN) while the other photoluminescence experiment setup was in electrical engineering department of University College London (UCL). The decay measurement performed using an optical set up in chemistry department of University of British Columbia (UBC) and finally the multiphoton microscopy setup was in Simon Fraser University (SFU).

3.1 FTIR System for Measurements of Upconversion Photoluminescence

As upconversion is an anti-Stokes phenomena many of conventional characterisation systems are not applicable for measurements of upconversion photoluminescence, especially, for accurate measurement of low intensity emissions. Al-

most all commercially available spectrophotometers employ monochromators to provide spectral data. And although it is possible to get high resolution photoluminescence using specific configurations such as double pass and double gratings, It is really difficult to get a high quality and high resolution upconversion photoluminescence data using conventional spectrophotometers. To overcome this problem in measurement of upconversion nanoparticles, we have introduced a novel photoluminescence setup for our experiments using a modified Bruker VERTEX 80v Fourier transform infrared (FTIR) and visible spectrometer.

In FTIR systems, a Michelson interferometer [7] is used instead of a dispersive element, such as a prism or diffraction grating, to resolve the wavelength spectrum of emitted light. In a Michelson interferometer, photons from a broad-band source is divided into two part using a beam splitter, with one beam heading toward a moving mirror and the other toward a fixed mirror. The interference of the two beams reflected from the two mirrors is constructive or destructive depending on the position of the moving mirror to produce an interfrogram for different frequencies, which can be related to the light intensity using Fourier transform. Generally, Using FTIR system for this purpose has three main advantages:

1. *Fellgett's advantage* – All wavelengths/frequencies are measured simultaneously, so a complete spectrum can be recorded very rapidly and many scans can be averaged in the time taken for a single scan of a dispersive spectrometer.

2. *Jacquinot advantage* – For the same resolution, the energy throughput in an interferometer can be higher than in a dispersive spectrometer, where

it is restricted by the slits. which provide ability to achieve the same signal-to-noise ratio as a dispersive instrument in a much shorter time.

3. *Connes advantage* – The wavenumber scale of an interferometer is derived from a HeNe (helium neon) laser, $\lambda = 632.8$ nm, that acts as an internal reference for each scan. The wavenumber of this laser is known very accurately and is very stable. As a result, the wavenumber calibration of interferometers is much more accurate and has much better long term stability than the calibration of dispersive instruments.

3.1.1 Optical Setup

Figure 3.1 illustrates the schematic of FTIR optical setup used for measurement of upconversion photoluminescence. A conventional fibre-coupled continuous wave (CW) semiconductor laser diode (NT55-373 Edmond Optics) with an emission centred at a wavelength of 975 nm and a nominal output power of 450 mW was used as the excitation light source. The collimated laser beam is reflected and focused on the sample that is placed on a sample holder in front of a FTIR system. Emissions from the sample is then collected by the objectives of the FTIR system and guided through the beam splitter. From the beam splitter beams propagate toward the mirrors and the reflected beams are reunited to produce a single beam. Two short pass filters with cutting wavelengths of 950nm and 900nm are used to prevent the excitation laser from reaching the detector that is a normal commercial silicon photodiode.

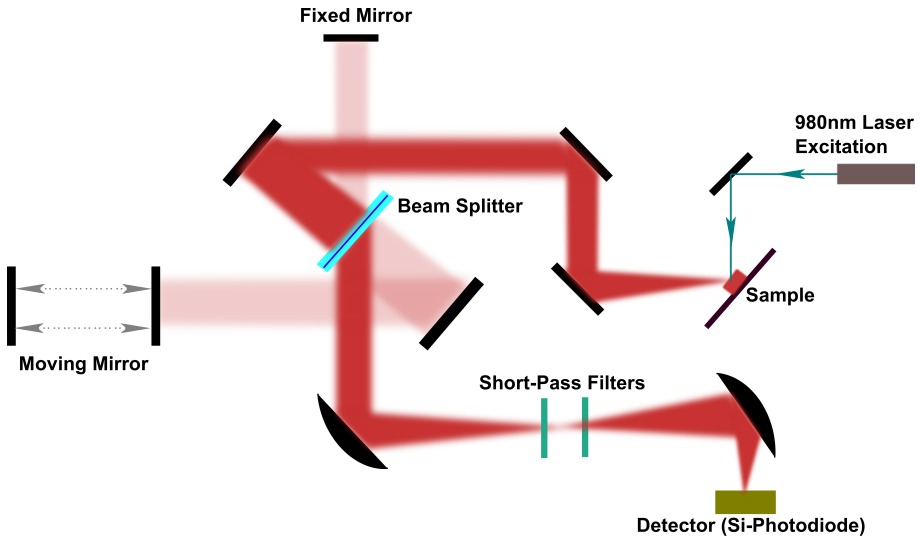

Figure 3.1: FTIR spectrometer optical setup used for accurate measurement of upconversion photoluminescence.

3.1.2 Results and Discussion

Upconversion photoluminescence of all Gd_2O_3 samples doped with Tm^{3+} and Er^{3+} is measured using the optical setup described in the previous section. Figure 3.2 illustrates the photoluminescence spectrum of Tm doped samples T1, T2, T3 and T6. Samples T1 and T2 are synthesised using 1 M urea solution, whereas samples T3 and T6 are synthesised using 2 M urea. Samples T1 and T3 are doped with 0.6 mmol of Yb^{3+} and 0.1 mmol of Tm^{3+}, whereas samples T2 and T6 are doped with 3 mmol Yb^{3+} and 0.25 mmol of Tm^{3+}. When excited with the 980 nm CW laser diode, all Tm^{3+} doped samples show pure near infrared to near infrared (NIR-to-NIR) upconversion emissions with a wide double peak in the range of 760 to 840 nm with the highest peaks located at around 810 nm, as seen in the figure. The lowest emission intensity belong to sample T1 that contains a low dopant concentration and synthesised using a

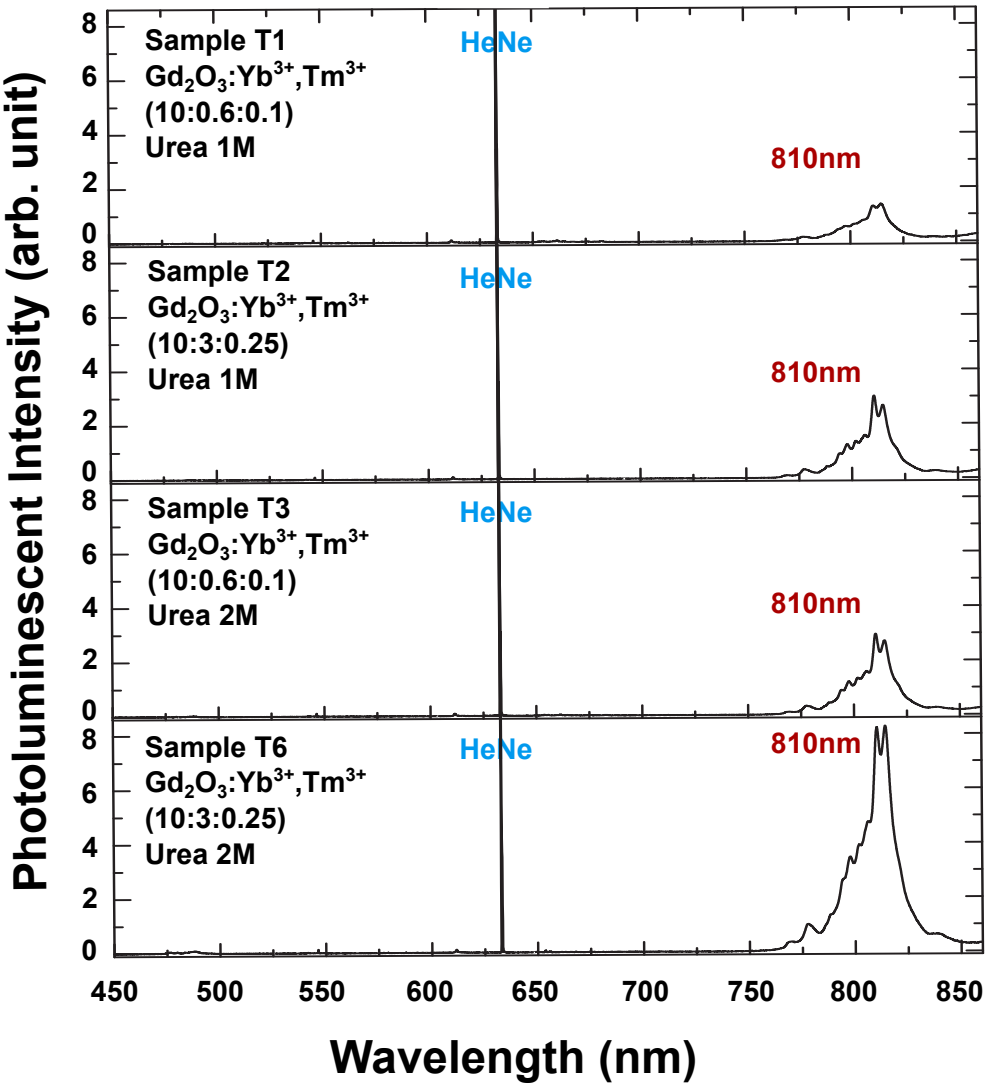

Figure 3.2: Upconversion photoluminescence from Tm doped samples T1, T2, T3 and T6, excited with a 980 nm CW laser diode. This diagram signifies the effect of changing urea and dopant concentrations on emission intensity. The peak emission of all samples is at 810 nm. HeNe laser of the spectroscope is marked in blue.

1 M urea. In contrast, the highest intensity is for sample T6 with a high dopant concentration and a 2 M urea. Sample T2 and T3 shows similar upconversion intensities, although sample T3 is doped with a lower concentration of dopants. These results shows that increasing the urea concentration during synthesis enhances the upconversion intensity of samples.

Figure 3.3 shows the upconversion photoluminescence of samples T3, T4, T5 and T6. All these samples are synthesised using a 2 M urea solution with different dopant molar ratios. All samples emit pure upconversion with a gradual increase of intensity from T3 to T6, which can be attributed to the increased dopant concentration. The intensities detected from samples T5 and T6 are similar. Both T5 and T6 are doped with 3 mmol Yb^{3+}, but have different concentrations of Tm^{3+}, which are 0.1 mmol for T5 and 0.25 mmol for T6. As seen in this figure, for Tm^{3+} doped Gd_2O_3 samples it is necessary to have 3 mmol Yb^{3+} to get an intense upconversion emission, and for this Yb^{3+} concentration, the emission intensity changes negligibly when Tm^{3+} dopant concentration changes from 0.1 to 0.25 mmol for T5 and T6, respectively, possibly due to self quenching of activator Tm^{3+} dopants by nonradiative relaxation.

For Er doped Gd_2O_3 samples, photoluminescence upconversion is demonstrated in Figure 3.4 and Figure 3.5. Similar to Tm doped samples the upconversion measurments are performed using a 980 nm excitation from a CW laser diode with 450 mW power. Figure 3.4 illustrates the effect of concetration of urea solution on the photoluminescence intenisty of Er^{3+} doped samples. Samples E1 and E3 are doped with 0.6 mmol of Yb^{3+} and 0.1 mmol of Er^{3+},

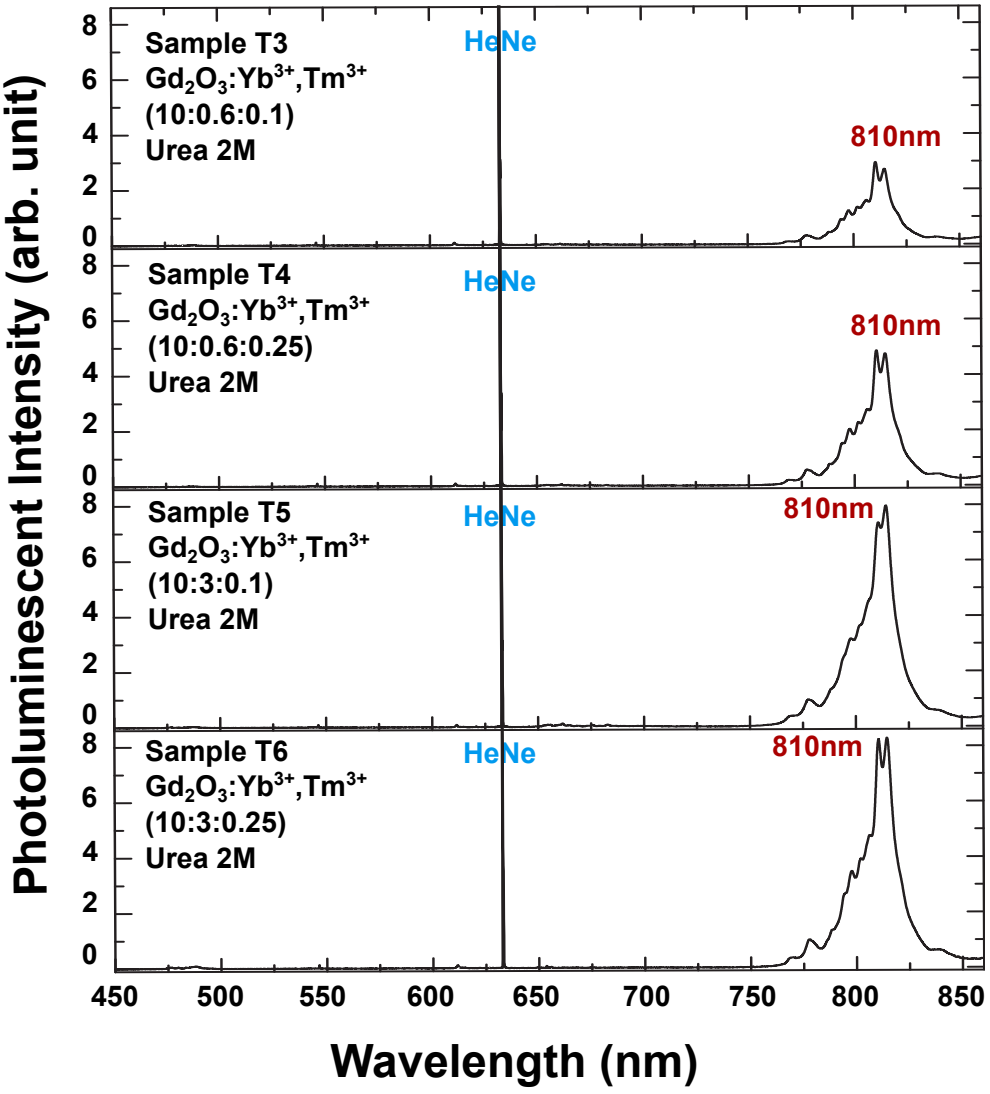

Figure 3.3: Effect of dopant cocentrations on upconversion photoluminescence of Tm^{3+} doped samples. Samples doped with 3 mmol Yb^{3+} have the most intense emission that is not changed significantly by changing the concentration of Tm^{3+} dopants. The peak emission of all samples is at 810 nm. HeNe laser of the spectroscope is marked in blue.

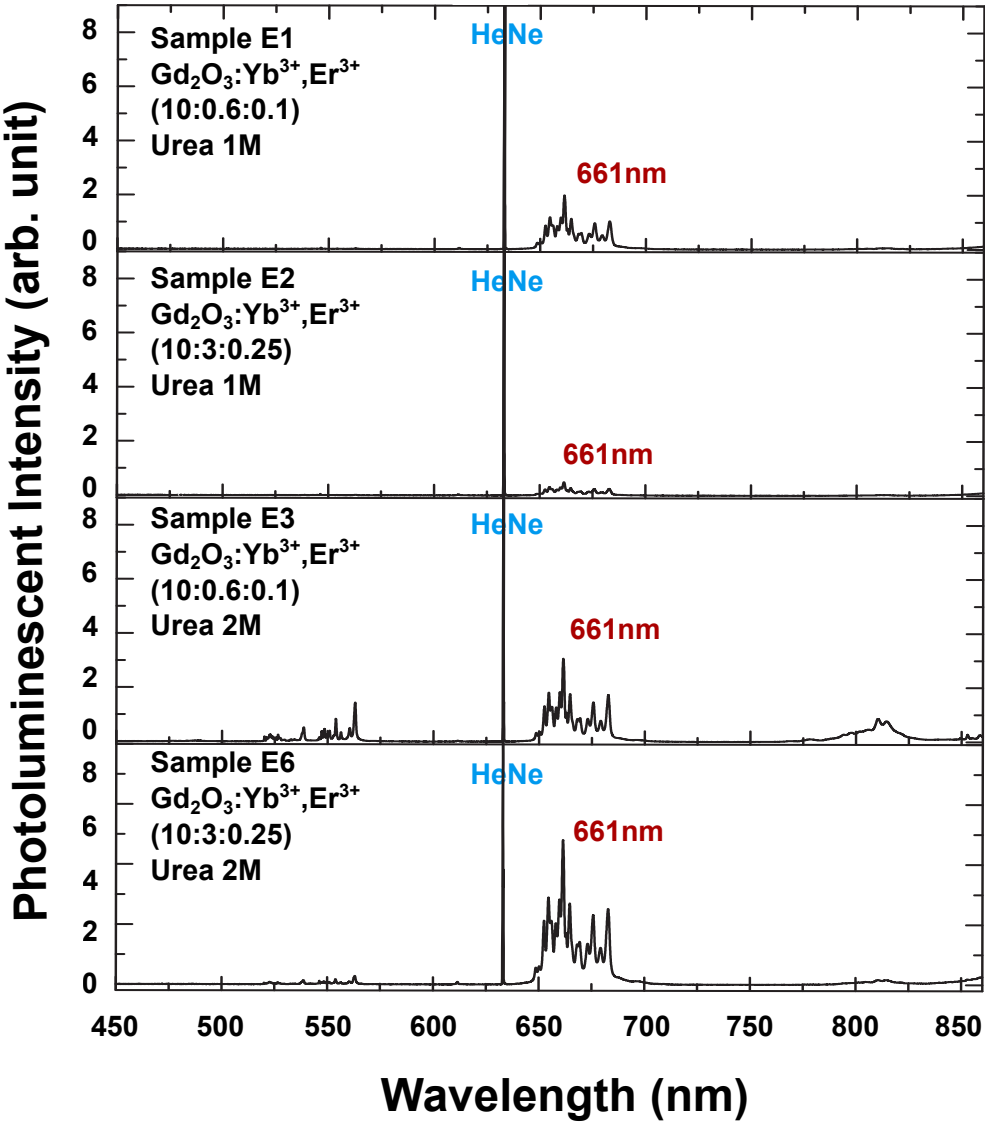

Figure 3.4: Effect of urea concentration on upconversion photoluminescence from Er^{3+} doped samples.

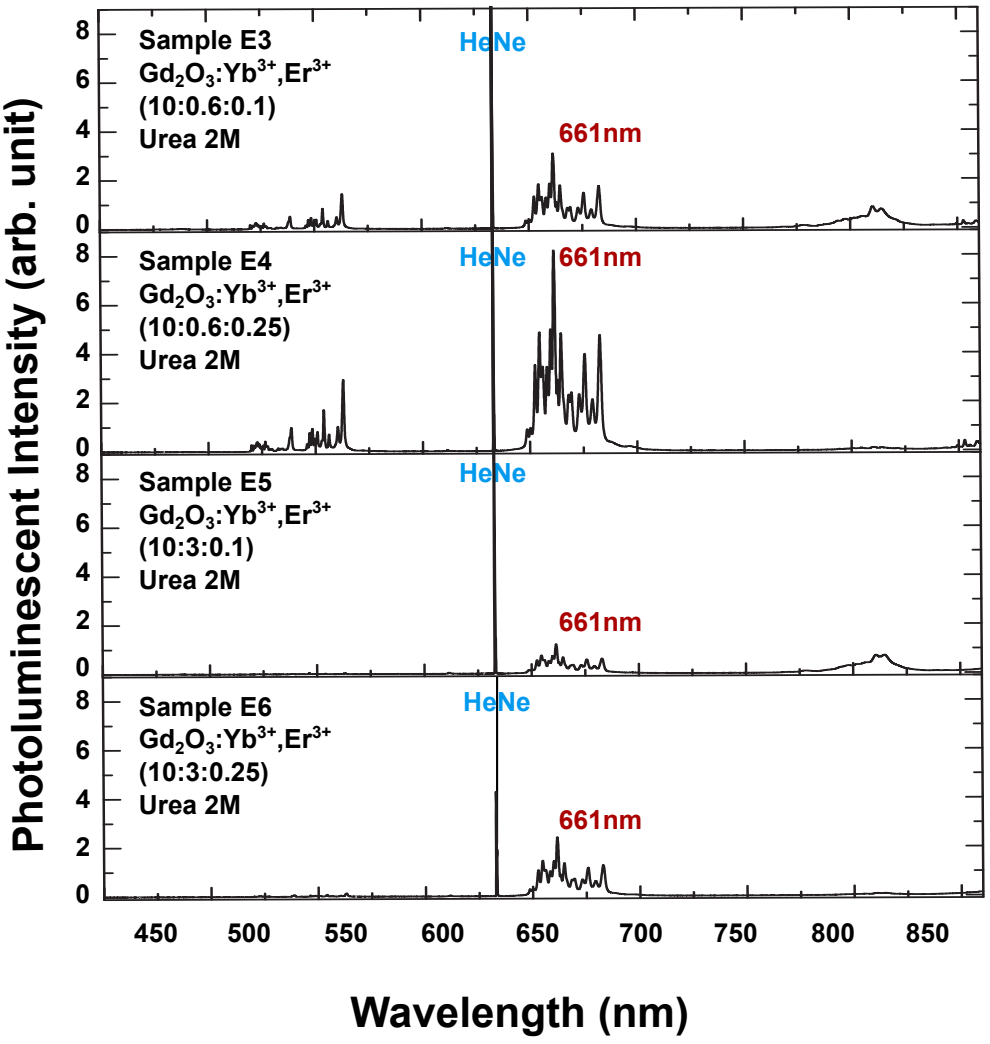

Figure 3.5: Effect of dopant concentration on upconversion emission from Er^{3+} doped samples. The most intense emission is detected from sample E4 with 0.6 mmol of Yb^{3+} and 0.25 mmol of Er^{3+}.

but E1 is synthesised using a 1 M urea solution, while a 2 M urea is used for synthesis of sample E3. Upconversion emission from sample E3 is strong and centred in the red region of spectrum at around 661 nm. Sample E3 shows a similar peak in the red region, but also emits in the green and near infrared regions the spectrum, as shown in the figure. Sample E6 and E2 have similar dopant concentrations, which are Yb^{3+} 3 mmol and Er^{3+} 0.25 mmol. Sample E6 is synthesised with a 2 M urea solution, while for sample E2 1'M urea is used. Comparing the photoluminescence of these samples shows that increasing the urea concentration from 1 M to 2 M enhances the intensity for the main emission peaks in the red region at around 661 nm. Note that similar to sample E3, sample E6 have some small peaks in green region and near infrared region, although these peaks have been suppressed in comparison to those of E3.

Figure 3.5 illustrates the effect of dopant concentration on upconversion emission of Gd_2O_3 doped with Yb^{3+} and Er^{3+}. Unlike Tm doped samples explained earlier, for the Er^{3+} doped samples the highest emission intensity is detected for samples synthesised using a 2 M urea solution. The most intense emission detected from sample E4 that is doped with 0.6 mmol of Yb^{3+} and 0.25 mmol of Er^{3+}. The second intense upconversion emission is observed for sample E3 that is doped with 0.6 mmol of Yb $^{3+}$ and 0.1 mmol of Er^{3+}. Samples E5 and E6 are doped with larger concentration of dopants Yb:Er of 3:0.1 and 3:0.25, respectively, but the upconversion emission of these samples are less intense than samples E3 and E4. The main emission from all samples is measured in the red region of the spectrum with the highest peak located at 661 nm. Samples E4 and E3 display emission peaks in the green region with the

highest peak at around 560 nm. In addition, small near infrared emissions are detected in samples E3 and E5 at around 810 nm.

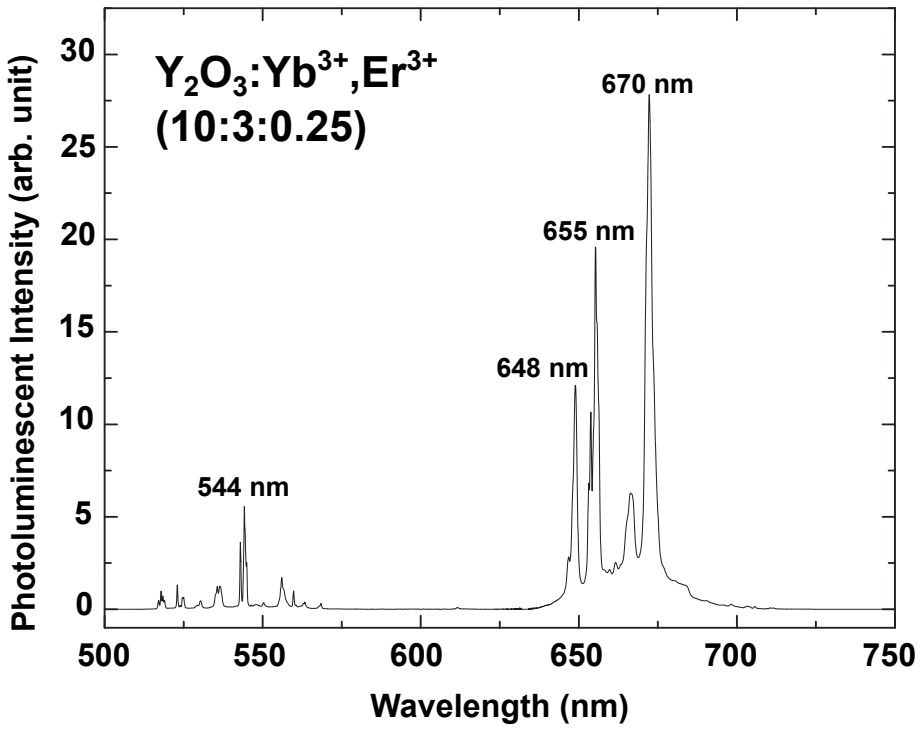

Figure 3.6: Upconversion photoluminescence of Y_2O_3:Yb^{3+}, Er^{3+} microparticles synthesized using rare-earth co-ordination precursors. Strong upconversion detected in the red and green regions of spectrum.

In addition to Gd_2O_3, we have investigated the upconversion emission from Y_2O_3:Yb^{3+}, Er^{3+} samples synthesized using organic solvothermal method using the FTIR setup. Figure 3.6 shows the emission spectrum of Y_2O_3:Yb^{3+}, Er^{3+} with molar ratios of 10:3:0.25. The upconversion emissions from these samples are strong with two range of peaks in the red and the green regions of spectrum. The highest peak is in the red region located at around 670 nm and

there are two other peaks in this region centred at 655 nm and 648 nm. The highest peak in the green region is located at 544 nm. I also tried other molar ratios for the organic Y_2O_3:Yb^{3+}, Er^{3+} samples but the most intense emission is detected from the molar ratio of 10:3:0.25. It is important to mention that I did not detect any upconversion emission from Y_2O_3:Yb^{3+}, Tm^{3+} synthesized using the organic solvothermal method.

3.1.3 Effects of Urea and Dopant Concentrations

As described earlier, several synthesis parameters affect the optical properties of resultant particles synthesised by UHP method, including host material, dopants concentration, urea concentration, reaction pH, reaction temperature and reaction time. In this work, the effects of urea and dopant concentrations on the morphological and especially the upconversion photoluminescence of the nanoparticles are investigated.

I have not detected any significant effect on the morphology of the particles by changing the urea and dopants concentrations. Although it has been reported that increasing urea concentration from 0.04 to 4 M decreases the particle size from 220 to 100 nm in case of synthesis of Y_2O_3 nanoparticles [150], but in this work, I have shown that for different amount of urea 1 and 2 M, the morphology of the particles does not change significantly. In contrast, by using a higher concentration of urea 2 M the photoluminescence intensity increases significantly, signifying the effect of urea concentration on the incorporation of dopants in the host Gd_2O_3 crystal lattice. I observed that the reaction and

ageing times affect the morphology and size of the particles more significantly. The reaction time for all our samples is kept at around 20 minutes. We observed that for a shorter reaction time of around 5 minutes no observable crystalline particle is formed and no upconversion photoluminescence is detected. By running the reaction for more than 1 hour, particles become massively large and form large aggregates and sediments in the reaction flask. We have not detected any upconversion photoluminescence from aged samples as well. Therefore, best results for upconversion emission was achieved for a urea concentration of 2 M which provides good nucleation and crystallinity in the samples over a controlled reaction time.

The other critical factor for upconversion emission is the dopants concentration. The sensitiser (Yb^{3+}) and activator (Tm^{3+} or Er^{3+}) concentrations are crucial factors for having an intense upconversion emission, since low concentration of dopants decreases the energy transfer efficiency and excess concentration of dopants leads to emission quenching effects by increasing the non-radiative relaxation between ions inside the host lattice. For ETU upconversion systems, other researchers suggest that the sensitiser concentration should be high ($\sim$ 20 mol %) and the activator content should be relatively low ($\sim$ 2 mol %) [9] unrelated to the type of activator or sensitiser ions.

In this work, I have tried different concentrations of both sensitiser and activator as described in Tables 2.2 and 2.3. Similar to urea, the dopants concentration does not play a crucial role in particles morphology and their size which could be justified by the fact that rare-earth materials and especailly Yb,

Tm and Er act in a similar way in the chemical reactions and therefore changing their relative concentrations should not have crucial effect on the morphology of the particles. On the other hand effect of the dopants concentration on upconversion photoluminescence is crucial and is related to the type of the dopants. In case of Gd_2O_3:Yb^{3+}, Tm^{3+} the highest luminescence intensity is detected for sample T5 doped with 3 mmol of Yb^{3+} and 0.1 mmol of Tm^{3+}, which is comparable to the suggested ratios in the literature and shows the crucial role that Yb^{3+} plays in energy transfer of this optical system. The luminescence intensity decreases when I tried higher or lower dopants concentrations because of non-radiatiove relaxation and non-efective energy transfer mechanisms, respectively.

Gd_2O_3:Yb^{3+}, Er^{3+} samples shows the highest upconversion intensity with 0.6 mmol Yb^{3+} and 0.25 mmol Er^{3+} (sample E4). The upconversion luminescence of the Er^{3+} doped samples, unlike the Tm^{3+} doped samples, decreases by increasing Yb^{3+} concentration, signifying the less critical role of Yb^{3+} in energy transfer of Er^{3+} doped samples in comparison to the Tm^{3+} samples. The energy transfer mechanisms of these samples will be described in Section 3.4.

3.2 Photoluminescence Measurement for Organic and Combustion Samples

Most commercial spectrophotometers [7] use monochromators in order to provide the spectrum of the emission coming from a sample under test. These

systems also use a monochromator for generation of different excitation wavelengths. A monochromator separates a narrow band of wavelengths $\Delta\lambda$ from a radiation source using constructive diffraction of the incoming light from a fine grating (typically 4000 to 20000 lines per cm). Two slits (entrance and exit) are used as well to achieve narrower band of wavelengths, but inevitably suppress the amount of light reaching the detector. The typical light source of a spectrophotometer is a tungsten filament lamp with an emission in the range of 350 – 2500 nm.

As discussed earlier, there are several issues related to the use of a conventional spectrophotometer for upconversion photoluminescence measurement. First, for upconversion a laser excitation is required and it is not possible to get an emission using the normal tungsten lamp used for monochromators. To overcome this issue, we have coupled a laser to a conventional spectrophotometer setup and bypassed the main light source and the first monochromator, which are not that easy to perform on most spectrophotometers. Second, due to the sharp emission peaks form the rare-earth based upconversion, it is necessary to have a very narrow wavelength resolution, which implies a smaller slit and finer grating and consequently an extremely low intensity light reaching the detector if a monochromator is used. Finally, as the signal is very low intensity, the measurements accuracy and repeatability is not good when a monochromator is used.

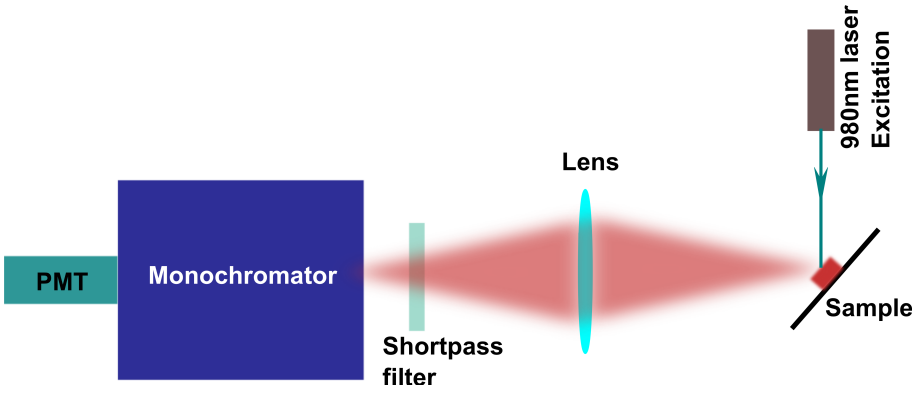

Figure 3.7: Optical setup, using a monochromator and a photomultiplier tube (PMT) to measure upconversion photoluminescence of samples synthesised by organic and combustion methods.

3.2.1 Optical Setup

Due to the limitations and issues of conventional spectrophotometers, discussed previously, I have set up a hand made spectrophotometer suitable for measurement of upconversion photoluminescence. Figure 3.7 depicts a schematic diagram of the optical setup used for the measurement of upconversion photoluminescence of samples derived mainly from organic solvothermal method and combustion method. A collimated 980 nm CW laser diode is used as the excitation source that is focused on the sample located on a sample holder. The upconversion emission guided through lenses and other objectives including two sets of shortpass filters with cutting edges of 900 nm and 950 nm in order to eliminate the excitation and prevent saturation of the detector. The filtered emission signal enters a monochromator that is connected to a photomultiplier tube (PMT) detector. The recorded data from the PMT to a computer for the analysis.

3.2.2 Results and Discussion

The optical setup described in Section 3.2.1 is used to measure low intensity upconversion emission from samples synthesized based on organic slovothermal method with surfactant and combustion method. The upconversion emissions of Y_2O_3:Yb^{3+}, Er^{3+} samples syhtnesized with different surfactants including PVA, PAA and PEG are displayed in Figure 3.8. The molar ratios of the host, dopants and also the surfactants used in the synthesis are kept unchanged in all samples. Interestingly the upconversion emission spectrums of the PVA and PEG samples are similar, while that of the PAA samples shows emission peaks in the green region of the spectrum. The highest peaks for all samples are located in the red region at around 670 nm.

It is important to mention that due to low intensity of emission from these samples it is hard to compare the emission intensities quantitatively. But the emission intensity of the organic solvothermal samples decreases dramatically when surfactants are used in synthesis. This can be due to the critical morphological changes when the surfactants are used, which affect the crystal and lattice formation and decrease the energy transfer in samples.

Another important issue is that by using a monochromator in the output decreases the sensitivity of the measurements. Comparison of the spectra derived using FTIR (Figure 3.6) setup and this setup (Figure 3.8) demonstrates the difference in accuracy of the two setups.

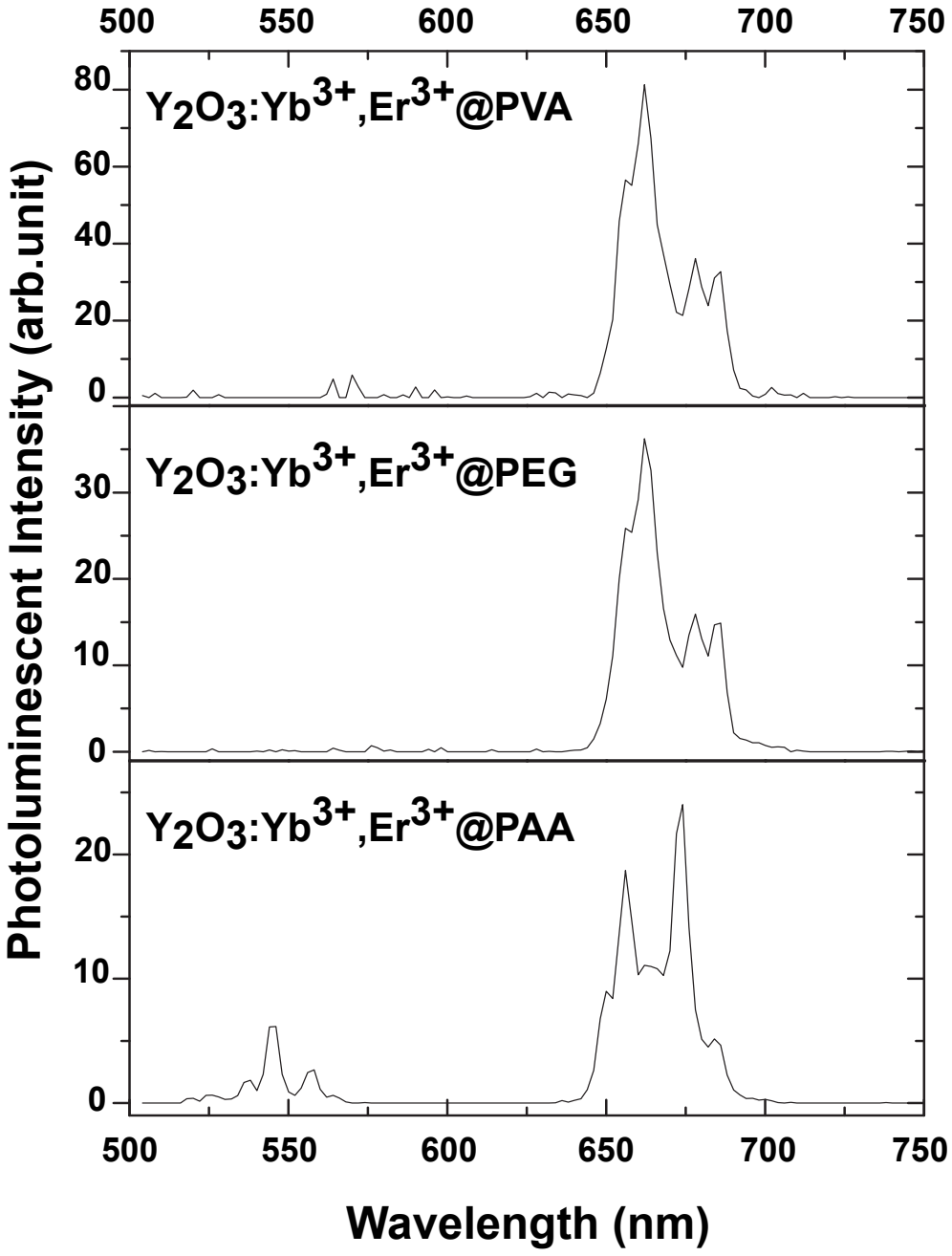

Figure 3.8: Upconversion photoluminescence of samples synthesized using rare-earth co-ordination with different surfactants.

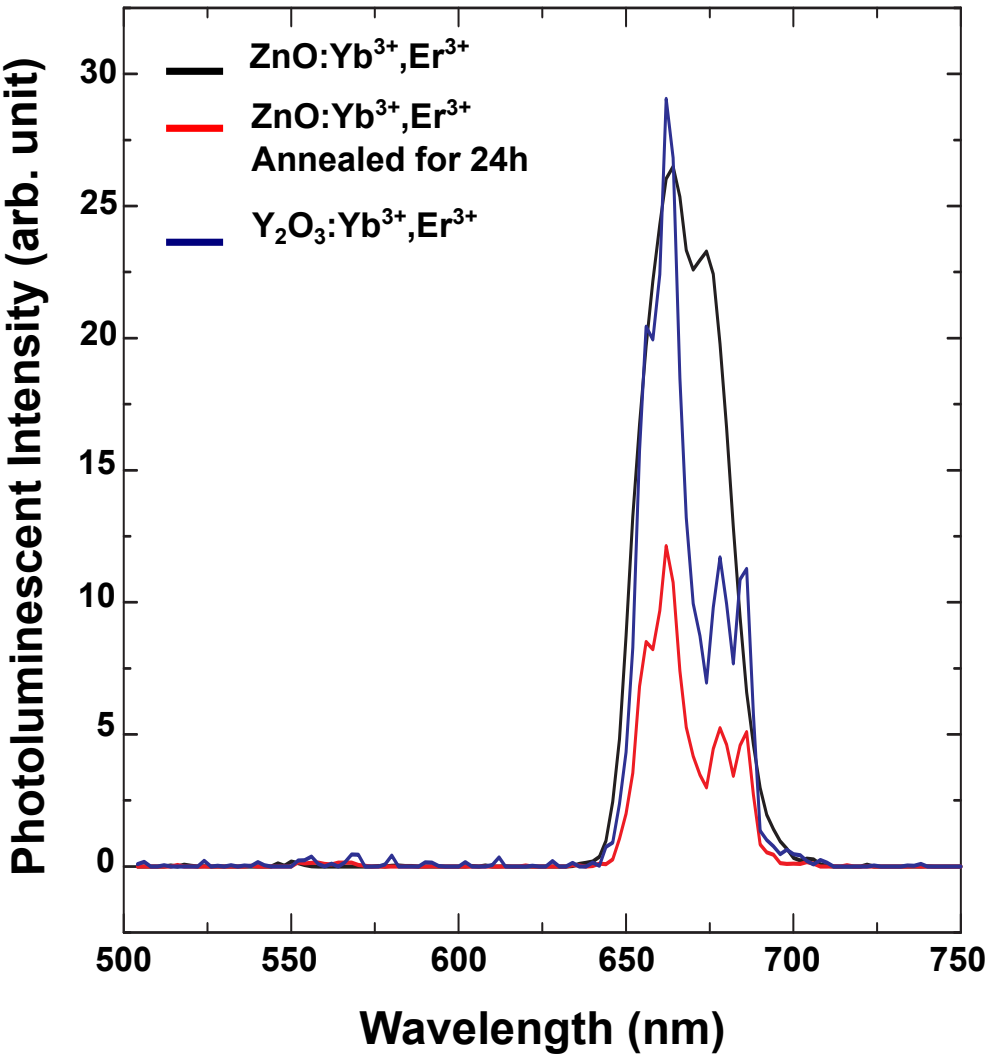

Figure 3.9: Upconversion photoluminescence of ZnO and Y_2O_3 samples synthesized using the combustion method. Photoluminescence of annealed ZnO samples decreases the emission intensity but sharpens the emission peaks.

Figure 3.9 illustrates the upconversion photoluminescence measurement results for Y_2O_3:Yb^{3+},Er^{3+} and ZnO:Yb^{3+},Er^{3+} samples synthesized using combustion method and measured with the setup described in Figure 3.7. Both Y_2O_3 and ZnO samples have emissions in the red region with the highest peaks located at around 660 nm with comparable intensities. We have tried a 24-hour annealing for the ZnO samples, as reported to increase the intensity of the upconversion emission [159], but as shown in Figure 3.8, annealing of ZnO:Yb^{3+},Er^{3+} samples for 24 hours at 900°C decreases the emission intensity by at least three orders of magnitude.

3.3 Time Resolved Photoluminescence Measurements

Mainly, there are three different methods for time resolved photoluminescence measurements:

1. *Decay of Emission to Obtain Lifetime.* A pulsed laser is used as the excitation source and the emission decay is monitored.

2. *Real-time Monitoring of Forster Resonance Energy Transfer (FRET).* A pulsed laser is used to excite an energy donor molecule and the emission of an energy acceptor molecule is studied as a function of time.

3. *Transient Spectroscopy.* A pulsed laser is used to obtain absorption, emission or Raman spectra of a sample.

After a pulsed excitation, the photoluminescence intensity I often decays through an exponential fluorescence decay involving a decay rate k, as given by

$$I = I_0 e^{-kt} = I_0 e^{-t/\tau}, \tag{3.1}$$

where I_0 is the initial photoluminescence intensity at $t = 0$ when the excitation pulse is turned off and τ the characteristic lifetime of the emission. This behaviour is referred to as a single exponential decay. The decay rate k represents both a radiative decay rate k_r and a nonradiative decay rate k_{nr}. Considering the radiative and nonradiative lifetimes, τ_r and τ_{nr}, respectively, we have

$$k = k_r + k_{nr} = \frac{1}{\tau_r} + \frac{1}{\tau_{nr}} = \frac{1}{\tau}. \tag{3.2}$$

We have performed upconversion photoluminescence decay measurements on Gd_2O_3:Yb^{3+},Er^{3+} (sample E4) and Gd_2O_3:Yb^{3+},Tm^{3+} (sample T5), which are selected in view of their intense upconversion emissions among all samples synthesised using UHP method. The optical set up used for this measurement described in the following.

3.3.1 Optical Setup

Figure 3.10 and 3.11presents the optical setup used for upconversion decay measurements. A 980 nm pulsed laser with a 5 ns pulse width and 3 mJ energy is used as the excitation source. A 500 nm longpass (LP) filter is placed between the laser and the sample in order to eliminate the second hormonic of the laser source. An optical powermeter is used next to the LP filter to monitor the reflectance and scattering of the laser and its harmonics. Samples are sandwiched

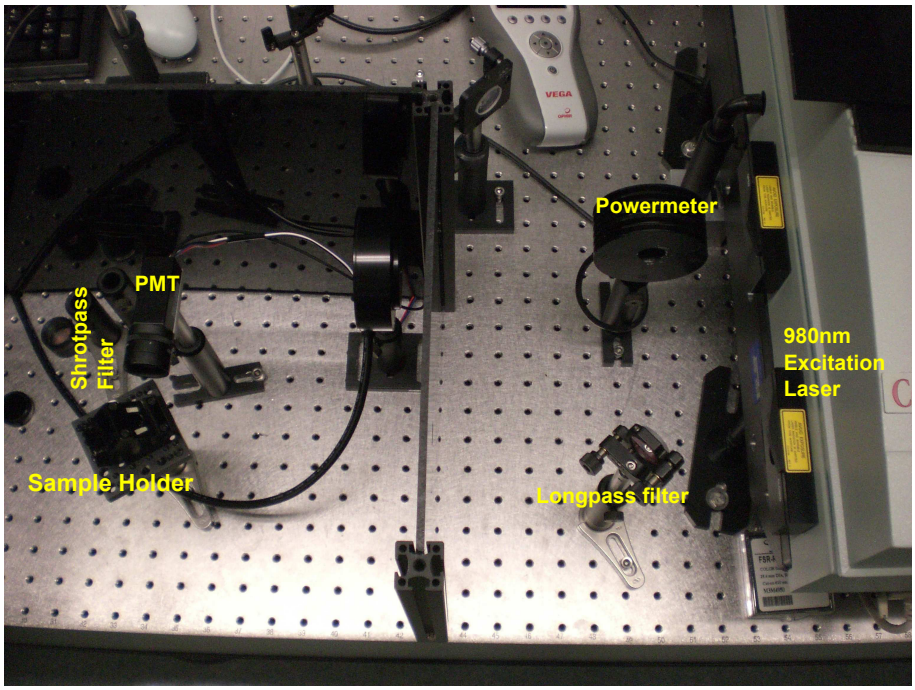

Figure 3.10: Optical setup for measurement of upconversion photoluminescence decay.

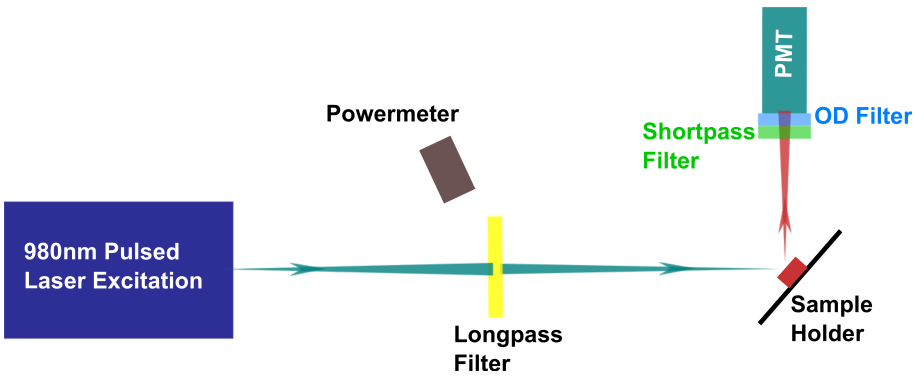

Figure 3.11: Schematic fiagram of Optical setup for measurement of upconversion photoluminescence decay. Short pass and OD filters mounted in front of PMT.

between two peaces of thin quartz and placed on a sample holder. The emission from the sample is guided to a fast PMT detector through two shortpass filters with cutting wavelengths of 950 and 900 nm in order to remove the laser excitation beam. Dark glass walls are used to make a dark room for the sample compartment to prevent the ambient light from reaching the detector. The detector is connected to a computer to record data.

3.3.2 Results and Discussion

Figure 3.12 depicts the decay measurement results for the sample E4, i.e., Gd_2O_3:Yb^{3+},Er^{3+} with molar ratio of 10:0.6:0.25, using the optical setup described in 3.3.1. The top part of Figure 3.12 demonstrates the decay results of sample E4 without any filter and with a 0.3 OD and 1 OD neutral density filters. The idea behind using these neutral density filters is to ruled out the effect of high intensity excitation beam on the decay results for the emission from the sample. The decay curves show a rapid decay with a lifetime of about 10 μs and a then a gradual decay lasting for about 35 μs. The lower part of Figure 3.12 illustrates the logarithmic scale of the decay measurement results for sample E4 with green straight lines fitted to curve. We have calculated the decay time constant τ from the slope of the fitted lines using:

$$\tau = \frac{dt}{dI} \log_1 0e, \tag{3.3}$$

where dI is the amount of decay in the intensity in the time interval dt. The decay graph without an OD filter shows a double exponential behaviour with a decay time constant τ_1=5 and τ_2=7.79 μs for the first and second fittings,

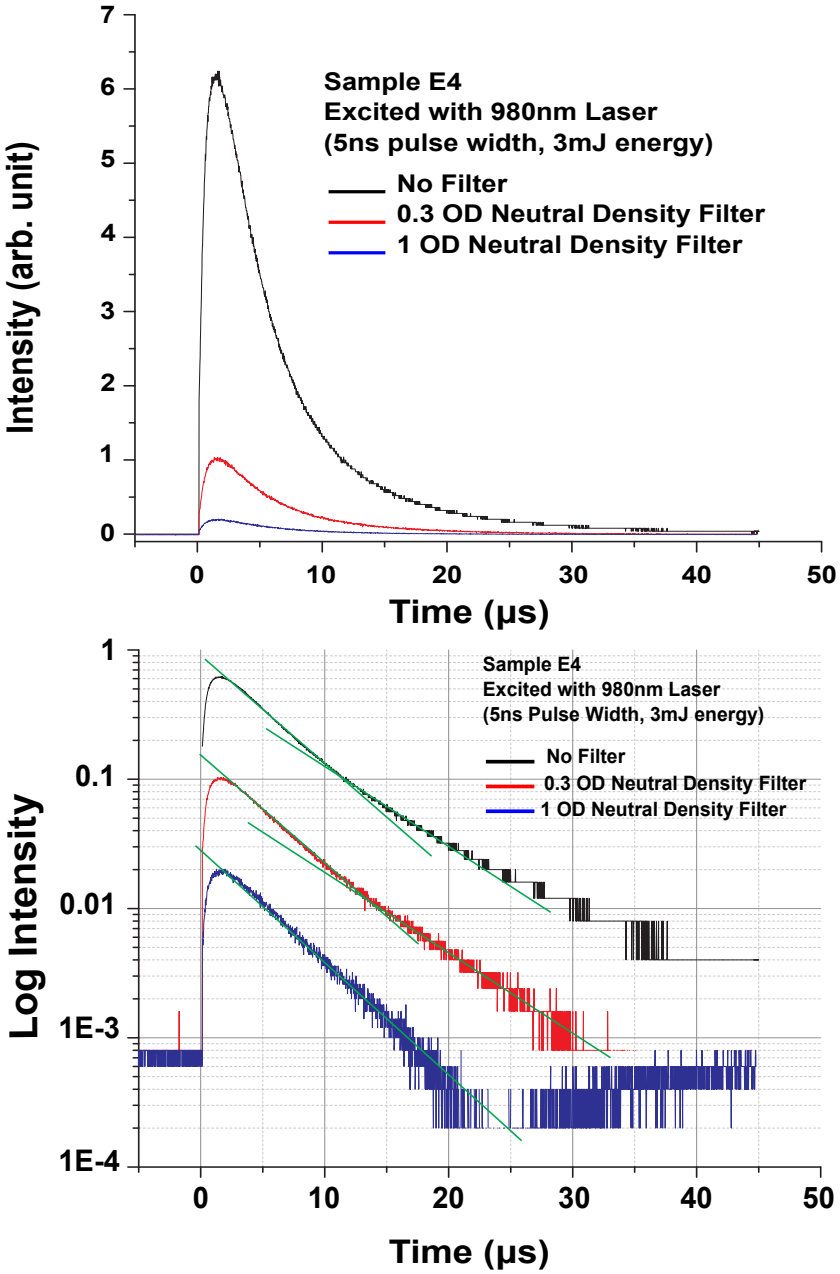

Figure 3.12: Decay measurement of upconversion emission from sample E4 in linear (top) and log (bottom) scale, showing a double exponential decay (with close time constants) without using OD filters. The emission becomes a single exponential decay when a 1 OD filter is used.

respectively. Calculated decay time constants with a 0.3 OD filter is τ_1=6.15 and τ_2=8.68 μs. Finally, the decay time constant calculated for the only fitting line of 10 OD filter is τ=7.16 μs. Therefore, although decay graphs without filter and with a 0.3 OD filter show double exponential behaviour, since the time constants of the two fittings of the graphs are very close, the double exponential behaviour can be attributed to the intense photon flux coming from the excitation source, and the decay behaviour of E4 sample should be considered as a single exponential with a time constant of τ=7.16 μs as found for measurement with a 1 OD filter.

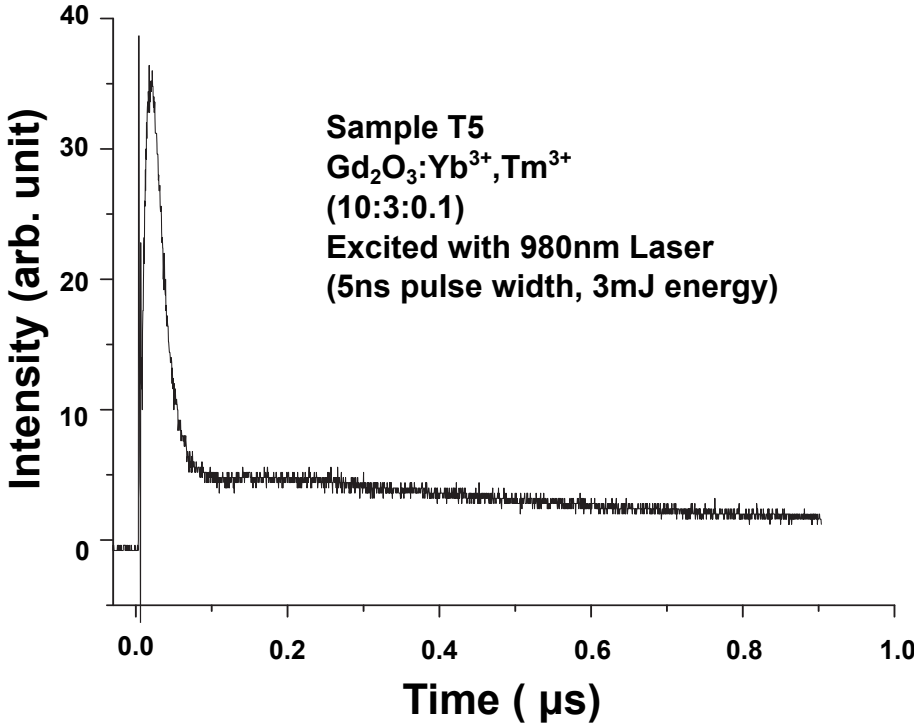

Figure 3.13: Upconversion luminescence decay measurements of sample T5, showing a fast decay followed by a long tail.

The decay measurements are also performed on sample T5, i.e., Gd_2O_3:Yb^{3+}, Tm^{3+} with molar ratios of 10:3:0.1, as illustrated in Figure 3.13. The decay measurement shows a rapid decay with a lifetime of about 75 ns followed by a long tail of gradual decay with a lifetime of 1.6 μs. The calculated decay time constants for sample T5 using Equation 3.3 is τ_1=1 ns and τ_2=130 ns for the rapid and slow decays, respectively. These results signify the distinctly different photoluminescence decay characteristics of sample T5 showing a clear double exponential decay in comparison to sample E4.

Differences between energy levels and energy transfer in Tm^{3+} doped and Er^{3+} doped Gd_2O_3:Yb^{3+} is the main underlying reason for the observed differences in the decay measurement of these two samples. As it will be discuss in Section 3.4, the main emission from sample E4 (Gd_2O_3:Yb^{3+}, Er^{3+}) is due to the radiative relaxation of $^4F_{9/2} \rightarrow {}^4I_{15/2}$. Although, we have detected some peaks in the green region of the spectrum as well, the main emission is from this energy transfer in the red area (661 nm), consequently leading to a longer lifetime and single exponentional for the photoluminescence decay (as seen in Figure 3.12). For sample T5 (Gd_2O_3:Yb^{3+}, Tm^{3+}), however, the emission is only coming form the radiative energy relaxation of $^3H_4 \rightarrow {}^3H_6$ (810 nm), but Tm^{3+} is famous as a blue emitter and it has a ladder like energy levels to reach to $^1D_2$ energy and emit in blue. In our system the structural formation of the ions force most of the electrons to reach to $^3H_4$ and emit at 810 nm which produce the fast decay peak, but there exist some electrons populated at other energy levels that reach higher energy levels of Tm^{3+} such as $^1D_2$ and $^1G_4$ and the relaxation of these electrons produce a very long but low intensity tail as

observed in Figure 3.13.

3.4 Energy Levels and Energy Transfer Methods

Understanding of how energy transfer happens in the synthesized samples is one of the most important steps in optical and material characterization. Upconversion photoluminescence and decay measurements described in previous sections provide essential data necessary for decoding complicated energy levels and energy transfer mechanisms. In this section I provide a brief review of quantum mechanic basics of energy levels and energy transfer in rare-earth materials, followed by comprehensive discussion of proposed energy transfer mechanisms for Gd_2O_3:Yb^{3+}, Er^{3+} and Gd_2O_3:Yb^{3+}, Tm^{3+} Systems.

3.4.1 Quantum Mechanic Basics of Energy Level Structures in RE materials

During the last century, discoveries in the field of quantum mechanics have revolutionised our understanding of the structure of matter. Here is a brief overview of fundamentals of electronic structure of materials especially Lanthanides, based on details provided by Jean-Claude G. Bünzli in [160], Guokui Liu in [161] and Michel J. F. Digonnet in [162]. Basically, the Schrödinger equation defines the interaction of electrons and nucleus in an atom as

$$H\Psi_n = E_n\Psi_n \tag{3.4}$$

where H is the time-dependent Hamiltonian operator describing the sum of kinetic and potential energies in the system. Ψ_n is the wavefunction and related to the movement of the particles and its square, $(\Psi_n)^2$, gives the probability that the particle will be found in a position given by the coordinates; the set of all probabilities for a given Ψ_n is called an orbital. E_n is the quantified energy associated with a specific wavefunction and is independent of the coordinates. In case of hydrogen the Hamiltonian simply consist of Coulombo's attraction between electron and nucleus and the kinetic energy named as H_0. Each wavefunction, or orbialts, calculated from the equation 3.4 defined by four quantum numbers, showing the two motions of the electrons including angular momentum $\vec{l}$ and the spin $\vec{s}$. The principal quantum number n is an integer and represent radial expansion of the orbital. The angular quantum number l varies from 0 to (n-1) and depicts the shape of the orbital, letters: *s*, *p*, *d*, *f*, *g*,... for l= 0, 1, 2, 3, 4,... respectively. on the other hand m_l is the projection of the $\vec{l}$ into z axis and its values different from -l and +l. Finally, m_s is the projection of $\vec{s}$ and have values of $\pm\frac{1}{2}$.

The energy levels of heavy atoms such as RE^{3+} free ions are determined by Hamiltonian operator given as,

$$H = H_0 + H_C + H_{SO} \tag{3.5}$$

Where H_0 is the central field approximation, H_C is the electrostatic interaction and H_{SO} is the spin orbit coupling. The central field approximation is the main contributor, in which each electron is assumed to move independently in a spherically symmetric potential formed by the nucleus and the average potential

of all the other electrons. Both H_C and H_{SO} are small compare to central field approximation and treated as perturbation. Using the central field approximation, the ${}_4F^N$ electron configuration has a single specific energy unrelated to the orbital and spin angular momentum. This single energy level is lifted by the H_C and H_{SO}, which splits the configuration into multiple energy levels. In this aspect for all $4f$ orbitals, each f electron contributes an orbital quantum number of 3 and spin of $\frac{1}{2}$. The LS coupling, or Russell-Saunders coupling, defines the energy states of rare-earth materials. L and S are added vectorially to form the total angular momentum J and the energy states are labelled as ${}^{2S+1}L_J$. Here $2S+1$, with S as the overall spin quantum number, represents the spin multiplicity. When S=0 , 2S+1=1, it represent a singlet state, while for S=1, 2S+1=3, represents a triple state. L represents the total angular momentum. The overall total angular momentum J is then obtained by coupling both L and S together such as J= (L-S), (L-S)+1, ..., (L+S).

Figure 3.14 shows an example of energy level splitting diagram of rare-earth materials. In this model the degeneracy of the electron configuration, defined by central field approximation, first lifted by the electrostatic interactions to produce the first splitting. This followed by the weaker spin-orbit coupling splits those levels into sub-levels. This coupling model is more accurate for light elements and for heavy elements such as lanthanides the free ion Hamiltonian is simplified into terms of effective operators based on the type of rare-earth. When a rare-earth is doped into a host and chemically bonds the electrostatic interaction change the spherical free ion model, but as the ${}_4F^N$ electrons are shielded this interactions are week and is considered as a perturbation H_{CF} to

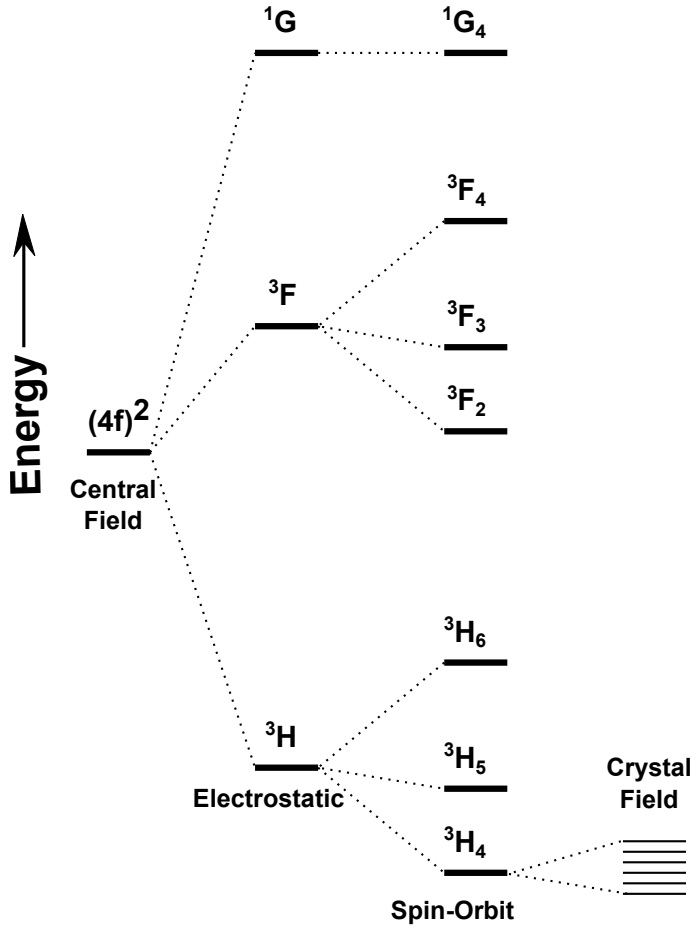

Figure 3.14: Energy diagram showing splittings resulting from electron-electron and electron-host interactions [162]

the previously described free ion model. H_{CF} lifts the angular momentum J, splitting each $^{2S+1}L_J$ into number of levels. For example, 2J+1 states created if the RE^{3+} ion has even number of f electrons. The manifolds split from J levels are responsible for the spectroscopic properties of lanthanides including absorption and emission.

3.4.2 Energy Transfer Mechanisms for Gd_2O_3:Yb^{3+}, Er^{3+} and Gd_2O_3:Yb^{3+}, Tm^{3+} Systems.

As mentioned before, lanthanide ions are the best choice for making upconversion materials due to their ladder like energy levels (Figure 1.11). We have also discussed the possible theoretical energy transfer mechanisms in systems which use Yb^{3+} as a sensitiser and Tm^{3+} or Er^{3+} as an activator, as shown in Section 1.6.3 (Figure 1.12). The optical characterisation not only provides the emission wavelength and spectrum for different samples but also leads to an understanding of the energy transfer mechanism of the observed photoluminescence emission.

Figure 3.15 depicts the photoluminescence of Gd_2O_3:Yb^{3+}, Er^{3+} samples (E1 to E6) in one graph from which it is possible to claim that in all Er^{3+} doped samples the main emission peaks are centred at 661 nm, which can be attributed to the $^4F_{9/2} \rightarrow {}^4I_{15/2}$ energy transfer mechanism. There are also two other peaks in some of the Er^{3+} doped samples: the first is in the green region at 562 nm and the second in the NIR region centred at 811 nm (detected in samples E3 and E5). These two peaks are correlated to the energy transfer of $^4S_{3/2} \rightarrow {}^4I_{15/2}$ and $^4I_{9/2} \rightarrow {}^4I_{15/2}$, respectively.

The mechanism leading to upconversion in Er^{3+} doped samples can be summarized as follows. The Yb^{3+} absorbs 975 nm photon in the $^2F_{7/2} \rightarrow {}^2F_{5/2}$ transition. Electrons are then easily transferred from the Yb^{3+} $^2F_{5/2}$ level to the Er^{3+} $^4I_{11/2}$ level because of the alignment of the respective energies, as schematically illustrated in Figure 3.16. The Er^{3+} also absorbs photons from

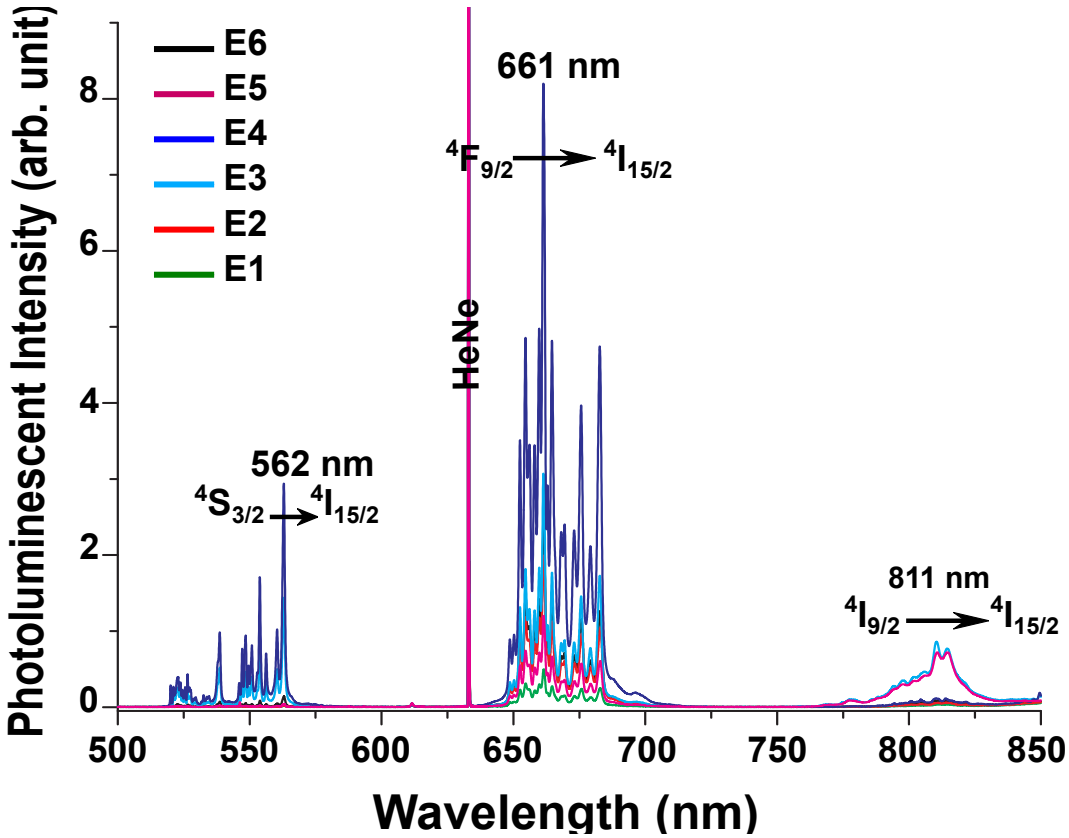

Figure 3.15: Upconversion photoluminescence of Gd_2O_3:Yb^{3+}, Er^{3+} samples with different synthesis condition, showing different peaks and corresponding to the proposed energy transfer mechanisms.

975 nm laser in the $^4I_{15/2}$→ $^4I_{11/2}$ energy transfer. Therefore, the Er^{3+} $^4I_{11/2}$ populated by absorbing photons directly by Er^{3+} or by transfer from Yb^{3+} to Er^{3+}. From there, another 975 nm photon can be absorbed or transferred from Yb^{3+}, taking the electron to Er^{3+} $^4F_{7/2}$. The electron then makes its way to $^4F_{9/2}$ thorough a non-radiative relaxation. From this energy level, a $^4F_{9/2}$→ $^4I_{15/2}$ transition gives rise to a 661 nm unconverted visible red emission.

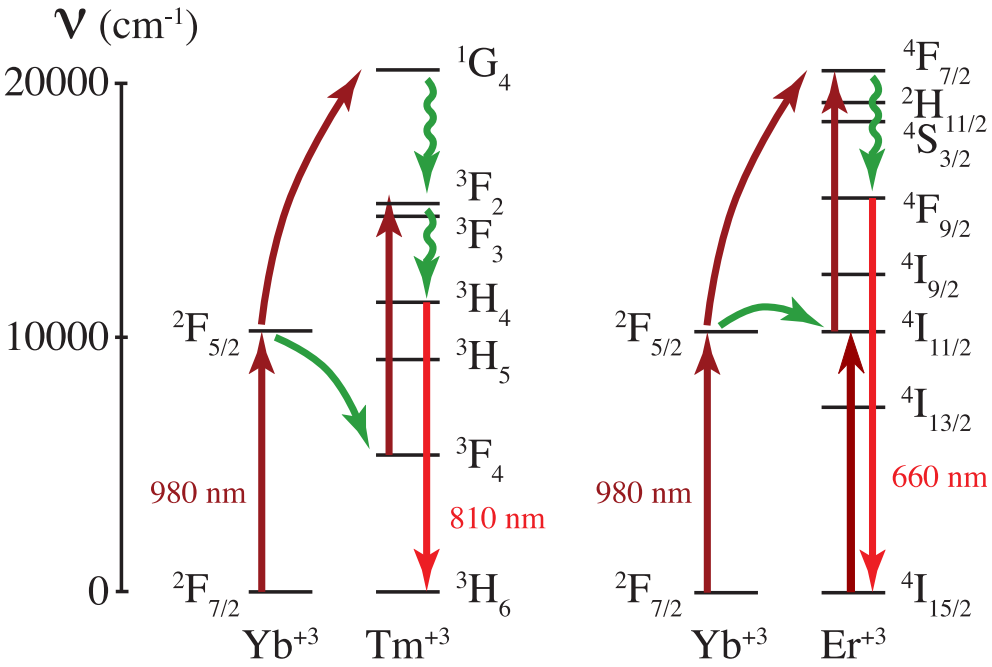

Figure 3.16: Left: Stark level scheme showing energy transfer between Yb^{3+} and Tm^{3+} ions for an 810 nm emission. Right: Similar level scheme showing energy transfer between Yb^{3+} and Er^{3+} ions for a 660 nm emission. The y-axis is wavenumber, and the position of the Stark levels are taken from Kaminskii's definitive work [15].

The energy transfer for a green emission (562nm) from Er^{3+} doped sample also starts from absorbing a 975 nm photons from the laser excitation by Yb^{3+} and Er^{3+} as described above, which ends in populating Er^{3+} $^4F_{7/2}$. From there, absorption or transfer of another photon takes the electrons to Er^{3+} $^2H_{11/2}$ from which electrons are relaxed by a non-radiative relaxation to reach Er^{3+} $^4S_{3/2}$. Finally, the electron transition $^4S_{3/2} \rightarrow {}^4I_{15/2}$ produces the observed green emission. In the case of Er^{3+} doped samples (E3 and E5) the low intensity NIR upconversion emission is centred at 810 nm. This rarely possible energy

transfer happens by series of non-radiative relaxations between Er^{3+} $^4F_{7/2}$ and Er^{3+} $^4I_{9/2}$ from which electrons radiatively relax to emit the NIR emission. As it is more likely for electrons to relax through higher energy levels such as $^4F_{9/2}$, the NIR emission from Er^{3+} doped samples is not statisitcally favoured.

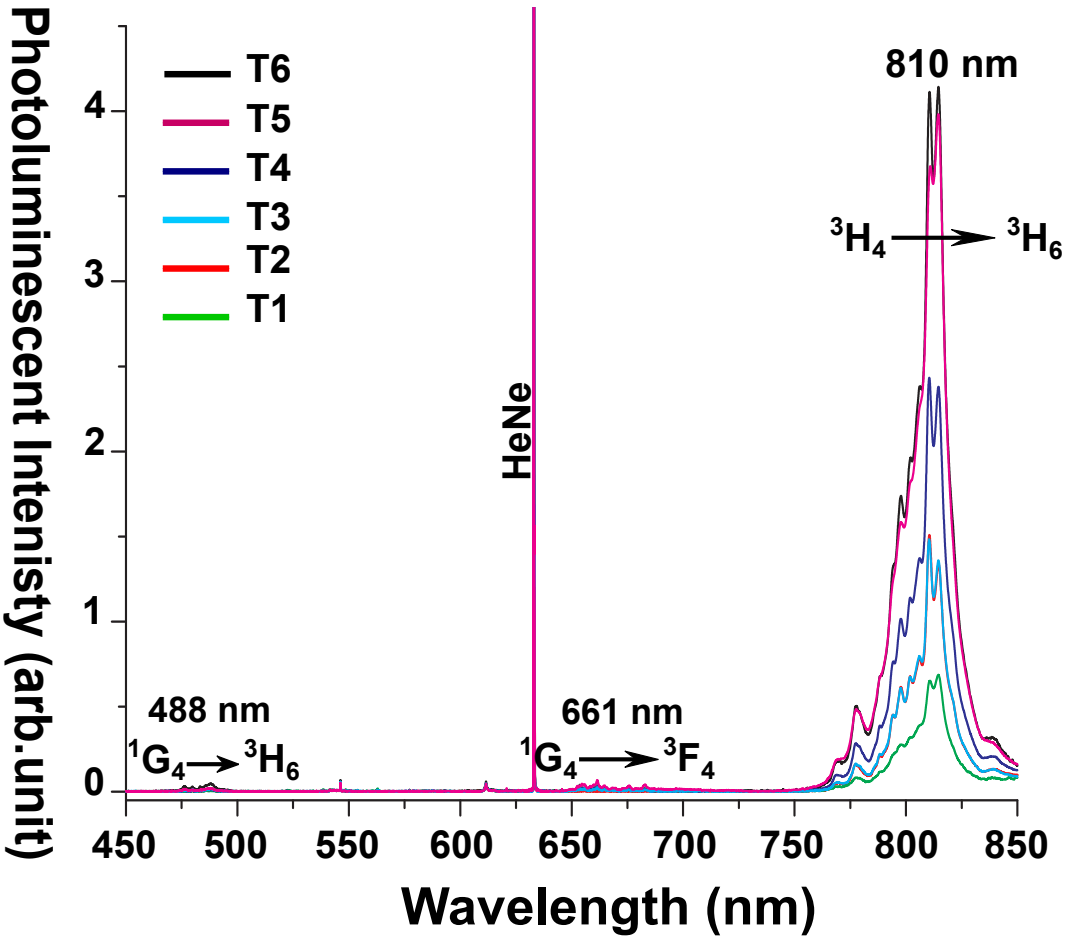

Figure 3.17: Upconversion photoluminescence of Gd_2O_3:Yb^{3+}, Tm^{3+} samples with different synthesis conditions, showing different peaks and corresponding proposed energy transfers.

Figure 3.17 depicts the photoluminescence of Gd_2O_3:Yb^{3+}, Tm^{3+} for sam-

ples T1 to T6. These samples show almost pure NIR-to-NIR upconversion emission centred at 810 nm corresponding to the $^3H_4 \rightarrow {}^3H_6$ transition. The traces of two other emissions that appear in some samples, namely the 661 and 488 nm emissions can be attributed to the $^1G_4 \rightarrow {}^3F_4$ and $^1G_4 \rightarrow {}^3H_6$ transitions, respectively.

Figure 3.16 demonstrates the suggested Stark manifold levels for upconversion mechanisms observed for the Yb^{3+} and Tm^{3+} ions adjacent to each other and highlights the importance of the Yb^{3+} sensitiser in facilitating the upconversion emission. The $^2F_{7/2} \rightarrow {}^2F_{5/2}$ transition in Yb^{3+} resonates with the photon energy of the 975 nm pump laser excitation. From the Yb^{3+} $^2F_{5/2}$ level, an electron can transfer to the Tm^{3+} $^3F_4$ level by losing some energy, whereupon another 975 nm photon can excite it into the $^3F_2$ level. From there, the electron makes its way to the $^3H_4$ where it undergoes the $^3H_4 \rightarrow {}^3H_6$ transition giving rise to the 810 nm upconverted near infrared emission. Another alternative path sees electrons from Yb^{3+} $^2F_{5/2}$ level excited to the Tm^{3+} $^1G_4$ level through the so-called diagonal transition. This is followed by the non-radiative relaxation from Tm^{3+} $^1G_4$ to Tm^{3+} $^3H_4$ and the radiative relaxation $^3H_4 \rightarrow {}^3H_6$ that leads to emission of the 810 nm photon.

3.5 Upconversion Imaging by Multiphoton Microscopy

Upconversion is a multiphoton phenomenon and therefore multiphoton microscopes are used for *in vitro* applications of upconversion nanoparticles. In multiphoton microscopy, absorption of series of photons excites a fluorophore such as upconversion nanoparticle to an excited state followed by upconversion emission which is used to obtain an image. Most of the practical applications of multiphoton microscopes for upconversion nanoparticles use a two-photon absorption mechanism since a three-photon absorption requires an excitation laser with an extremely high peak intensity [7].

Since a normal two-photon microscope requires simultaneous absorption of two laser photons from a pulsed source, it is necessary to use high power laser as the probability for this absorption is proportional to the square of light intensity. Typically, a Ti:Sapphire laser that produces a very short ($\sim$ 100 fs) pulses centered around 800 nm with a very large peak power (50 kW) is needed. Please note that theoretically upconversion excitation can occur even without simultaneous excitation and therefore high laser femtosecond lasers are not necessary. To prove the applicability of the Gd_2O_3 upconversion nanoparticles synthesised in this work for *in vitro* bioimaging, we have performed microscopy imaging using a Leica TCS SPII confocal and multiphoton microscope. The next two sections will describe the optical setups and the results of the experiments.

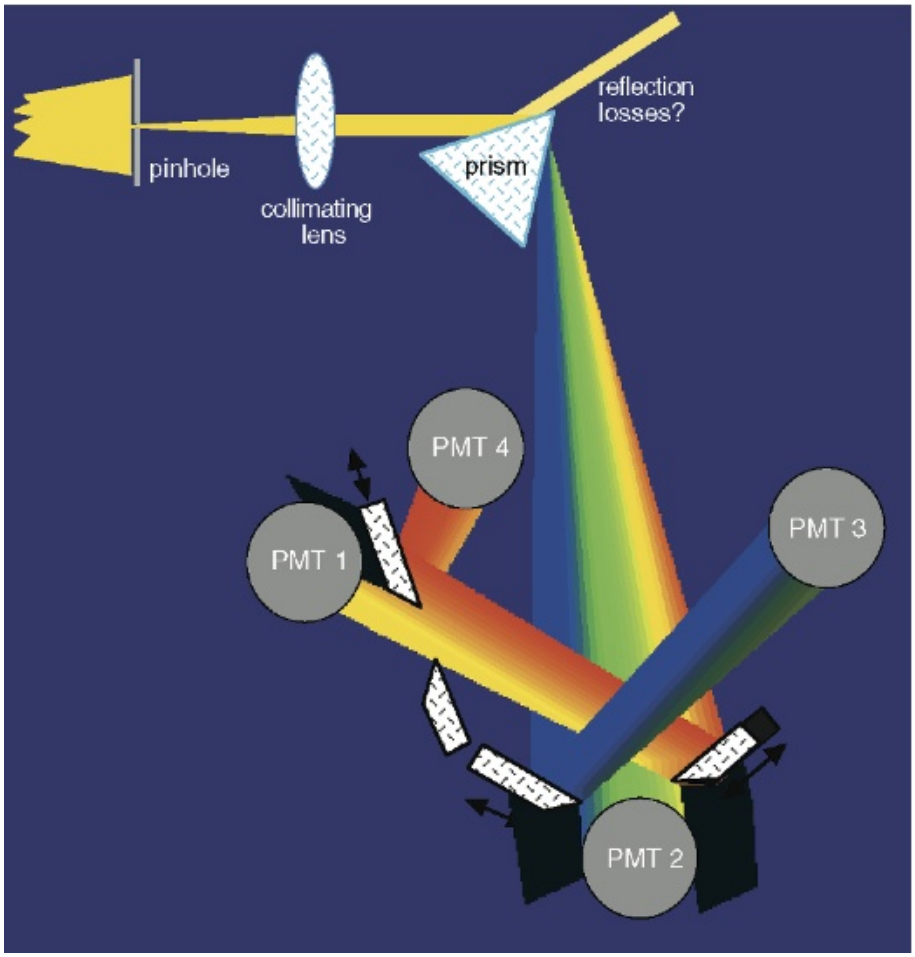

Figure 3.18: Schematic of Leica TCS SPII spectrophotometer detection system using a prism, 2 sliders and 4 PMTs to detect the region of interest of the spectrum [16].

3.5.1 Optical Setup

The Leica TCS SPII confocal and multiphoton microscope is used for characterization of upconversion nanparticles. In addition to UV and visible laser sources, the system has a tunable IR source. The excitation from the laser is passing through a series of objectives and mirrors, which produce a collimated

beam that reaches the sample through the microscope objective lens. Emission from the sample goes exactly the same way as the excitation and reaches a beam splitter that sends the emission signal trough filters and in case of the confocal microscopy through a pin hole. The filters and beam splitter are used to control the amount light heading toward the detector. The specific detector system of Leica system is shown in Figure 3.18. The emission light passes thorough a prism that stretch the light to separate the spectrum that can be redirected onto the opening window of different PMTs. There are four PMTs available in this system with slits that narrow down or widen the spectrum of the incoming light, as shown in the figure. The advantage of using such a system is possibility to adjust the imaging band according to the dye used, the possibility of multi-spectral imaging using all four different PMTs and the possibility of performing emission spectra via wavelength scan [16].

3.5.2 Results and Discussion

To demonstrate the potential of using the synthesised upconversion nanoparticles for *in vitro* bioimaging applications, we have used the Leica multiphoton microscope. Sample E4, with the most intense upconversion emission is selected for this experiment. Unfortunately the highest sensitivity of the PMT detectors of the microscope was at 795 nm and therefore even this unique set up is not suitable for Tm^{3+} doped samples. Upconversion nanoparticles from sample E4 are dissolved in DI water and stirred to get a homogeneous milky mixture. One drop of the solution is sandwiched between two pieces of microscope film for the experiment.

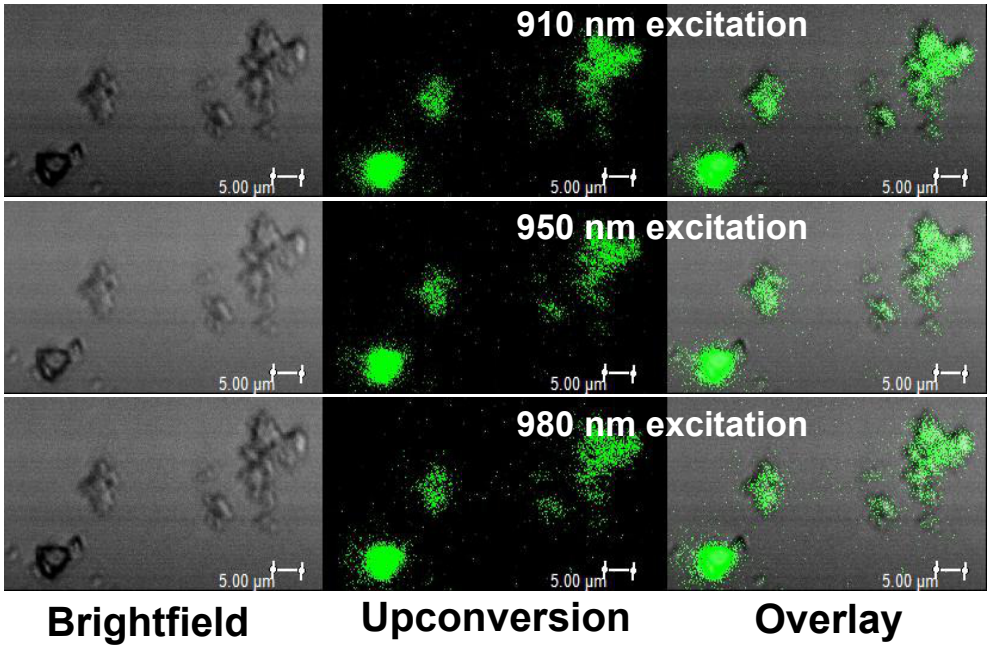

Figure 3.19: Brightfield, upconversion luminescence and the overlap image of clusters of nanoparticles from sample E4 under a two photon micrsocope. Different excitation wavelength has been tried and images are produced with all different excitations.

The excitation light source used in this experiment was a tunable NIR laser and we have tried different wavelength excitation from 850 to 1000 nm. Figure 3.19 illustrates the photomicrographs of the same sample exposed to different excitation wavelength of 910 (top), 950 (middle) and 980 nm (bottom). The micrograph from left to right are bright field microscope image of the nanoparticles, upconversion luminescence detected from the same sample using the corresponding excitation in the dark, and the overlay image of these pictures. The middle column of pictures shows a strong upconversion emission

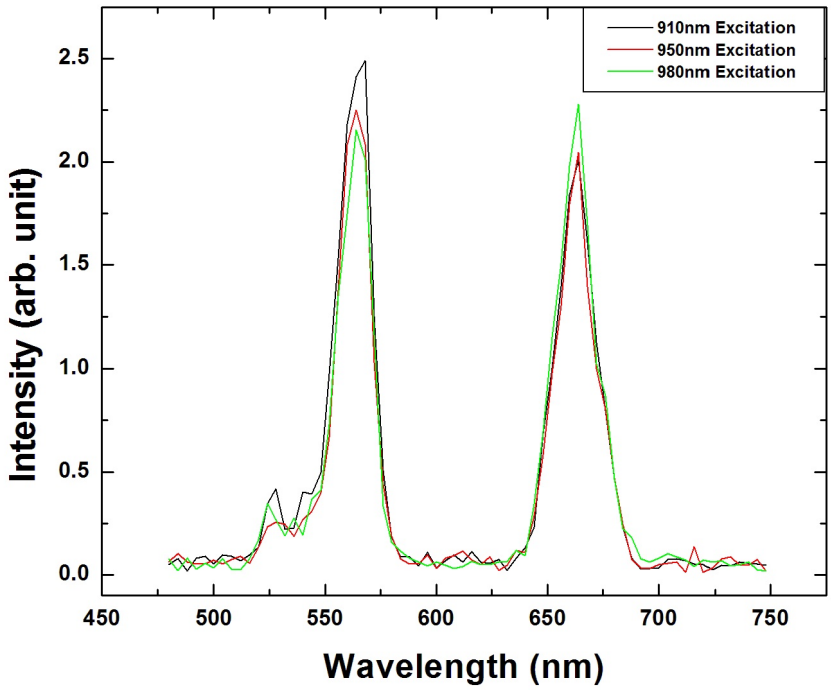

Figure 3.20: The intensity versus λ from Sample E4 (Gd_2O_3:Yb^{3+}, Er^{3+}) with different excitation wavelength, derived from microscopy imaging, showing the corresponding peaks in the red and green regions of spectrum.

from the clusters of particles for all excitation wavelengths used. The overlap pictures signify that the observed emissions accurately correlate to the location of the nanoparticles under the microscope. The spot size for the emitted signal is defined by the size of nanoparticle aggregates on the sample and for our detector is around 1μ m. This signifies the potential for high spatial resolution provided by these nanoparticles. We did not detect upconversion emission with excitation wavelengths smaller than 900 nm and larger than 1000 nm, but the

intensity of emission remain unchanged for the accuracy of our detector for the range of 910 – 980 nm, indicating the possibility of using these upconversion nanoparticles with 910 nm excitation, a preferred wavelength for bioimaging as water absorption coefficient is minimal at 910 nm in comparison to that for 980 nm [163].

Figure 3.20 depicts the photoluminescence intensity from sample E4 (Gd_2O_3:Yb^{3+}, Er^{3+}) measured by multiphoton microscope. Three different excitation wavelengths are examined for this sample, including 910, 950 and 980 nm. All wavelengths produce photoluminescence intensity spectrum with two peaks located at green (570 nm) and red (661 nm) regions of spectrum, demonstrating the efficiency of these nanoparticles for stable upconversion for a range of excitations.

3.6 Challenges and Opportunities in Optical Characterization of NIR-to-NIR Upconversion Nanoparticles

As described in this chapter, optical characterization of upconversion nanoparticles is performed using different methods and approaches so as to provide a comprehensive understanding of the optical properties of the synthesised nanoparticles. One of the most important challenges for optical characterization of upconversion nanoparticles, especially for the biologically important NIR-to-NIR conversion, is the lack of commercially available optical setup for precise and

quantifiable experiments. Due to this problem, performing NIR-to-NIR characterization a commercial optical setup needs to be radically modified or a new setup needs to be assembled. The reason for this problem is rooted in that almost all optical systems are built for Stoke's shift conversion or down conversion such as fluorescence. As an example, the most convenient way to do photoluminescence experiments is to use a spectrophotometer, such as Horiba's FluoroLog, but these devices usually use a tungsten light source with a monochromator to provide excitation beam in the required spectrum and for upconversion these light sources do not have the required intensity. This issue can be addressed by accommodation of a NIR fibre-coupled laser.

Second issue for the characterization of NIR-to-NIR upconversion samples is related to the confocal or multiphoton microscopes. Most typical confocal microscopes are not equipped with a NIR laser sources and their filter sets need to be changed for upconversion microscopic imaging use. Using multiphoton microscopes is a more convenient replacement as they have a tunable NIR laser by default. Though, the problem with multiphoton microscopes is their detectors and filters. For instance, the PMTs of Leica multiphoton that we used in this work has the maximum edge of sensitivity at 780 nm, and consequently, not suitable for microscopy imaging of Tm^{3+} doped particles with 810 nm emission while we manage to use the system sucessfully for Er^{3+} doped samples with an emission centred at 661 nm. It is important to note that since a compatible PMT for this type of microscope is still not available commercially by the manufacturer, the only possible way to do microcopy on these sample is setting up a hand made multiphoton microscope with the desired characteristics.

The above-mentioned problems limit the experimental methods that can be used for optical charaterization of NIR-to-NIR upconverison nanoparticles, but novel method such as using FTIR spectroscope for this purpose as demonstrated here can be a significant opportunity for future systems providing a high resolution full spectrum measurement even at low emission intensities.

3.7 Conclusion

Optical characterization is one of the most important steps in understanding optical, electronic and material properties of upconversion nanoparticles. Therefore, I tried different methods and approaches in this work to provide a comprehensive understanding of optical behaviour of synthesized nanoparticles.

Upconversion photoluminescence of Gd_2O_3:Yb^{3+}, Tm^{3+} and Gd_2O_3:Yb^{3+}, Er^{3+}, synthesized by UHP method, performed using novel FTIR setup reported in this chapter. Strong NIR to NIR upconversion detected from Gd_2O_3:Yb^{3+}, Tm^{3+} centred at 810 nm. This kind of pure NIR to NIR upconversion to the best of our knowledge has not been reported before for this type of upconversion nanoparticles. Same optical set up used for Gd_2O_3:Yb^{3+}, Er^{3+} which shows upconversion emission centred in red spectral region (661 nm). By applying upconversion photoluminescence measurements for samples synthesized using different dopants and urea concentration, this work also provide a better understanding of optimized synthesis recipe and energy transfer mechanisms

in this type of nanoparticles. Unrelated to the type of dopants used in these materials keeping urea concentration at 2 M provides good nucleation and crystallinity in samples leading for more intense upconversion emission. The effect of dopants concentration is different for different kind of lanthanide used as activator ion. The energy transfer and upconversion emission of Gd_2O_3:Yb^{3+}, Tm^{3+} are more Yb^{3+} dependent compare with samples doped with Er^{3+} as activator. Therefore the most intense emission from Tm^{3+} doped samples are detected from samples doped with 3 mmol of Yb^{3+} and only 0.1 mmol of Tm^{3+} (sample T5), while in Er^{3+} doped samples most intense emission detected from sample doped with only 0.6 mmol of Yb^{3+} and 0.25 mmol of Er^{3+}. Although it is suggested that for ETU upconversion systems the sensitiser concentration should be high ($\sim$ 20 mol %) and the activator content should be relatively low ($\sim$ 2 mol %) [9] unrelated to the type of activator or sensitiser ions, in this work I found out that, at least for samples with Gd_2O_3 as host, to get the most intense upconversion emission the sensitiser, in this case Yb^{3+}, concentration should be adjusted depending on what element used as activator.

Upconversion photoluminescence also measured for samples synthesized through other methods tried in this work. For Y_2O_3:Yb^{3+}, Er^{3+} samples synthesized using novel organic solvothermal method FTIR setup applied and intense upconversion detected from these samples. While for samples synthesized with organic solvothermal method by employing surfactants and also from combustion synthesis method, different optical setup applied using monochromator and PMT. These measurements not only provide crucial information about the optical properties of the synthesized samples but also provide an opportunity to

compare two different photoluminescence methods described in this chapter. In conclusion FTIR is a faster and easier to apply method, with much better resolution and possibility of getting whole spectrum data compare to the other method.

Decay measurements also performed for Gd_2O_3:Yb^{3+}, Tm^{3+} and Gd_2O_3:Yb^{3+}, Er^{3+} using the optical setup described in this chapter. There is a fundamental difference between decay results of Gd_2O_3:Yb^{3+} doped with Tm^{3+} and Er^{3+}, related to the different energy transfer mechanism of these two systems. The Er^{3+} doped samples exhibited a single exponential decay behaviour, while Tm^{3+} doped samples had a double exponential behaviour consist of a fast decay related to radiative relaxation from Tm^{3+} $^3H_4$ resulting in 810 nm upconversion emission, while some of the absorbed electrons populated at other energy levels of Tm^{3+} such as $^1D_2$ and $^1G_4$ relaxed in a non-radiative way to produce a long tail decay. It is important to mention here that to the best of out knowledge no prior work exists on upconversion photoluminescence decay of nanophosphors based on Gd_2O_3 doped with Yb^{3+}, Tm^{3+} or Yb^{3+}, Er^{3+}.

Another optical experiment that I performed in this work and described in this chapter was testing Gd_2O_3:Yb^{3+}, Er^{3+} nanoparticles with a commercial two photon microscope. This specific experiment shows the applicability of these type of nanoparticles synthesized in this work for *in vitro* applications. As the microscope equipped with a tunable laser I also tried different excitation wavelengths and it was proved that the intensity of emission remained unchanged for the range of 910-980 nm within the experimental error, which indicates the pos-

sibility of using these upconversion particles for 910 nm excitation, a preferred wavelength for bioimaging as water absorption coefficient is lower at 910 nm in comparison to that for 980 nm.

Chapter 4

Magnetic Characterization of Gd_2O_3 Upconversion Nanoparticles

A motivation for using Gd_2O_3 as host for optically-active upconversion nanoparticles is the possibility for using its magnetic properties in bimodal bioimaging. Gd complexes have proven to be a powerful alternative contrast agents for MRI [164, 165, 30], with advantage of providing a rise to positive contrast (bright signal) on T_1-weighted images because of their paramagnetic properties. This is in contrast to the superparamagnetic nanoparticles that only enhance the negative signal in MRI images, which is difficult to be distinguished in a weak MRI signal. In order to characterise the magnetic properties of the synthesised Gd_2O_3:Yb^{3+}, Tm^{3+} and Gd_2O_3:Yb^{3+}, Er^{3+} upconversion nanoparticles we used Superconducting Quantum Interference Device (SQUID) as one of the

most sensitive magnetometers and Magnetic Force Microscopy (MFM) as one of the most novel methods reported.

All SQUID and zero-field-cooled/field-cooled (ZFC/FC) measurements are performed by MPMS-XL Quantum Design magnetometer located in The Royal Institution of Great Britain and their technician helped me for these measurements. The MFM and AFM measurement performed by myself using a Veeco Dimension 3100 Atomic force microscopy located in London Centre for Nanotechnology (LCN). The following sections will describe basics of SQUID and MFM measurement and results of the magnetic characterisation of nanoparticles.

4.1 SQUID Measurements

Superconducting quantum interference devices (SQUID) is a very sensitive magnetometer, designed to detect very small magnetic fields. SQUID provides advantages such as high sensitivity ($\approx 10 - 100$ fT $\text{Hz}^{-\frac{1}{2}}$), wide bandwidth (from DC to 10 kHz), broad dynamic range (> 80 dB), its quantitative nature and reasonable costs [166]. The great sensitivity of SQUID magnetometers is associated to the properties of superconductive materials and Josephson junctions.

Superconductive materials conduct current with zero resistivity when cooled down to temperatures below a critical temperature T_c. The maximum current that a superconductive material can conduct with zero resistance is the

critical current I_c. A superconductive ring will have a quantized magnetic flux that is integer products of the quantum magnetic flux $\phi_0 = h/2e \cong 2.067833758(46) \times 10^{-15}$ Wb, where h is Planck's constant and e the elementary charge and weber (Wb) the SI unit of magnetic flux. A Josephson junction is formed by two superconductive material separated by a thin insulator layer or a weak link.

A SQUID measurement system is a superconducting loop containing two Josephson junctions, which provide a weakly connected superconducting loops. Thus, a change in the magnetic flux applied to the loop ϕ_A will cause the current to move in opposite way in order to oppose this change and ignite a phase difference in the junction. Most novel SQUID systems use a pick-up coil to collect data, in order to avoid exposing the bare SQUID to the magnetic field of interest.

The schematic of a typical SQUID system is presented in Figure 4.1. The SQUIDs are located inside a small magnetic shield (for example superconducting niobium). The superconducting pick-up coils are located at the bottom of the Dewar, the electronic devices are at room temperature and the magnetic objects are beneath the instrument. The samples is placed inside a gelatine capsule and kept in the SQUID part of the system and placed inside the liquid helium. A resistor attached to the SQUID holder is used to heat the sample during the experiment.

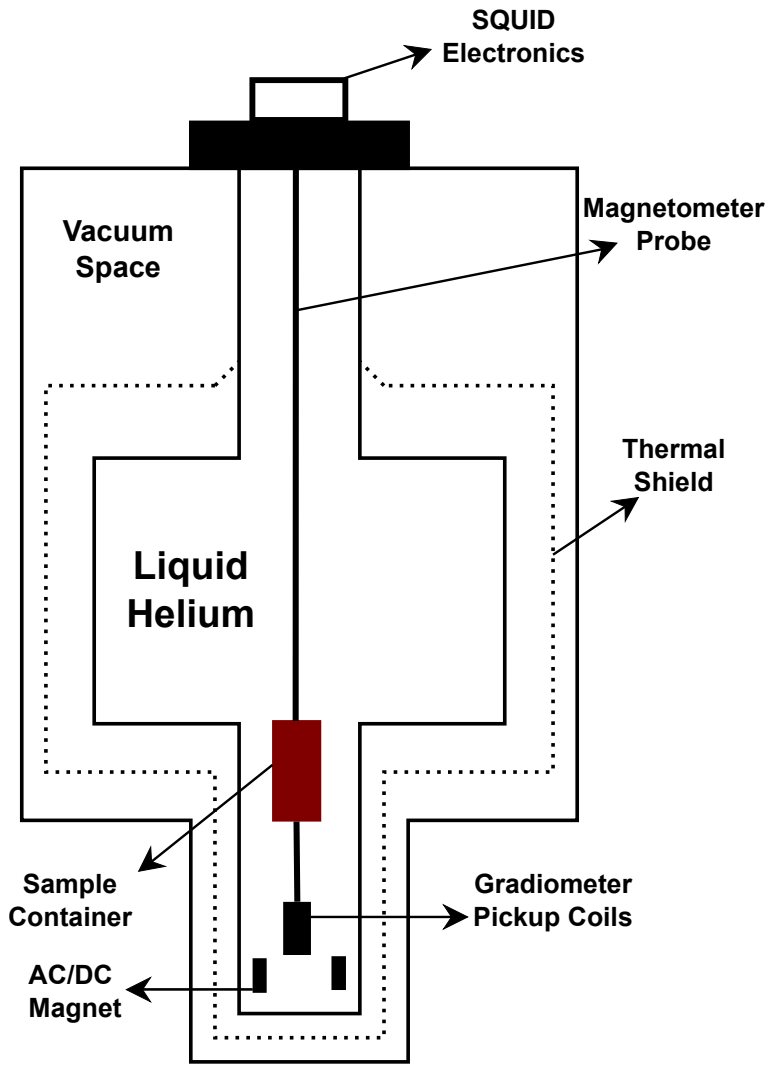

Figure 4.1: Cross sectional schematic diagram of a simple SQUID system (redrawn from Ref. [17]).

4.1.1 SQUID Results and discussion

The SQUID measurements performed by a MPMS-XL Quantum Design magnetometer. Magnetic moment versus applied magnetic field (MH) measurements performed at 5 K and 300 K with a maximum applied magnetic field of 70 kOe

for all samples except sample E4 which measured at maximum 50 kOe. The weight of materials used for the experiments are 7.5 , 8.8, 10.8, 17.8 and 10.2 mg for samples T6, T5, E6, E5, E4, respectively, and all the results are normalised to the weight of the sample. Temperature dependent ZFC and FC magnetization measurements were obtained with the same system for a range of temperature between < 2 K and 300 K with an applied magnetic field of 100 Oe.

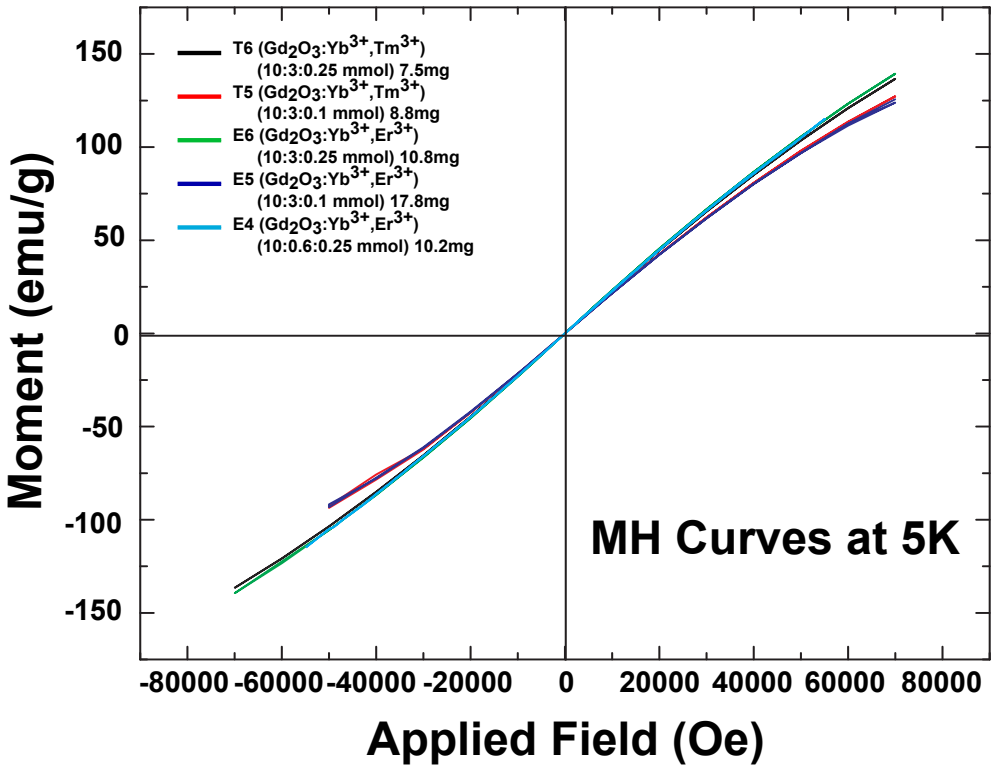

Figure 4.2: MH curve of Er^{+3} and Tm^{+3} doped samples at 5 K. All samples show similar behaviour with a curvature without absolute saturation and no observable hystresis. Samples T5 (red) and E5 (dark blue) show less susceptibility and higher curvature than other samples.

Figure 4.2 illustrates the measured MH curves of nanoparticles doped with Er^{+3} and Tm^{+3} at 5 K temperature for samples T5, T6, E5, E6 and E4, demonstrating similar magnetisation behaviour for all samples. Although none of the samples reach saturation and there is no hysteresis at this temperature, a curvature is observed in the MH curves, indicating a saturation at around 105 emu g^{-1}. The curvature of the sample T6, E6 and E4 is completely identical, while it is slightly higher for samples E5 and T5 and the curves approach the saturation point faster. The observed MH results for samples T5 and E5 can be justified by the lower Gd percentage reported as compared to samples T6, E6 and E4 in ICP spectroscopy results. The percentage of Gd appeared in samples T5 and E5 is 55.29% and 60.6%, respectively, whereas this is 66.17%, 66.02% and 76.42% for samples T6, E6 and E4, respectively. From this graph a magnetic mass susceptibility χ of 2.5×10^{-3} emu/Oe.g at 5 K is extracted from the slope of the curves in the linear central region using Equation 1.13.

As illustrated in Figure 4.3 the MH curves of Gd_2O_3 samples doped with Yb^{+3}:Er^{+3} or Yb^{+3}:Tm^{+3} at room temperature (300 K) shows no curvature, an indication for a typical paramagnetic materials [5, 167]. From this figure, the magnetic mass susceptibility can be extracted as 1.33×10^{-4} emu/Oe.g at room temperature. Sample E4 shows slightly higher susceptibility possibly due to the smaller dopant concentration in sample E4 (10:0.6:0.25) and the higher Gd percentage in the final synthesized sample measured by ICP spectroscopy as 76.42%.

Figure 4.4 illustrates the zero-field-cooled (ZFC)/ field-cooled (FC) curves

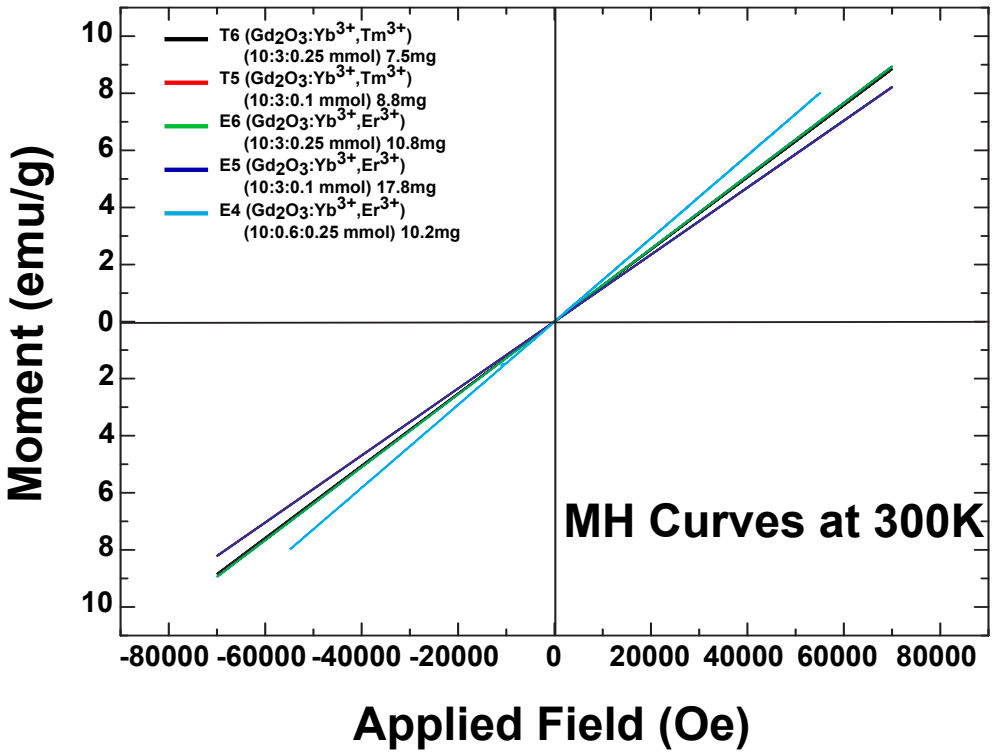

Figure 4.3: Magnetic behaviour of Tm^{3+} and Er^{3+} doped samples at 300 K. All samples shows linear pattern which is a typical behaviour of paramagnetic material. Sample E4 (light blue) show the highest magnetic mass susceptibility.

of the samples as a function of temperature. All samples show similar behaviour which is a clear evidence of the paramagnetic behaviour obtained from all samples, not affected with dopant concentration or different types of lanthanide used as dopants. The ZFC/FC results shows the typical signature $1/T$ behaviour for paramagnetic materials, which corroborates with the absence of blocking temperature and splitting between FC and ZFC [164]. The lack of hysteresis and absolute saturation in MH graphs and lack of splitting in ZFC-FC rules out the possibility of superparamagnetic behaviour and this is in accordance to the size range of the particles synthesised as the superparamagnetic behaviour is

reported in ultra small Gd_2O_3 nanoparticles with size range of around 3 nm [164].

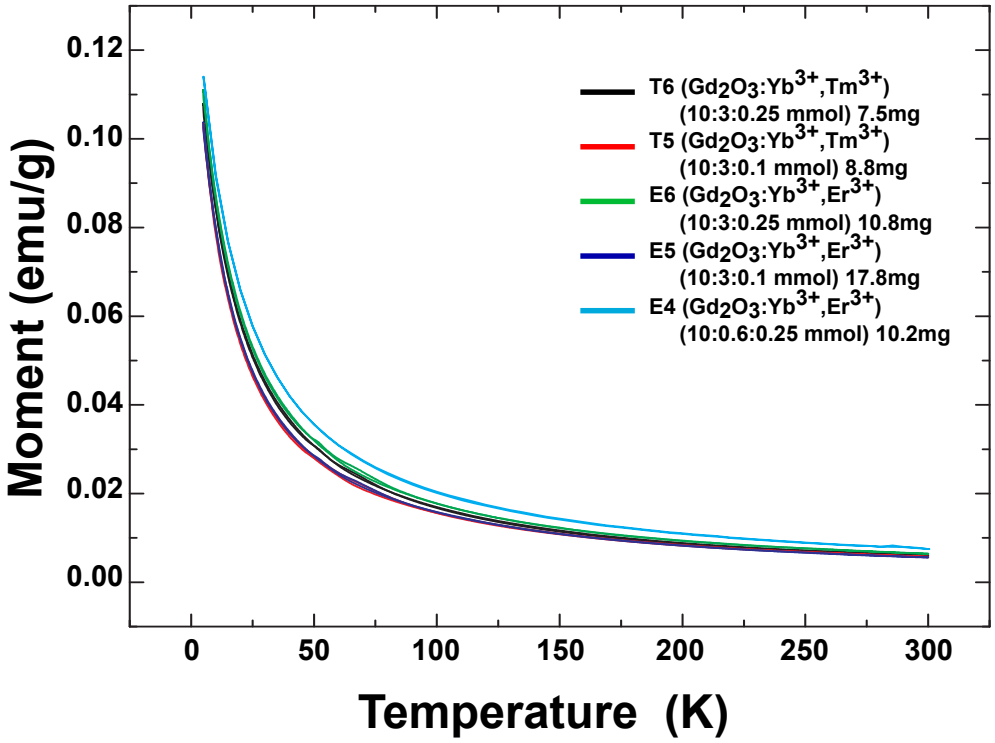

Figure 4.4: zero-field-cooled (ZFC) field-cooled (FC) measurements of Tm^{3+} and Er^{3+} doped samples. No blocking temperature and splitting suggest the paramagnetic properties of the samples.

4.2 Magnetic Force Microscopy

Magnetic force microscopy (MFM) belongs to atomic force microscopy (AFM) family of measurements and is based on the interaction between a magnetised cantilever tip with surface of a sample. A flexible cantilever with typical size of

around 200 μm long, 30 μm wide and 3 μm thick with a sharp magnetic tip is used as a force sensor. The force on the cantilever is measured by measuring changes on the reflection of a laser beam focused on the tip of the cantilever. When a small force $F_z = F_0 \cos(\omega t)$ at a frequency ω interacts with the cantilever causes the tip to oscillate with a displacement z given by

$$z = z_0 \cos(\omega t + \phi(\omega)), \tag{4.1}$$

where ϕ is the phase difference between oscillations of the tip and external force [168]. The amplitude z_0 of the oscillations is given by

$$z_0 = \frac{F_0}{m\sqrt{(\omega_0^2 - \omega^2)^2 + (\frac{\omega_0 \omega}{Q})^2}}, \tag{4.2}$$

where m is the mass of the tip, Q the quality factor representing the ratio of energy stored in the cantilever to the energy lost per cycle, $\omega_0 = \sqrt(k/m)$ the natural oscillation frequency of the cantilever and k the spring constant of the tip. The phase shift ϕ reads

$$\phi = \tan^{-1}\left(\frac{\omega\omega_0}{Q(\omega_0^2 - \omega^2)}\right). \tag{4.3}$$

The force on the magnetic tip increases as it approaches the magnetic sample, leading to a change in the resonance frequency $\Delta\omega$ given by

$$\Delta\omega = -\frac{\omega_0}{2k}\frac{\partial F_z}{\partial z}. \tag{4.4}$$

The above equation signifies that when a force attracts the cantilever, the resonance frequency of the cantilever decreases and for forces pushing the cantilever

away the resonance frequency of the cantilever increases [168].

When using a magnetized tip, the energy of the cantilever tip/sample U can be written as

$$U = -\mu_0 \int_{tip} \vec{M}_{tip} \vec{H}_{sample} dV_{tip}, \tag{4.5}$$

where μ_0 is the magnetic permeability of vacuum, $\vec{M}_{tip}$ is the magnetization of the cantilever tip and $\vec{H}_{sample}$ is the magnetic field of the sample. The force is thus derived by

$$\vec{F} = -\nabla U = \mu_0 (\vec{M}_{tip} \cdot \vec{\nabla}) \vec{H}_{sample}. \tag{4.6}$$

One of the most important issues in MFM measurement is distinguishing between magnetic forces interact with cantilever and other forces such as vibrational or electrostatic forces. In order to achieve this goal, we use the tapping mode and lifting mode to carry out MFM experiments. Figure 4.5 shows a schematic of the idea of the two-pass experiment. In a two-pass experiment, the sample is first topologically assessed by using the tapping mode, meaning that the cantilever oscillates with a certain frequency while moving and scanning the sample. After the first scan cantilever is lifted from the sample to a required height Δz to avoid the surface electrostatic forces and measurement is done only for the long-range magnetic forces [18, 169].

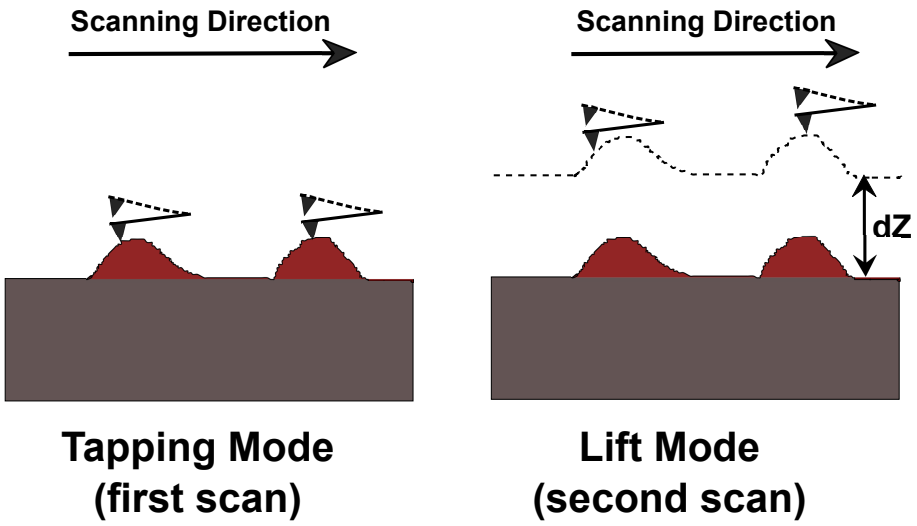

Figure 4.5: Schematic of a two-pass scanning magnetic force microscopy (MFM). First scan is the topographic tapping mode for morphological characterization followed by second scan which is the lift mode to measure the magnetic interactions (redrawn using [18]).

4.2.1 Experimental Method

We have performed magnetic force microscopy (MFM) on sample E4 (Gd_2O_3:Yb^{3+}, Er^{3+}) as it has the most intense upconversion emission as illustrated in Figure 3.15 and also it has the highest magnetic susceptibility between the synthesised samples, as shown in Figure 4.3. We have tried the same experiment on commercial nickel nanoparticles as well, so as to compare behaviour of ferromagnetic nickel with paramagnetic Gd_2O_3 nanoparticles. The experiment are carried out by a Veeco Dimension 3000 AFM by using commercially available Veeco MFM cantilevers with 225 micron length and with a resonant frequency f_0 between 60 and 100 kHz. The tip is a conducting antimony doped silicon coated with chrome and cobalt and then magnetized to a Coercivity of $\sim$ 400 Oe and a

spring constant in the order of 1 – 5 N/m.

To get high quality AFM and MFM images, a delicate sample preparation is required as particles need to rigidly adhere to the substrate that has a roughness less than the size of the nanoparticles. A sliced silicon wafer is used as a substrate, which is washed first with isopropyl alcohol (IPA) during a 30 minute ultrasonication. The substrate is then placed in an aminopropyltriethoxy silane (APTES) saturated desiccator for 24 hours in order to get a very thin film layer of APTES on the surface of silicon to enhance adhesion of nanoparticles. Meanwhile, 10 mg of Gd_2O_3:Yb^{3+}, Er^{3+} or nickel nanopowder is diluted in 10 ml DI water and subjected to 30 minutes ultrasonication to get a homogeneous dispersion of the nanoparticles. The dispersions are then diluted with DI water 5 times. A drop of the diluted nanoparticle dispersions is placed on the APTES modified substrate and dried at room temperature under nitrogen. The prepared samples is then used in MFM and AFM measurements [170].

AFM imaging performed using the tapping mode by the above-mentioned magnetised tip to get the morphological image of the particles. Then, the tip is lifted away from the sample by 90 nm, at which distance the surface forces such as Van der Waals and the electrostatic forces are negligible and only the magnetic interaction of the particles and magnetised tip is recorded. The result of AFM and MFM experiments will be discussed in the following section.

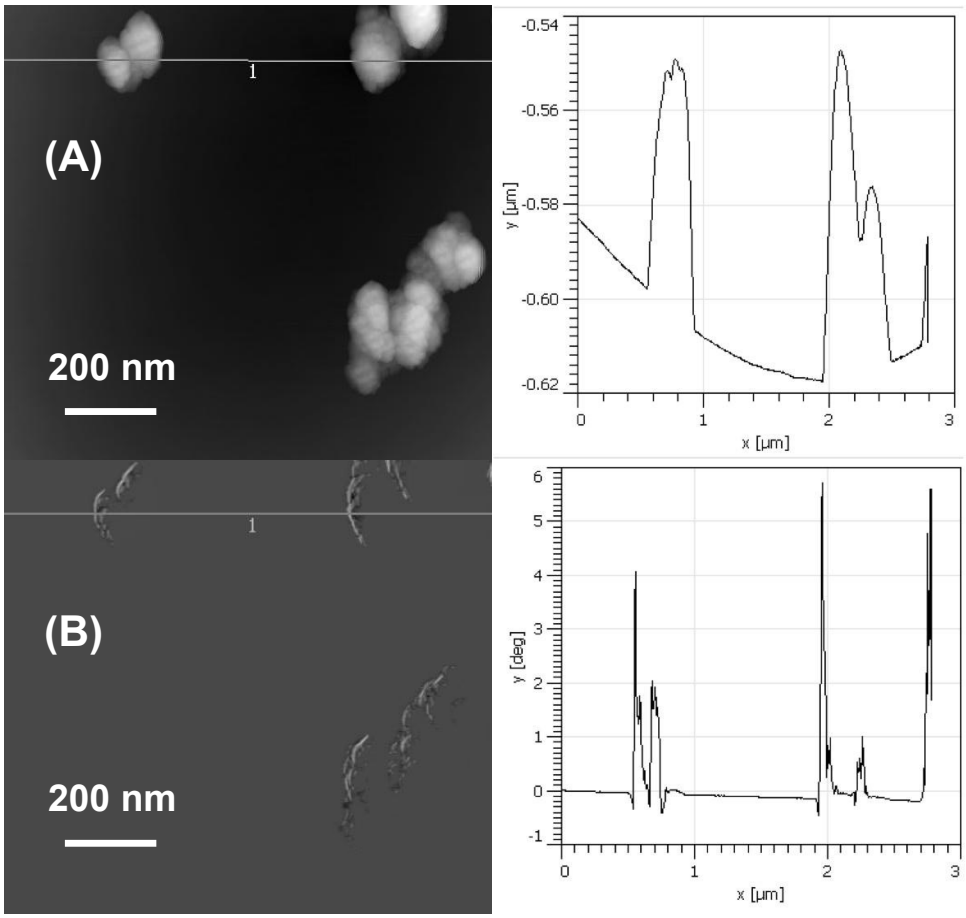

Figure 4.6: Atomic force microscopy (A) and magnetic force microscopy (B) measurement results with corresponding phase shift graphs of sample E4 (Gd_2O_3:Yb^{3+}, Er^{3+}) on the illustrated scan lines.

4.2.2 Magnetic Force Microscopy Results and Discussion

Figure 4.6 illustrates the AFM and MFM photomicrgraphs and their corresponding phase diagrams for nanoparticles from sample E4 (Gd_2O_3:Yb^{3+}, Er^{3+}). As illustrated, the AFM micrograph (A) illustrates clusters of spherical particles with a size range of around 100 – 200 nm diameter and 1 μm height. The graph on the right of the AFM micrgraph shows the cantilever amplitude related to

the topography measurement of particles on the shown scan line. MFM micrograph (B) shows the MFM image derived by repeating the experiment by lifting the cantilever by 90 nm and shows the magnetic interaction of magnetized tip with the paramagnetic field of Gd_2O_3:Yb^{3+}, Er^{3+} nanoparticles induced by the magnetic field of the tip during the AFM scan. A small negative phase shift is detected when the tip reaches the surface of the particles followed by sharp spikes, indicating oscillation of the tip due to the magnetic its interaction with the particle magnetic field.

We have perform similar AFM and MFM imaging on commercial nickel nanoparticles. Figure 4.7 demonstrates the result for this experiment. In part (A) the topography image of a cluster of nickel nanoparticles with 200 nm diameter and approximately 700 nm height. Part (B) illustrates the MFM image from the same cluster while the cantilever is lifted by 90 nm from the sample. The cluster of nanoparticle is disappeared in this image, signifying that the cantilever does not have interaction with the magnetic field of the nickel particles at this height. The graph next to picture (B) shows the phase shift of the cantilever while imaging the nanoparticles cluster and it illustrates no obvious phase shift related to detection of the particles.

Comparing results from ferromagnetic nickel nanoparticles (Figure 4.7) and paramagnetic Gd_2O_3:Yb^{3+}, Er^{3+} (Figure 4.6), it is arguable that although the AFM images, part (A) in both figures, shows similar topography of the particles with different size range, but the recorded MFM micrographs, part (B) in both figures, are completely different. By lifting the cantilever by 90 nm from the

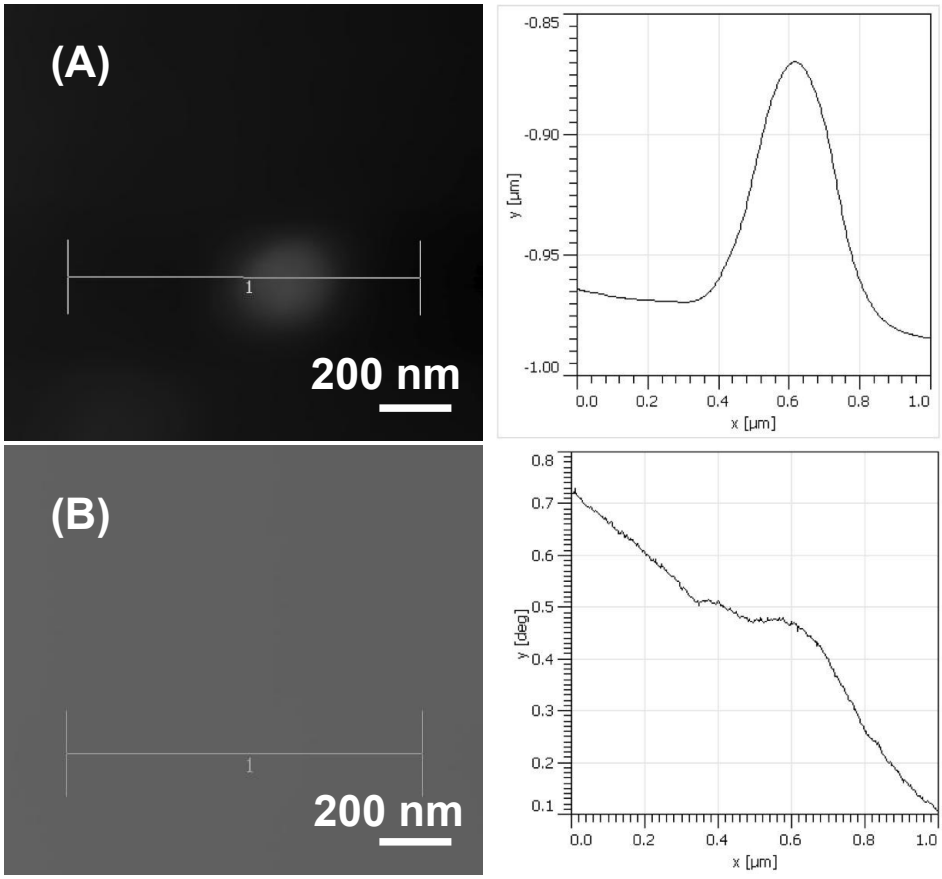

Figure 4.7: Atomic force microscopy (A) and magnetic force microscopy (B) results with corresponding phase shift graphs of nickel nanoparticles.

surface of the samples, in case of nickel nanoparticle there is no obvious phase shift while for the Gd_2O_3:Yb^{3+}, Er^{3+} a sharp and strong phase shift is detected especially at the surface of the particles. This result can be justified by keeping in mind that nickel nanoparticles are ferromagnetic and therefore the magnetic field of the particles is unrelated to the magenetization of the tip and therefore by lifting the cantilever to 90 nm from the sample no oscilating interaction will be caused. While, the Gd_2O_3:Yb^{3+}, Er^{3+} nanoparticles are paramagnetic and

the magnetic field of the particles is induced by the magnetic field of the tip, therefore when the very similar but opposite field from the tip and particles interact with each other, a strong oscilating interaction occurs.

4.3 Conclusion

In this chapter, magnetic characterization of the synthesized Gd_2O_3:Yb^{3+}, Er^{3+} and Gd_2O_3:Yb^{3+}, Tm^{3+} samples have been described. These nanoparticles exhibit paramagnetic behaviour and therefore have a strong potential application as a positive MRI contrast. The SQUID measurements not only proved the paramagnetic behaviour of the particles, but also showed that the magnetic properties of these nanoparticles are not affected by the kind of dopants and concentration of the dopants. Thus, the most important factor affecting the magnetic properties of the particles is host material, in this case Gd, which provides a constant and stable magnetic behaviour for these nanoparticles. This is an important point because it means that it is possible to dope Gd_2O_3 nanoparticles with different elements in order to get different upconversion emission colour with higher intensity and better efficiency without altering the magnetic behaviour of the particles.

I have also performed magnetic force microscopy that shows the possibility of magnetic characterization on single nanoparticle. The comparison of MFM results of commercially available nickel nanoparticles with Gd_2O_3:Yb^{3+}, Er^{3+} nanoparticles synthesized in this work illustrated a completely different reaction

between the MFM cantilever and magnetic field of the particles. In case of the paramagnetic Gd_2O_3:Yb^{3+}, Er^{3+} the interaction of the magnetized tip and the induced magnetic field of the particles produce a strong oscillation. This reaction did not happen for ferromagnetic nickel nanoparticles.

Testing properties of these nanoparticles in MRI experiments is an interesting future work that requires customizable MRI test systems. Another interesting experiment is to perform MFM experiments on a single particle with both magnetized and normal tip and comparing the effect of the magnetized tip on single particles. The main challenge for this experiment is bringing back the tip to exactly the same particle on the sample.

Chapter 5

Potential for Multi-Modal *In Vitro* and *In Vivo* Bio-Imaging

5.1 *In Vitro* Optical Imaging and Use of Upconversion Nanoparticles

Upconversion nanoparticles provide unique optical properties, described in Section 1.6.2, such as sharp, blinking-free and long lifetime luminescence, high photostability, possibility for using low power continuous wave lasers as excitation source and tunable emission. Because of these, there exists a huge interest for their applications in bioimaging and biological experimentation. The first potential field that upconversion nanoparticles can play an important role is *in*

vitro bioimaging.

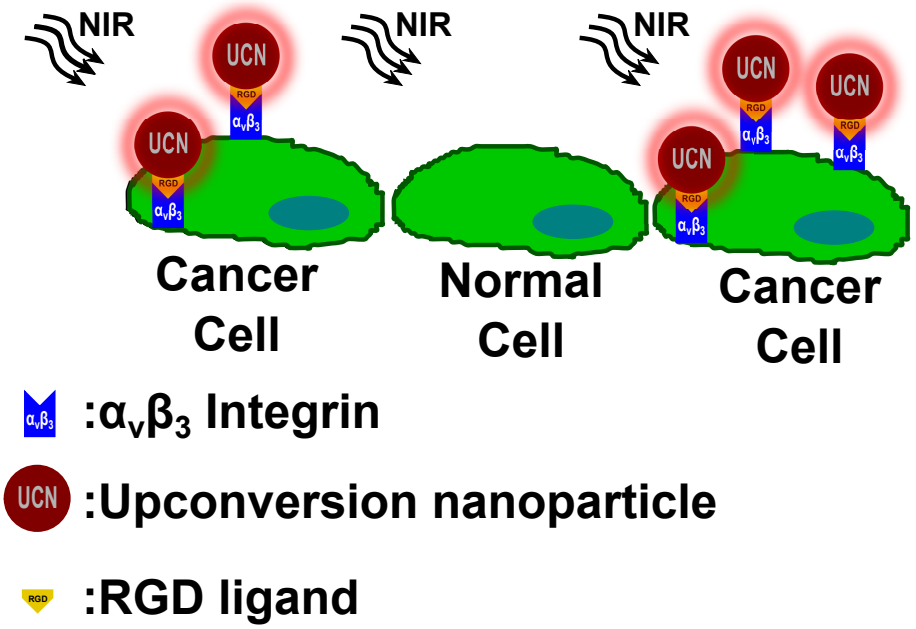

Figure 5.1: Schematic of how RGD modified upconversion nanoparticles distinguish between a normal cell without specific integrin $\alpha_v\beta_3$ expression and a cancer cell with integrin on its cell surface.

First *in vitro* application of upconversion nanoparticles is using them for targeted detection of normal cells and pathological cells such as cancer cells. The idea is to attach a ligand that can specifically detect a target, so as to detect for example a cancer cell from a normal cell. A famous example of a clinically useful ligand is arginine–glycine–asparatic acid (RGD) peptide. RGD can be attached to integrin $\alpha_v\beta_3$ specifically and as these integrins are expressed in some cancer cells but not in normal cells, it is possible to distinguish these two types of cells by doing an optical image. Figure 5.1 shows a schematic of

how RGD modified upconversion nanoparticles can be immobilizer on a cancer cell with integrin expression but not on the surface of a normal cell. This type of targeted detection reported recently by different groups and prove the applicability of upconversion nanoparticles [171, 172]. There are many other clinically important targets with their specific targets that could be developed in the same way for *in vitro* bioimaging. Although the *in vitro* detection of two different cells is far from a real clinical application but it is possible to think that by developing specific ligands for specific targets it is possible to increase the specificity and selectivity of clinical pathology by using nanoparticles for *in vitro* bioimaging.

Second example is the application of upconversion nanoparticles for heterogeneous bioassays. In this application, a substrate is covered with molecules that can capture and immobilize specific analyte molecules in a test sample or solution to give a quantitative measure of the amount of analytes. Figure 5.2 illustrates a schematic of a heterogeneous assay system using upconversion nanoparticles. In a competitive assay, free analytes in a sample compete with analytes modified by upconversion nanoparticles for immobilization on the surface molecules. The setup is washed after letting the system to settle to remove unattached analytes or nanoparticles. The substrate is then excited by a NIR excitation beam and the emission from the immobilized nanoparticle-modified analytes is detected. In this case the amount of analyte is inversely proportional to the emission intensity. In a non-competitive assay, probes modified by upconversion nanoparticles are captured on top of analytes immobilized on the capture molecule in a sandwich structure. After washing the substrate the

remaining particles are subjected to NIR excitation. In this case, the intensity of upconversion luminescence is directly proportional to the concentration of analytes [19].

Although for *in vitro* applications even μm size particles can be suitable, but smaller particles lead to better target-to-reporter ratio and higher quality results. One advantage of using upconversion nanoparticles for *in vitro* bio-applications is the lack of autofluorescence in the samples due to the low energy NIR laser as excitation source. Limited or no autofluorescence means higher signal to noise ratio (SNR) that results in higher image resolution and more sensitive quantitative results. It is important to keep in mind that, unlike quantum dots (QDs), emission wavelength of upconversion nanoparticles is not related to their size but defined by the type of activator used in the particles. This means that it is possible to get different emission colours from very similar particles and with the same NIR excitation source. This is a massive advantage as it provides possibility of simultaneous multicolour imaging and multicolour assays for different targets.

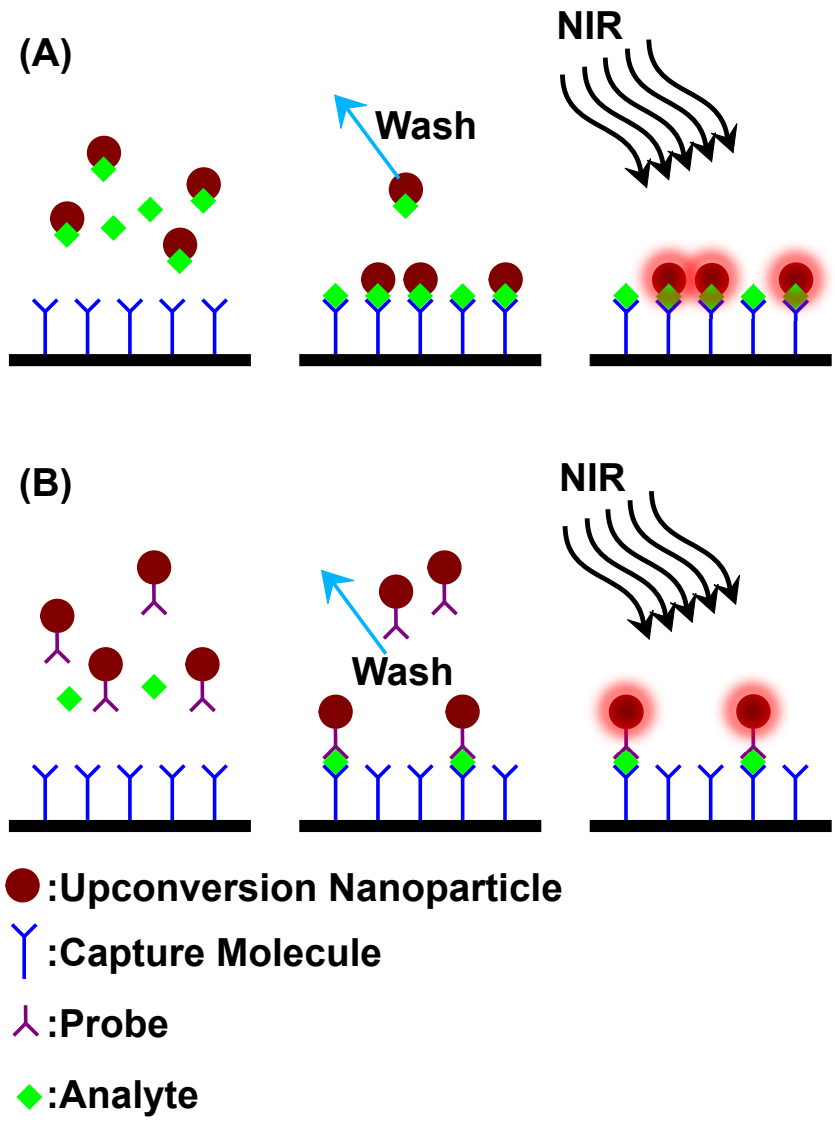

Figure 5.2: Mechanism of heterogeneous bioassays with upconversion nanoparticles. (A) A competitive assay, in which free analytes compete with analytes modified with nanoparticles, (B) A non-competitive assay in which analytes are sandwiched between probe and capture molecule. After being washed the amount of analytes can be quantified by the emitted signal from nanoparticles excited with NIR beam (redrawn from [19]).

5.2 *In Vivo* Bio-Imaging with Upconversion Nanoparticles: Animal Scans and Intra Operation Imaging

Recently, in view of the progress in development of high quality and efficiency upconversion nanoparticles, these nanoparticles have started to play an important role as an alternative for conventional dyes used for molecular imaging [173, 174]. Upconversion nanoparticles have some important advantages over other nanoparticles and imaging probes especially for *in vivo* applications. First advantage of upconversion nanoparticles is the use of NIR sources, as discussed in Section 1.3.3, resulting in less autoflourescence emission from bio-samples and higher signal to noise ratio and better image quality [107]. In addition, NIR excitations enable a deeper tissue penetration [175, 176]. Another advantage of upconversion nanoparticles for *in vivo* applications is the possibility for multicolour emission depending on the type of dopants used in synthesis of the nanoparticles using a single NIR excitation source. The emission from these nanoparticles are sharp with unique signature, without any overlap with excitation source which improves the imaging sensitivity.

To use the NIR-biological window, which enables deeper tissue penetration, upconversion by default has the excitation beam in the NIR region, but it is hard to get the emission in NIR region as well. Although recently pure or semi pure NIR to NIR upconversion nanoparticles are reported [53, 163], there is still a need to develop particles with high conversion efficiency and pure NIR-to-NIR upconversion. In this work, we have demonstrated pure NIR-to-NIR upconver-

sion nanoparticles. These particles are excited with different wavelength in the range of 900 to 1000 nm and emit pure upconversion centred at 810 nm. This will open huge potential application for *in vivo* imaging using upconversion nanoparticles.

There are two important factors involve in efficient application of nanoprticles for *in vivo* including size and the surface condition of nanoparticles. Particles need to be small enough to be able to pass biological barriers such as cell walls, endothelial layer and blood brain barrier and also to be able to avoid the reticuloendothelial system (RES) including lymph nodes, spleen and liver. On the other hand the very small particles can be filtered away rapidly in kidney. There are some contradictory reports about the effective particle size [22, 5], but it is possible to say that an ideal size is in the range between 10 – 100 nm depends on the *in vivo* application. The other important factor is the surface condition of the particles, generally speaking particles need to be covered with a layer of biocompatible material in order to be stealth from the immune system and RES, the most popular way of doing this is to cover particle with polyethylene glycol in a process referred to as PEGylation. Surface modified particles can resist the RES system and their blood circulation half-life increases by several orders of magnitude [22].

Pathological tissues especially tumour tissues have structural differences as compared to normal tissues. Examples of these differences include presence of angiogenic blood vessels and expression of specific target molecules. These differences can be employed for active and passive targeting of cancer cells and

pathologic tissues. In comparison to normal tissues tumour tissues have higher permeability because of endothelial pores with sizes varying from 10 to 1000 nm [177]. Also the lymphatic derange system is not working in tumorous tissues, and as a result, nanoparticles can easily get into the tumour tissues, are not easily removed, leading to accumulation in the tumour. Detection of the accumulated nanoparticles can indicate a tumour tissue in a passive mechanism that is referred to as the enhanced permeability and retention effect (EPR) [178], enabling passive targeting.

As the passive targeting is limited by structure of a tumour such as degree of tumour vasculature (related to the type of tumour) or pressure of solid tumours, the application of this type of targeting is limited. To overcome this issue, active targeting has been introduced, by using specifically activated and functionalized nanoparticles. An example for this type of targeting is the use of functionalized particles with RGD ligands, described in Section 5.1, and since integrin $\alpha_v\beta_3$ is expressed on the endothelial cells of some tumours, nanoparticles are immobilized and accumulated selectively on these targets to provide an intense emission for a sensitive detection.

Other groups recently have demonstrated the application of upconversion nanoparticles for *in vivo* imaging, especially in animal models [179, 163]. This is a novel subject of research, and for example to the best of our knowledge, there is no report for *in vivo* application of pure NIR-to-NIR upconversion nanoparticles, although there are some reports about using these type of particles in phantom tissues to illustrate deeper imaging penetration depth for this

nanoparticles. An example for application to animal models is to test the effect of new medical treatments on a particular cancer or other pathologies by targeted imaging of the targets related to that cancer. By trying these imaging techniques over time and comparing the presence of the target the effect of the medical treatment can be studied more effectively. This method can have significant, transformative effect on the laborious, time consuming process of discovering new medicines. As it is mentioned in Section 3.6, design and instrumentation of novel upconversion imaging systems are a novel field and there is no commercial system available for this type of imaging. Recently, Mahmood et. al. [180] reported a system for small animal upconversion imaging, which is a basic design for this type of imagers and signifies the opportunity for design and developing better and more practical imaging systems in this field.

An important example of clinical *in vivo* applications of nanoparticles is the detection of sentinel lymph node during surgery. The sentinel lymph node is the first lymph node or group of nodes infected by metastasizing cancer cells from a primary tumour. Use of nuclear modality (e.g., PET) has become the typical method for detection of sentinel lymph node in clinic. But this is limited due to danger of radiation from the nuclear contrasts, low quality images and cost of these imaging systems. Recently, there have been some reports about applications of magnetic nanoparticle for this purpose. Upconversion nanoparticles can play an important role, as the excitation source for these type of nanoparticles is a low cost conventional CW laser without adverse radiation effects. An important point is that optical modality suffers from low penetration depth, a problem that can be severely reduced by using NIR-to-NIR upconverison nanoparticles,

but in the case of surgery the tissues are exposed and therefore the limited penetration depth is not a major problem while the high sensitivity of optical modality could be used for an accurate detection of the sentinel lymph nodes.

The synthesized Gd_2O_3 based upconversion nanoparticles synthesized in this work are multimodal particles with optical and magnetic properties. This important property enables the possibility of using these type of nanoparticles as multimodal probe for biomedical imaging. The advantages of multimodality for *in vivo* application is the ability to use advantages of the two modalities to improve the effectiveness of imaging technique. For example, by using these type of particles for sentinel lymph nodes, it is possible to use the paramagnetic behaviour of the particles to get high quality anatomical MRI images overlapped with sensitive detection of the targets using optical imaging. And as both these two important and comprehensive diagnosis tools are performed by same particle it is much safer and more biocompatible than applying different contrasts for obtaining different images.

Although theoretically and to some extent practically it has been demonstrated that by using NIR biological window, it is possible to increase the penetration depth of the optical modality, it is important to mention that different tissues in the body have different anatomical, physiological and biophysicochemical properties and these properties can affect the accessibility and efficiency of the tissues for *in vivo* molecular imaging. For example, blood brain barrier (BBB) tissues have a barrier that separate brain from the general blood circulation in the body and therefore it is difficult and tricky to detect a target

inside the brain. Or for example, bones do not have a very dynamic circulation so it is not possible to use the circulation force for transferring imaging probes to the targets located in them. And also some tissues are located in some places in the body that is not possible to access them through skin, while some other tissues such as breast, skin, prostate, lymph nodes, and liver are more accessible thorough circulation and located in positions that could be easier for using the optical imaging. Although as will be discussed it is possible to use endsocopy techniques, as described in Section 5.3, but targets should be selected according to the properties of the tissue, their accessibility and the possibility to be imaged using the available modality.

5.3 *In Vivo* Endoscopic Use of Bio-Imaging Nanoparticles

Introduction of endoscopic imaging to medicine is one of the most important breakthroughs both for the diagnosis and treatment of illnesses, as it helps medics and surgeons to have access to tissues and organs *in vivo*. In recent years, the introduction of new technologies such as wide-field endoscopy, autofluorescence endoscopy, scanning fiber endoscopy, confocal endomicroscopy and two-photon endomicrsocopy has opened a new era in potentials of endoscopy for clinical diagnosis and treatments. Especially, the development of confocal and two-photon endomicroscopy can have revolutionary effects on molecular imaging using endoscopy. In confocal endomicroscopy, a single photon usually in the visible range is used to excite tissues and the emitted fluorescence beam is detected

by using the core of single mode optical fiber which acts as a filter to reject the scattered light except the light coming from the interested focal point. Using this method information form cancer cells have been detected in tissues as deep as 500 μm below the surface. On the other hand, in two-photon endomicroscopy, two NIR excitation beams excite the tissue simultaneously to produce a visible emission from the target of interest. Two-photon endomicroscopy brings some advantages such as less scattering in tissues, limited photo-bleaching and deeper depth penetration because of NIR excitation [181].

In all of the above-mentioned endomicroscopic methods, usage of targeted nanoparticles can enhance their sensitivity and selectivity. Applying upconversion nanoparticles as targeted probes can be a real opportunity to improve optical molecular imaging using endomicroscopy [182]. One important advantage of upconversion to even two-photon endoscopy is the possibility to couple a NIR continuous wave laser diode in an endoscope easily and there is no need for simultaneous excitation. On the other hand, another fiber optic with filters designed for the emission wavelength could be used for detection and as the emission coming from particles in the case of upconversion is sharp it is easy to detect the signal form any background emission that increases the sensitivity of images. Finally, possibility to get NIR-to-NIR upconversion nanoparticles as shown in this work, implies deeper penetration depth for both excitation and emission without minimal autofluorescence from background tissues.

5.4 Toxicology and Catabolism of Nanoparticles

Nanotechnology has attracted attention in the recent years as a technology that can play a crucial role in the future of medicine and bioscience. But like any other novel technology it also ignites questions about the acute and chronic effects of nanoparticles and nanostrsuctures on cells and tissues *in vitro* and *in vivo*. Traditionally, toxicology of materials is dose related, which means that medicines and chemicals can have different effects with different doses and can be toxic in certain dosages. This approach to toxicology changes to some extend in the case of nonmaterials as chemical and physical properties of material change in nano-scale. Because of this, for nanomaterial not only the dosage but also their type, size, shape, surface, charge, coating, dispersion, agglomeration and aggregation can play an important role in their toxic effect and their catabolism [183]. Another important point is that the surface layer of nanoparticles are much more important for their reactivity, and consequently, their toxicity, and this surface attracts biomaterial to form strong or weak bonds as soon as the nanoparticles enter a bio-matrix. The surface of a nanoparticles after being covered with biomaterial is called corona [184]. So not only the type of material that nanoparticles are built from is important, but the environment where the nanoparticles are going to be used in and thus the corona surface of the particles should be studied in toxicology studies.

In vitro toxic effects of nanoparticles on cells can be chemical or physical. The chemical mechanisms include production of reactive oxygen species (ROS), release of toxic ions, disturbance on cell membrane transport activity and oxidation damages. The physical mechanisms are also important and related to the

size and morphology of particles. These mechanisms include membrane activity disruption, blocking transport processes, disruption in protein synthesis mechanisms and aggregation of particles [183]. Adding all these mechanisms, the first organelle being affected is the cell membrane, which can be manipulated by surface modification of the particles, but particles can potentially disrupt normal functions of the cell membrane. Other vulnerable organelles in cells are mitochondria and lysosomes. There are some reports that carbon nanotubes can reach mitochondria and disrupt its function as the cell engine. Lysosomes are responsible for metabolism inside the cells and the observed disruption is believed to be generally due to accumulation of nanoparticles, but the catabolism process of nanoparticles inside lysosomes are not well understood yet [185, 183].

The *in vivo* toxicology and catabolism of nanoparticles is even more complicated and less revealed yet. The biodistribution studies of nanoparticles in animal models have shown that unrelated to how particles enter the body, traces of nanoparticles are detected in liver, spleen, heart and even brain [183]. It is even reported that silica nanoparticles and titanium dioxide particles in the size range of 35 to 70 nm cause pregnancy problems such as smaller fetus and presence of particles in fetus liver and brain [186]. Therefore, there is an urgent need for a comprehensive study of *in vivo* toxicological properties of nanoparticles.

Upconversion nanoparticles are not excepted to suffer extensively from the mentioned toxicology issues. Although rare-earth material are generally considered as non-toxic and bio-compatible [97], and there are some reports available on the *in vitro* and *in vivo* applications of these nanoparticles without any

acute toxic problems [187], but the longterm effects of these type of particles are not well understood. While Gd complexes is an FDA approved MRI contrast agent, but these type of material can cause heavy metal toxicity if used in high dosages or accumulated in tissues during longterm usage. In conclusion, although upconversion nanoparticles are far safer and biocompatible than other nanoparticles including QDs, but their catabolism and more importantly their longterm effects is still unknown, which requires significant attention.

Chapter 6

Conclusions

Upconversion Gd_2O_3:Yb^{3+}, Tm^{3+} and Gd_2O_3:Yb^{3+}, Er^{3+} nanoparticles have been synthesized using urea homogeneous precipitation (UHP) method. Tm^{3+} doped samples demonstrate pure near infrared to near infrared (NIR–to–NIR) upconversion emission centred at around 810 nm (associated to the $^3H_4 \rightarrow {}^3H_6$ energy transfer of Tm^{3+}), when excited with a low cost 975 nm continuous wave excitation laser in photoluminescence experiments. This places both excitation and emission wavelength in the biologically important window that has the highest penentration depth and minimal tissue autoflourescence, leading to increased image quality and signal to noise ratio. For Er^{3+} doped samples, upconversion emission mainly falls in the visible red region centred at 661 nm (attributed to the $^4F_{9/2} \rightarrow {}^4I_{15/2}$ energy transfer of Er^{3+}), when excited with the same infra red laser excitation. Effect of molar ratio of dopants and urea concentration used in the synthesis is systematically investigated for finding the best recipes for these particles. Morphological characterization, including scanning electron microscopy (SEM) and transmission electron microscopy (TEM)

shows spherical and oval monodispersed particles with a rough surface and a size distribution in the range of 50 to 150 nm. The size distribution and monodispersity tests using dynamic light scattering (DLS) approve the size distribution of the particles and demonstrate formation of acceptable aqueous dispersions and point out agglomeration challenges especially for bioimaging applications. The HR-TEM tests show a lattice distance of 4.1 Åfor Gd_2O_3:Yb^{3+}, Tm^{3+} and 4.6 Åfor Gd_2O_3:Yb^{3+}, Er^{3+} nanoparticles. The elemental analyses including inductively coupled plasma optical emission spectrometry (ICP-OES) and X-ray photoelectron spectroscopy demonstrate correlation between the starting molar ratios of the host and dopants and final concentrations of the ions in the resultant particles. XPS results also suggested that particles tend to absorb CO_2 from atmosphere but this has no effect on the particles optical and magnetic properties.

For sensitive optical characterization of the synthesized nanoparticles, we have developed a novel method for upconversion photoluminescence measurement using fourier transform infrared (FTIR) and visible spectrometer by which it is possible to get accurate and high resolution data with possibility of scanning whole spectrum without limitations of a conventional spectrophotometers for NIR-to-NIR applications. The most intense NIR-to-NIR emission is detected from the samples synthesized with 2 M of urea solution and doped with 3 mmol Yb^{3+} and 0.1 or 0.25 mmol Tm^{3+}. The highest upconversion intensity in the case of Er^{3+} doped samples belongs to samples doped with 0.6 mmol of Yb^{3+} and 0.25 mmol of Er^{3+} and syhthesized with 2 M urea stock solution. The photoluminescence decay measurements illustrate a single exponential de-

cay behaviour for Er^{3+} doped samples with a time constant of $\tau = 7.16$ μs. The Tm^{3+} doped samples, in contrast, demonstrate a distinguishable double exponential decay behaviour with a decay constant of $\tau_1 = 0.001$ μs and $\tau_2 = 0.13$ μs for the rapid and long tail decays, respectively. The photoluminescence and decay measurements suggest different energy transfer mechanisms responsible for the Tm^{3+} and Er^{3+} doped samples. The Tm^{3+} samples are more dependent on Yb^{3+} sensitisers, thus requiring a high (3 mmol) Yb^{3+} concentration for the most intense emission and a low activator concentration to prevent self quenching effects. In contrast, in Er^{3+} doped samples, Yb^{3+} dopant plays a much less critical role, since Er^{3+} also absorbs the excitation in addition to acting as an activator. Microscopic images of the nanoparticles illustrate the potential for using these upconversion nanoparticles in *in vitro* bioimaging. The emission detected from particles excited with a 980 nm is accurately correlated to the location of the particle clusters in the bright field image, illustrating a spatial resolution down to a micron. Other excitation wavelengths in the range of 900–1000 nm show similar upconversion emission.

Multimodal behaviour of Gd_2O_3:Yb^{3+}, Tm^{3+} and Gd_2O_3:Yb^{3+}, Er^{3+} upconversion nanoparticles is demonstrated by magnetic characterization of the synthesized nanoparticles. Superconducting quantum interference devices (SQUID) show no saturation and no hysteresis for MH measurements carried out at 5 K, but a curvature is present in the MH behaviour. A magnetic mass susceptibility χ of 2.5×10^{-3} emu/Oe.g at 5 K. MH curves of Gd_2O_3 samples doped with Er^{+3} or Tm^{+3} at room temperature (300 K) demonstrate no curvature, an indication for a typical paramagnetic materials and a magnetic mass susceptibility

of 1.33×10^{-4} emu/Oe. Zero-field-cooled (ZFC)/ field-cooled (FC) curves provide evidence of paramagnetic behaviour including the typical signature $1/T$ behaviour, absence of blocking temperature and lack of splitting between FC and ZFC. Magnetic force microscopy (MFM) show that synthesized nanoparticles produce positive phase difference on a magentized tip even at a lift height of 90 nm, whereas nickel nanoparticles do not show such a behaviour when the tip is lifted from the sample.

In addition to the above nanoparticles, we have synthesized Y_2O_3:Yb^{3+}, Er^{3+} and Y_2O_3:Yb^{3+}, Er^{3+} upconversion nanoparticles using similar UHP method, and we observed that Gd_2O_3 is a better host for upconversion nanoparticles in comparison to Y_2O_3 for providing a stronger emission. We investigated novel thermal decomposition method for synthesis of upconversion phosphors using organic co-ordination complexes as precursors. The synthesized Y_2O_3:Yb^{3+}, Er^{3+} particles have a size in the micrometer range with spherical shape and show strong upconversion emission in the red (661 nm) and green (560 nm) regions of the spectrum. Surfatants such as PEG, PVA and PAA have been used to control the morphology and size of the particles, and Y_2O_3:Yb^{3+}, Er^{3+} nanoparticles with diameters of 150 nm are demonstrated using PEG surfactants. We have also presented synthesis of upconversion nanoparticles using the combustion method for both Y_2O_3:Yb^{3+}, Er^{3+} and ZnO:Yb^{3+}, Er^{3+} but the upconversion emission from these samples are extremely low intensity and not comparable to the samples synthesiszed with other methods. We examined the effect of long term annealing on the combustion samples, showing a decrease in the emission intensity for at least three order of magnitude.

The results of this work for synthesis and characterization of multimodal magnetic and optical nanoparticles opens significant opportunities for novel *in vitro* and *in vivo* bioimaging applications. As mentioned in the next section, these results provide the foundation for significant improvements in the field of optical molecular and multimodal imaging with direct implications for better diagnosis and clinical applications.

6.1 Future Works

The future works that can be directly founded on the contributions of this thesis include:

1. *Progress in synthesis of upconversion nanoparticles.* Although in this work we have demonstrated fine and monodispersed Gd_2O_3 nanoparticles with pure NIR-to-NIR upconversion for particles doped with Tm^{3+} and NIR to visible for those doped with Er^{3+}, there exist many opportunities for novel synthesis routes. Using other lanthanide ions as dopants and using core-shell structures [10] can improve both the morphological and optical properties of the nanoparticles. We have tried synthesis using organic precursors and reported dramatic change in the morphology of the synthesized particles using surfactants. Applying surfactants on the fine particles synthesized with UBHP method is another idea worth trying to improve size and surface conditions of the particles.

2. *Surface modification and functionalization of the particles.* As mentioned

before to increase the efficiency of particles for bioimaging, especially for *in vivo* applications, surface modifications are required. For example, the surface modifications used for Y_2O_3 particles in literature [154] can be easily used for Gd_2O_3 particles and commercial availability of functionalized PEG makes the design of experiments for *in vitro* and *in vivo* bioimaging applications easier.

3. *Designing upconversion set-up both for in vitro and in vivo imaging.* As mentioned before, the lack of a standard setup for upconversion imaging is an important problem for sensitive optical and microscopy imaging experiments. This poses as a great experimental and commercial opportunity for development of next generation upconversion microscopy and clinical tools. An experimental setup can be arranged using commercially available multiphoton microscopes for *in vitro* experiments and designing flexible setups for animal experiments and other *in vivo* imaging applications.

4. *Performing in vitro and in vivo experiments. In vitro* and *in vitro* experiments are possible to perform with upconversion nanoparticles with different types of dopants that enable having multiple targets with multicolour tagging capability. Another opportunity is to try both MRI and optical imaging simultaneously to use advantages of both methods and enhance the possible clinical application of these particles.

5. *Toxicology and longterm safety experiments of upconversion nanoparticles.*

As mentioned, an important missing piece of the puzzle for application of nanoparticles for clinical applications is better understanding of toxicology, catabolism and longterm effects of nanoparticles. Designing experiments to overcome these issues is one of the most important future works in nanopaticle research area.

6. *Finding new targets with high specificity and selectivity for clinical applications.* We have briefly mentioned possible targets for clinical applications in this thesis. Development of new targets for specific *in vitro* and *in vivo* diagnosis and test applications is the key for connecting these nanoparticles to new applications in nanomedicine. Extensive research and collaboration with different research groups in basic medical science and clinical areas is one of the most important strategies to improve this novel field of science and technology.

Bibliography

[1] S. McNeil, "Nanotechnology for the biologist," *Journal of Leukocyte Biology*, vol. 78, no. 3, pp. 585–594, 2005.

[2] E. Hillman, "Experimental and theoretical investigations of near infrared tomographic imaging methods and clinical applications," 2002.

[3] R. Alfano and A. Katz, "Non invasive fluorescence-based instrumentation for cancer and precancer detection and screening," *In-Vitro Diagnostic Instrumentation*, pp. 223–226, 2000.

[4] R. Weissleder *et al.*, "A clearer vision for in vivo imaging.," *Nature Biotechnology*, vol. 19, no. 4, p. 316, 2001.

[5] Q. Pankhurst, J. Connolly, S. Jones, and J. Dobson, "Applications of magnetic nanoparticles in biomedicine," *Journal of Physics D: Applied Physics*, vol. 36, p. R167, 2003.

[6] I. Pykett, J. Newhouse, F. Buonanno, T. Brady, M. Goldman, J. Kistler, G. Pohost, *et al.*, "Principles of nuclear magnetic resonance imaging.," *Radiology*, vol. 143, no. 1, p. 157, 1982.

[7] P. Prasad, *Introduction to biophotonics*. John Wiley and Sons, 2003.

[8] F. Auzel, "Upconversion and anti-stokes processes with f and d ions in solids," *Chemical reviews*, vol. 104, no. 1, pp. 139–174, 2004.

[9] F. Wang and X. Liu, "Recent advances in the chemistry of lanthanide-doped upconversion nanocrystals," *Chem. Soc. Rev.*, vol. 38, no. 4, pp. 976–989, 2009.

[10] F. Wang, R. Deng, J. Wang, Q. Wang, Y. Han, H. Zhu, X. Chen, and X. Liu, "Tuning upconversion through energy migration in core–shell nanoparticles," *Nature Materials*, 2011.

[11] S. Eliseeva and J. Bünzli, "Lanthanide luminescence for functional materials and bio-sciences," *Chem. Soc. Rev.*, vol. 39, no. 1, pp. 189–227, 2009.

[12] M. Haase and H. Schäfer, "Upconverting nanoparticles," *Angewandte Chemie International Edition*, vol. 50, no. 26, pp. 5808–5829, 2011.

[13] C. Boss and K. Fredeen, *Concepts, instrumentation and techniques in inductively coupled plasma optical emission spectrometry.* Perkin Elmer, 1999.

[14] D. Schroder, *Semiconductor material and device characterization.* Wiley-IEEE Press, 2006.

[15] A. Kaminski?, *Crystalline lasers: physical processes and operating schemes*, vol. 12. CRC, 1996.

[16] J. Rietdorf and E. Stelzer, "Special optical elements," *Handbook of Biological Confocal Microscopy*, pp. 43–58, 2006.

[17] R. Fagaly, "Neuromagnetic instrumentation.," *Advances in neurology*, vol. 54, p. 11, 1990.

[18] Y. Zhang, M. Yang, M. Ozkan, and C. Ozkan, "Magnetic force microscopy of iron oxide nanoparticles and their cellular uptake," *Biotechnology progress*, vol. 25, no. 4, pp. 923–928, 2009.

[19] F. Wang, D. Banerjee, Y. Liu, X. Chen, and X. Liu, "Upconversion nanoparticles in biological labeling, imaging, and therapy," *Analyst*, vol. 135, no. 8, pp. 1839–1854, 2010.

[20] M. Pysz, S. Gambhir, and J. Willmann, "Molecular imaging: current status and emerging strategies," *Clinical radiology*, vol. 65, no. 7, pp. 500–516, 2010.

[21] R. Minchin and D. Martin, "Minireview: nanoparticles for molecular imagingan overview," *Endocrinology*, vol. 151, no. 2, p. 474, 2010.

[22] P. Debbage and W. Jaschke, "Molecular imaging with nanoparticles: giant roles for dwarf actors," *Histochemistry and cell biology*, vol. 130, no. 5, pp. 845–875, 2008.

[23] P. Sharma, S. Brown, G. Walter, S. Santra, and B. Moudgil, "Nanoparticles for bioimaging," *Advances in colloid and interface science*, vol. 123, pp. 471–485, 2006.

[24] R. Hashemi, W. Bradley, and C. Lisanti, *MRI: the basics*. Lippincott Williams & Wilkins, 2010.

[25] S. Jiang, M. Gnanasammandhan, and Y. Zhang, "Optical imaging-guided cancer therapy with fluorescent nanoparticles," *Journal of the Royal Society Interface*, vol. 7, no. 42, pp. 3–18, 2010.

[26] R. Lawaczeck, H. Bauer, T. Frenzel, M. Hasegawa, Y. Ito, K. Kito, N. Miwa, H. Tsutsui, H. Vogler, and H. Weinmann, "Magnetic iron oxide particles coated with carboxydextran for parenteral administration and liver contrasting," *Acta Radiologica*, vol. 38, no. 4, pp. 584–597, 1997.

[27] Y. Jun, J. Lee, and J. Cheon, "Chemical design of nanoparticle probes for high-performance magnetic resonance imaging," *Angewandte Chemie International Edition*, vol. 47, no. 28, pp. 5122–5135, 2008.

[28] J. Choi, J. Lee, T. Shin, H. Song, E. Kim, and J. Cheon, "Self-confirming "AND" logic nanoparticles for fault-free MRI," *Journal of the American Chemical Society*, 2010.

[29] Q. Pankhurst, N. Thanh, S. Jones, and J. Dobson, "Progress in applications of magnetic nanoparticles in biomedicine," *Journal of Physics D: Applied Physics*, vol. 42, p. 224001, 2009.

[30] G. Xing, H. Yuan, R. He, X. Gao, L. Jing, F. Zhao, Z. Chai, and Y. Zhao, "The strong MRI relaxivity of paramagnetic nanoparticles," *The Journal of Physical Chemistry B*, vol. 112, no. 20, pp. 6288–6291, 2008.

[31] R. Nagarajan and T. Hatton, *Nanoparticles: synthesis, stabilization, passivation, and functionalization*, vol. 996. Oxford University Press, USA, 2008.

[32] S. Caruthers, S. Wickline, and G. Lanza, "Nanotechnological applications in medicine," *Current opinion in biotechnology*, vol. 18, no. 1, pp. 26–30, 2007.

[33] V. Vogel, *Nanotechnology. Vol. 5, Nanomedicine*. Wiley-VCH, 2009.

[34] W. De Herder, D. Kwekkeboom, R. Valkema, R. Feelders, M. Van Aken, S. Lamberts, A. van der Lely, E. Krenning, *et al.*, "Neuroendocrine tumors and somatostatin: imaging techniques.," *Journal of endocrinological investigation*, vol. 28, no. 11 Suppl International, p. 132, 2005.

[35] F. Wiesinger, V. De Moortele, G. Adriany, N. De Zanche, K. Ugurbil, K. Pruessmann, *et al.*, "Parallel imaging performance as a function of field strengthan experimental investigation using electrodynamic scaling," *Magnetic resonance in medicine*, vol. 52, no. 5, pp. 953–964, 2004.

[36] R. Dashner, A. Kangarlu, D. Clark, A. RayChaudhury, and D. Chakeres, "Limits of 8-tesla magnetic resonance imaging spatial resolution of the deoxygenated cerebral microvasculature," *Journal of Magnetic Resonance Imaging*, vol. 19, no. 3, pp. 303–307, 2004.

[37] I. Paschkunova-Martic, C. Kremser, K. Mistlberger, N. Shcherbakova, H. Dietrich, H. Talasz, Y. Zou, B. Hugl, M. Galanski, E. Sölder, *et al.*, "Design, synthesis, physical and chemical characterisation, and biological interactions of lectin-targeted latex nanoparticles bearing Gd–DTPA chelates: an exploration of magnetic resonance molecular imaging (MRMI)," *Histochemistry and cell biology*, vol. 123, no. 3, pp. 283–301, 2005.

[38] S. Zhang, X. Zhu, Z. Chen, C. Cai, T. Lin, and J. Zhong, "Improvement in the contrast of CEST MRI via intermolecular double quantum coherences," *Physics in Medicine and Biology*, vol. 53, p. N287, 2008.

[39] M. Woods, D. Woessner, and A. Sherry, "Paramagnetic lanthanide complexes as PARACEST agents for medical imaging," *Chem. Soc. Rev.*, vol. 35, no. 6, pp. 500–511, 2006.

[40] S. Worthy, "High resolution computed tomography of the lungs," *BMJ*, vol. 310, no. 6980, p. 616, 1995.

[41] R. Popovtzer, A. Agrawal, N. Kotov, A. Popovtzer, J. Balter, T. Carey, and R. Kopelman, "Targeted gold nanoparticles enable molecular CT imaging of cancer," *Nano letters*, vol. 8, no. 12, pp. 4593–4596, 2008.

[42] J. Lindner, "Evolving applications for contrast ultrasound," *The American journal of cardiology*, vol. 90, no. 10, pp. 72–80, 2002.

[43] A. Bennett, *Phase microscopy: principles and applications*. Wiley, 1951.

[44] F. Bolin, L. Preuss, R. Taylor, and R. Ference, "Refractive index of some mammalian tissues using a fiber optic cladding method," *Applied optics*, vol. 28, no. 12, pp. 2297–2303, 1989.

[45] W. Cheong, S. Prahl, and A. Welch, "A review of the optical properties of biological tissues," *Quantum Electronics, IEEE Journal of*, vol. 26, no. 12, pp. 2166–2185, 1990.

[46] J. Beek, P. Blokland, P. Posthumus, M. Aalders, J. Pickering, H. Sterenborg, and M. Gemert, "In vitro double-integrating-sphere optical proper-

ties of tissues between 630 and 1064 nm," *Physics in medicine and biology*, vol. 42, p. 2255, 1997.

[47] A. Torricelli, A. Pifferi, P. Taroni, E. Giambattistelli, and R. Cubeddu, "In vivo optical characterization of human tissues from 610 to 1010 nm by time-resolved reflectance spectroscopy," *Physics in medicine and biology*, vol. 46, p. 2227, 2001.

[48] M. Firbank, M. Hiraoka, M. Essenpreis, and D. Delpy, "Measurement of the optical properties of the skull in the wavelength range 650–950 nm," *Physics in medicine and biology*, vol. 38, p. 503, 1993.

[49] C. Simpson, M. Kohl, M. Essenpreis, and M. Cope, "Near-infrared optical properties of ex vivo human skin and subcutaneous tissues measured using the monte carlo inversion technique," *Physics in Medicine and Biology*, vol. 43, p. 2465, 1998.

[50] J. Ritz, A. Roggan, C. Isbert, G. Müller, H. Buhr, and C. Germer, "Optical properties of native and coagulated porcine liver tissue between 400 and 2400 nm," *Lasers in surgery and medicine*, vol. 29, no. 3, pp. 205–212, 2001.

[51] V. Hollis, T. Binzoni, and D. Delpy, *Non-invasive monitoring of brain tissue temperature by near-infrared spectroscopy.* PhD thesis, University of London, 2002.

[52] A. Katz and R. Alfano, "Non invasive fluorescence-based instrumentation for cancer and precancer detection and screening," in *SPIE proceedings series*, pp. 223–226, Society of Photo-Optical Instrumentation Engineers, 2000.

[53] H. Wong, H. Chan, and J. Hao, "Towards pure near-infrared to near-infrared upconversion of multifunctional GdF_3: Yb^{3+}, Tm^{3+} nanoparticles," *Optics Express*, vol. 18, no. 6, pp. 6123–6130, 2010.

[54] A. Morrish, "The physical principles of magnetism," *The Physical Principles of Magnetism, by Allan H. Morrish, pp. 696. ISBN 0-7803-6029-X. Wiley-VCH, January 2001.*, vol. 1, 2001.

[55] S. Kasap, *Principles of electronic materials and devices*, vol. 81. McGraw-Hill New York, 2006.

[56] D. Jiles, *Introduction to magnetism and magnetic materials*. CRC, 1998.

[57] A. Elster and J. Burdette, *Questions and answers in magnetic resonance imaging*. Mosby, 1994.

[58] M. Leach, "Spatially localized nuclear magnetic resonance," *The Physics of Medical Imaging. Bristol: Institute of Physics Publishing*, pp. 389–487, 1988.

[59] K. H. Bae, Y. B. Kim, Y. Lee, J. Hwang, H. Park, and T. G. Park, "Bioinspired synthesis and characterization of gadolinium-labeled magnetite nanoparticles for dual contrast T1- and T2-weighted magnetic resonance imaging," *Bioconjugate Chemistry*, vol. 21, no. 3, pp. 505–512, 2010.

[60] H. Na, I. Song, and T. Hyeon, "Inorganic nanoparticles for MRI contrast agents," *Advanced Materials*, vol. 21, no. 21, pp. 2133–2148, 2009.

[61] Y. Sheng, Y. Yuan, C. Liu, X. Tao, X. Shan, and F. Xu, "In vitro macrophage uptake and in vivo biodistribution of PLA–PEG nanopar-

ticles loaded with hemoglobin as blood substitutes: effect of PEG content," *Journal of Materials Science: Materials in Medicine*, vol. 20, no. 9, pp. 1881–1891, 2009.

[62] S. Moghimi and J. Szebeni, "Stealth liposomes and long circulating nanoparticles: critical issues in pharmacokinetics, opsonization and protein-binding properties," *Progress in lipid research*, vol. 42, no. 6, pp. 463–478, 2003.

[63] S. Moghimi, A. Hunter, and J. Murray, "Long-circulating and target-specific nanoparticles: theory to practice," *Pharmacological reviews*, vol. 53, no. 2, pp. 283–318, 2001.

[64] W. Mulder, G. Strijkers, J. Habets, E. Bleeker, D. van der Schaft, G. Storm, G. Koning, A. Griffioen, and K. Nicolay, "MR molecular imaging and fluorescence microscopy for identification of activated tumor endothelium using a bimodal lipidic nanoparticle," *The FASEB journal*, vol. 19, no. 14, pp. 2008–2010, 2005.

[65] C. Petre and D. Dittmer, "Liposomal daunorubicin as treatment for kaposis sarcoma," *International journal of nanomedicine*, vol. 2, no. 3, p. 277, 2007.

[66] R. Oude Engberink, S. van der Pol, E. Döpp, H. de Vries, and E. Blezer, "Comparison of SPIO and USPIO for in vitro labelling of human monocytes: MR detection and cell function," *Radiology*, vol. 243, no. 2, p. 467, 2007.

[67] S. Lim, R. Riehn, C. Tung, W. Ryu, R. Zhuo, J. Dalland, and R. Austin, "Upconverting nanophosphors for bioimaging," *Nanotechnology*, vol. 20, p. 405701, 2009.

[68] S. Svenson and D. Tomalia, "Dendrimers in biomedical applications–reflections on the field," *Advanced drug delivery reviews*, vol. 57, no. 15, pp. 2106–2129, 2005.

[69] M. Vicent, "Polymer-drug conjugates as modulators of cellular apoptosis," *The AAPS journal*, vol. 9, no. 2, pp. 200–207, 2007.

[70] M. Flenniken, D. Willits, A. Harmsen, L. Liepold, A. Harmsen, M. Young, and T. Douglas, "Melanoma and lymphocyte cell-specific targeting incorporated into a heat shock protein cage architecture," *Chemistry & biology*, vol. 13, no. 2, pp. 161–170, 2006.

[71] Y. Huang, Y. Lin, Z. Lin, and H. Chang, "Aptamer-modified gold nanoparticles for targeting breast cancer cells through light scattering," *Journal of Nanoparticle Research*, vol. 11, no. 4, pp. 775–783, 2009.

[72] A. Haes and R. Van Duyne, "A nanoscale optical biosensor: sensitivity and selectivity of an approach based on the localized surface plasmon resonance spectroscopy of triangular silver nanoparticles," *Journal of the American Chemical Society*, vol. 124, no. 35, pp. 10596–10604, 2002.

[73] O. Rabin, J. Perez, J. Grimm, G. Wojtkiewicz, and R. Weissleder, "An X-ray computed tomography imaging agent based on long-circulating bismuth sulphide nanoparticles," *Nature Materials*, vol. 5, no. 2, pp. 118–122, 2006.

[74] J. Lewis, G. Destito, A. Zijlstra, M. Gonzalez, J. Quigley, M. Manchester, and H. Stuhlmann, "Viral nanoparticles as tools for intravital vascular imaging," *Nature medicine*, vol. 12, no. 3, pp. 354–360, 2006.

[75] Z. Liu, S. Tabakman, S. Sherlock, X. Li, Z. Chen, K. Jiang, S. Fan, and H. Dai, "Multiplexed five-color molecular imaging of cancer cells and tumor tissues with carbon nanotube raman tags in the near-infrared," *Nano research*, vol. 3, no. 3, pp. 222–233, 2010.

[76] F. Wolf, W. Li, F. Li, and C. Li, "Novel luciferase-based reporter system to monitor activation of ErbB2/Her2/neu pathway noninvasively during radiotherapy," *International Journal of Radiation Oncology* Biology* Physics*, vol. 79, no. 1, pp. 233–238, 2011.

[77] M. Chalfie, Y. Tu, G. Euskirchen, W. Ward, and D. Prasher, "Green fluorescent protein as a marker for gene expression," *Science*, vol. 263, no. 5148, p. 802, 1994.

[78] X. He, K. Wang, and Z. Cheng, "In vivo near-infrared fluorescence imaging of cancer with nanoparticle-based probes," *Wiley Interdisciplinary Reviews: Nanomedicine and Nanobiotechnology*, vol. 2, no. 4, pp. 349–366, 2010.

[79] J. Bünzli, "Lanthanide luminescence for biomedical analyses and imaging.," *Chemical reviews*, vol. 110, no. 5, p. 2729, 2010.

[80] M. Wang, C. Mi, W. Wang, C. Liu, Y. Wu, Z. Xu, C. Mao, and S. Xu, "Immunolabeling and nir-excited fluorescent imaging of hela cells by using NaYF4: Yb, Er upconversion nanoparticles," *ACS nano*, vol. 3, no. 6, pp. 1580–1586, 2009.

[81] T. Soukka, K. Kuningas, T. Rantanen, V. Haaslahti, and T. Lövgren, "Photochemical characterization of up-converting inorganic lanthanide phosphors as potential labels," *Journal of fluorescence*, vol. 15, no. 4, pp. 513–528, 2005.

[82] H. Suzuki, I. Lee, and N. Maeda, "Laser-induced emission from dye-doped nanoparticle aggregates of poly (DL-lactide-co-glycolide)," *Int. J. Phys. Sci*, vol. 3, pp. 42–44, 2008.

[83] K. Yong, "Mn-doped near-infrared quantum dots as multimodal targeted probes for pancreatic cancer imaging," *Nanotechnology*, vol. 20, p. 015102, 2009.

[84] B. Dubertret, P. Skourides, D. Norris, V. Noireaux, A. Brivanlou, and A. Libchaber, "In vivo imaging of quantum dots encapsulated in phospholipid micelles," *Science*, vol. 298, no. 5599, p. 1759, 2002.

[85] C. Leatherdale, W. Woo, F. Mikulec, and M. Bawendi, "On the absorption cross section of CdSe nanocrystal quantum dots," *The Journal of Physical Chemistry B*, vol. 106, no. 31, pp. 7619–7622, 2002.

[86] X. He, J. Gao, S. Gambhir, and Z. Cheng, "Near-infrared fluorescent nanoprobes for cancer molecular imaging: status and challenges," *Trends in Molecular Medicine*, vol. 16, no. 12, pp. 574–583, 2010.

[87] Q. Ma and X. Su, "Near-infrared quantum dots: synthesis, functionalization and analytical applications," *Analyst*, vol. 135, no. 8, pp. 1867–1877, 2010.

[88] S. Päuser, R. Reszka, S. Wagner, K. Wolf, H. Buhr, and G. Berger, "Liposome-encapsulated superparamagnetic iron oxide particles as markers in an MRI-guided search for tumor-specific drug carriers," *Anti-cancer drug design*, vol. 12, no. 2, pp. 125–135, 1997.

[89] X. Shi, S. Wang, S. Swanson, S. Ge, Z. Cao, M. Van Antwerp, K. Landmark, and J. Baker Jr, "Dendrimer-functionalized shell-crosslinked iron oxide nanoparticles for *In-Vivo* magnetic resonance imaging of tumors," *Advanced Materials*, vol. 20, no. 9, pp. 1671–1678, 2008.

[90] C. Alexander, "Cobalt-beer cardiomyopathy: A clinical and pathologic study of twenty-eight cases," *The American journal of medicine*, vol. 53, no. 4, pp. 395–417, 1972.

[91] G. Bernardini, A. Cattaneo, E. Sabbioni, M. Di Gioacchino, M. Chiriva-Internati, and R. Gornati, "Toxicology of engineered metal nanoparticles," *General, Applied and Systems Toxicology*, 2011.

[92] H. Na, I. Lee, H. Seo, Y. Park, J. Lee, S. Kim, and T. Hyeon, "Versatile PEG–derivatized phosphine oxide ligands for water–dispersible metal oxide nanocrystals," *Chemical Communications*, no. 48, pp. 5167–5169, 2007.

[93] J. Lee, Y. Huh, Y. Jun, J. Seo, J. Jang, H. Song, S. Kim, E. Cho, H. Yoon, J. Suh, *et al.*, "Artificially engineered magnetic nanoparticles for ultra-sensitive molecular imaging," *Nature medicine*, vol. 13, no. 1, pp. 95–99, 2006.

[94] C. Bárcena, A. Sra, G. Chaubey, C. Khemtong, J. Liu, and J. Gao, "Zinc ferrite nanoparticles as MRI contrast agents," *Chemical Communications*, no. 19, pp. 2224–2226, 2008.

[95] C. Lam, J. James, R. McCluskey, S. Arepalli, and R. Hunter, "A review of carbon nanotube toxicity and assessment of potential occupational and environmental health risks," *CRC Critical Reviews in Toxicology*, vol. 36, no. 3, pp. 189–217, 2006.

[96] T. Andelman, S. Gordonov, G. Busto, P. Moghe, and R. Riman, "Synthesis and cytotoxicity of Y_2O_3 nanoparticles of various morphologies," *Nanoscale research letters*, vol. 5, no. 2, pp. 263–273, 2010.

[97] S. Cotton, *Lanthanide and actinide chemistry*, vol. 17. John Wiley & Sons, 2006.

[98] J. Chivian, W. Case, and D. Eden, "The photon avalanche: a new phenomenon in Pr^{3+}-based infrared quantum counters," *Applied Physics Letters*, vol. 35, no. 2, p. 124, 1979.

[99] L. Yang, H. Han, Y. Zhang, and J. Zhong, "White emission by frequency up-conversion in Yb^{3+}-Ho^{3+}-Tm^{3+} triply doped hexagonal $NaYF_4$ nanorods," *The Journal of Physical Chemistry C*, vol. 113, no. 44, pp. 18995–18999, 2009.

[100] Z. Hou, Y. Luo, and X. Li, "Cationic rare earth metal alkyls as novel catalysts for olefin polymerization and copolymerization," *Journal of organometallic chemistry*, vol. 691, no. 14, pp. 3114–3121, 2006.

[101] F. Yuan, J. Yang, and L. Xiong, "Lanthanide borohydride complexes with an aryloxide ligand: Synthesis, structural characterization and polymerization activity," *Journal of organometallic chemistry*, vol. 691, no. 11, pp. 2534–2539, 2006.

[102] T. Parac-Vogt, K. Deleersnyder, and K. Binnemans, "Lanthanide (III) tosylates as new acylation catalysts," *European journal of organic chemistry*, vol. 2005, no. 9, pp. 1810–1815, 2005.

[103] M. Oshitani, M. Watada, K. Shodai, and M. Kodama, "Effect of lanthanide oxide additives on the high-temperature charge acceptance characteristics of pasted nickel electrodes," *Journal of the Electrochemical Society*, vol. 148, p. A67, 2001.

[104] A. Polman and F. van Veggel, "Broadband sensitizers for erbium-doped planar optical amplifiers: review," *JOSA B*, vol. 21, no. 5, pp. 871–892, 2004.

[105] R. Reisfeld, "Industrial applications of rare earths in fiber optics, luminescent solar concentrators and lasers," *Inorganica Chimica Acta*, vol. 140, pp. 345–350, 1987.

[106] J. Ballato, J. Lewis, and P. Holloway, "Display applications of rare-earth-doped materials," *MRS Bulletin*, vol. 24, no. 9, pp. 51–56, 1999.

[107] Z. Tian, G. Chen, X. Li, H. Liang, Y. Li, Z. Zhang, and Y. Tian, "Autofluorescence-free in vivo multicolor imaging using upconversion fluoride nanocrystals," *Lasers in Medical Science*, vol. 25, no. 4, pp. 479–484, 2010.

[108] J. Shen, L. Sun, and C. Yan, "Luminescent rare earth nanomaterials for bioprobe applications," *Dalton Trans.*, no. 42, pp. 5687–5697, 2008.

[109] P. Peijzel, A. Meijerink, R. Wegh, M. Reid, and G. Burdick, "A complete *4fn* energy level diagram for all trivalent lanthanide ions," *Journal of solid state chemistry*, vol. 178, no. 2, pp. 448–453, 2005.

[110] D. Johnson, "Principles of lanthanide chemistry," *Journal of Chemical Education*, vol. 57, no. 7, p. 475, 1980.

[111] Z. Liu, F. Kiessling, and J. Gätjens, "Advanced nanomaterials in multimodal imaging: design, functionalization, and biomedical applications," *Journal of Nanomaterials*, vol. 2010, p. 51, 2010.

[112] D. Lee, H. Koo, I. Sun, J. Ryu, K. Kim, and I. Kwon, "Multifunctional nanoparticles for multimodal imaging and theragnosis," *Chem. Soc. Rev.*, 2011.

[113] J. Smith, R. Kontermann, J. Embleton, and S. Kumar, "Antibody phage display technologies with special reference to angiogenesis," *The FASEB journal*, vol. 19, no. 3, p. 331, 2005.

[114] P. Holliger and P. Hudson, "Engineered antibody fragments and the rise of single domains," *Nature biotechnology*, vol. 23, no. 9, pp. 1126–1136, 2005.

[115] K. OHSAWA, T. KASAMATSU, J. NAGASHIMA, K. HANAWA, M. KUWAHARA, H. OZAKI, and H. SAWAI, "Arginine-modified DNA aptamers that show enantioselective recognition of the dicarboxylic acid

moiety of glutamic acid," *Analytical Sciences*, vol. 24, no. 1, pp. 167–172, 2008.

[116] D. Ahmadvand, F. Rahbarizadeh, and S. Moghimi, "Biological targeting and innovative therapeutic interventions with phage-displayed peptides and structured nucleic acids (aptamers)," *Current Opinion in Biotechnology*, 2011.

[117] W. Chen, P. Jarzyna, G. van Tilborg, V. Nguyen, D. Cormode, A. Klink, A. Griffioen, G. Randolph, E. Fisher, W. Mulder, *et al.*, "RGD peptide functionalized and reconstituted high-density lipoprotein nanoparticles as a versatile and multimodal tumor targeting molecular imaging probe," *The FASEB Journal*, vol. 24, no. 6, p. 1689, 2010.

[118] S. Lee, J. Xie, and X. Chen, "Peptide-based probes for targeted molecular imaging," *Biochemistry*, vol. 49, no. 7, pp. 1364–1376, 2010.

[119] R. Schiffelers, A. Ansari, J. Xu, Q. Zhou, Q. Tang, G. Storm, G. Molema, P. Lu, P. Scaria, and M. Woodle, "Cancer siRNA therapy by tumor selective delivery with ligand-targeted sterically stabilized nanoparticle," *Nucleic acids research*, vol. 32, no. 19, pp. e149–e149, 2004.

[120] Y. Xie, W. Lu, and X. Jiang, "Improvement of cationic albumin conjugated pegylated nanoparticles holding NC-1900, a vasopressin fragment analog, in memory deficits induced by scopolamine in mice," *Behavioural brain research*, vol. 173, no. 1, pp. 76–84, 2006.

[121] J. Lutz, H. Börner, and K. Weichenhan, "'click'bioconjugation of a well-defined synthetic polymer and a protein transduction domain," *Australian journal of chemistry*, vol. 60, no. 6, pp. 410–413, 2007.

[122] Z. Krpetic, S. Saleemi, I. Prior, V. See, R. Quershi, and M. Brust, "Negotiation of intracellular membrane barriers by TAT-modified gold nanoparticles," *ACS nano*, 2011.

[123] X. Gao, J. Chen, J. Chen, B. Wu, H. Chen, and X. Jiang, "Quantum dots bearing lectin-functionalized nanoparticles as a platform for *in vivo* brain imaging," *Bioconjugate chemistry*, vol. 19, no. 11, pp. 2189–2195, 2008.

[124] K. Douma, L. Prinzen, D. Slaaf, C. Reutelingsperger, E. Biessen, T. Hackeng, M. Post, and M. van Zandvoort, "Nanoparticles for optical molecular imaging of atherosclerosis," *Small*, vol. 5, no. 5, pp. 544–557, 2009.

[125] F. Jaffer, D. Kim, L. Quinti, C. Tung, E. Aikawa, A. Pande, R. Kohler, G. Shi, P. Libby, and R. Weissleder, "Optical visualization of cathepsin K activity in atherosclerosis with a novel, protease-activatable fluorescence sensor," *Circulation*, vol. 115, no. 17, p. 2292, 2007.

[126] A. Abi-Dargham and M. Laruelle, "*In Vivo* imaging of dopamine receptors," *The Dopamine Receptors*, pp. 399–430, 2010.

[127] D. Hyde, R. de Kleine, S. MacLaurin, E. Miller, D. Brooks, T. Krucker, and V. Ntziachristos, "Hybrid FMT-CT imaging of amyloid-beta plaques in a murine Alzheimer's disease model," *Neuroimage*, vol. 44, no. 4, pp. 1304–1311, 2009.

[128] M. Okumura, R. Arakawa, H. Ito, C. Seki, H. Takahashi, H. Takano, E. Haneda, R. Nakao, H. Suzuki, K. Suzuki, *et al.*, "Quantitative analysis of NK1 receptor in the human brain using PET with 18F-FE-SPA-RQ," *Journal of Nuclear Medicine*, vol. 49, no. 11, p. 1749, 2008.

[129] I. Tomlinson, J. Mason, R. Blakely, and S. Rosenthal, "High affinity inhibitors of the dopamine transporter (DAT): novel biotinylated ligands for conjugation to quantum dots," *Bioorganic & medicinal chemistry letters*, vol. 16, no. 17, pp. 4664–4667, 2006.

[130] J. Desgrosellier and D. Cheresh, "Integrins in cancer: biological implications and therapeutic opportunities," *Nature Reviews Cancer*, vol. 10, no. 1, pp. 9–22, 2010.

[131] L. Peng, R. Liu, J. Marik, X. Wang, Y. Takada, and K. Lam, "Combinatorial chemistry identifies high-affinity peptidomimetics against $\alpha 4\beta 1$ integrin for *in vivo* tumor imaging," *Nature Chemical Biology*, vol. 2, no. 7, pp. 381–389, 2006.

[132] H. Jin and J. Varner, "Integrins: roles in cancer development and as treatment targets," *British journal of cancer*, vol. 90, no. 3, pp. 561–565, 2004.

[133] J. Stouwdam and F. van Veggel, "Near-infrared emission of redispersible Er^{3+}, Nd^{3+}, and Ho^{3+} doped LaF_3 nanoparticles," *Nano letters*, vol. 2, no. 7, pp. 733–737, 2002.

[134] F. Wang, D. Chatterjee, Z. Li, Y. Zhang, X. Fan, and M. Wang, "Synthesis of polyethylenimine/$NaYF_4$ nanoparticles with upconversion fluorescence," *Nanotechnology*, vol. 17, p. 5786, 2006.

[135] F. Wang and X. Liu, "Upconversion multicolor fine-tuning: Visible to near-infrared emission from lanthanide-doped $NaYF_4$ nanoparticles," *Journal of the American Chemical Society*, vol. 130, no. 17, pp. 5642–5643, 2008.

[136] Y. Park, J. Kim, K. Lee, K. Jeon, H. Na, J. Yu, H. Kim, N. Lee, S. Choi, S. Baik, *et al.*, "Nonblinking and nonbleaching upconverting nanoparticles as an optical imaging nanoprobe and T1 magnetic resonance imaging contrast agent," *Advanced Materials*, vol. 21, no. 44, pp. 4467–4471, 2009.

[137] F. Zhang, J. Li, J. Shan, L. Xu, and D. Zhao, "Shape, size, and phase-controlled rare-earth fluoride nanocrystals with optical up-conversion properties," *Chemistry-A European Journal*, vol. 15, no. 41, pp. 11010–11019, 2009.

[138] X. Liu, J. Zhao, Y. Sun, K. Song, Y. Yu, C. Du, X. Kong, and H. Zhang, "Ionothermal synthesis of hexagonal-phase $NaYF_4$: Yb^{3+}, Er^{3+}/Tm^{3+} upconversion nanophosphors," *Chemical Communications*, no. 43, pp. 6628–6630, 2009.

[139] V. Venkatramu, D. Falcomer, A. Speghini, M. Bettinelli, and C. Jayasankar, "Synthesis and luminescence properties of Er^{3+}-doped $Lu_3Ga_5O_{12}$ nanocrystals," *Journal of Luminescence*, vol. 128, no. 5-6, pp. 811–813, 2008.

[140] Y. Liu, C. Xu, and Q. Yang, "White upconversion of rare-earth doped ZnO nanocrystals and its dependence on size of crystal particles and content of Yb^{3+} and Tm^{3+}," *Journal of Applied Physics*, vol. 105, no. 8, pp. 084701–084701, 2009.

[141] H. Han, L. Yang, Y. Liu, Y. Zhang, and Q. Yang, "Up-conversion luminescence switching in Er^{3+}-containing ZnO nanoparticles through Li^+ co-doping," *Optical Materials*, vol. 31, no. 2, pp. 338–341, 2008.

[142] R. Martín-Rodríguez, R. Valiente, C. Pesquera, F. González, C. Blanco, V. Potin, and M. Marco de Lucas, "Optical properties of nanocrystalline-coated Y_2O_3: Er^{3+}, Yb^{3+} obtained by mechano-chemical and combustion synthesis," *Journal of Luminescence*, vol. 129, no. 9, pp. 1109–1114, 2009.

[143] W. Kong, J. Shan, and Y. Ju, "Flame synthesis and effects of host materials on Yb^{3+}/Er^{3+} co-doped upconversion nanophosphors," *Materials Letters*, vol. 64, no. 6, pp. 688–691, 2010.

[144] J. Li, X. Li, X. Sun, and T. Ishigaki, "Monodispersed colloidal spheres for uniform Y_2O_3: Eu^{3+} red-phosphor particles and greatly enhanced luminescence by simultaneous Gd^{3+} doping," *The Journal of Physical Chemistry C*, vol. 112, no. 31, pp. 11707–11716, 2008.

[145] H. Willard and N. Tang, "A study of the precipitation of aluminum basic sulfate by urea," *Journal of the American Chemical Society*, vol. 59, no. 7, pp. 1190–1196, 1937.

[146] M. Salutsky and L. Quill, "The rare earth metals and their compounds. XII. carbonates of lanthanum, neodymium and samarium," *Journal of the American Chemical Society*, vol. 72, no. 7, pp. 3306–3307, 1950.

[147] E. Matijevic, "Production of monodispersed colloidal particles," *Annual Review of Materials Science*, vol. 15, no. 1, pp. 483–516, 1985.

[148] E. Matijevic, "Preparation and properties of uniform size colloids," *Chemistry of materials*, vol. 5, no. 4, pp. 412–426, 1993.

[149] Y. Xia, B. Gates, Y. Yin, and Y. Lu, "Monodispersed colloidal spheres: old materials with new applications," *Advanced Materials*, vol. 12, no. 10, pp. 693–713, 2000.

[150] S. Sohn, Y. Kwon, Y. Kim, and D. Kim, "Synthesis and characterization of near-monodisperse yttria particles by homogeneous precipitation method," *Powder technology*, vol. 142, no. 2-3, pp. 136–153, 2004.

[151] J. Li, X. Li, X. Sun, T. Ikegami, and T. Ishigaki, "Uniform colloidal spheres for $(Y_{1-x}$ Gd $_x)_2O_3$ (x= 0–1): Formation mechanism, compositional impacts, and physicochemical properties of the oxides," *Chemistry of Materials*, vol. 20, no. 6, pp. 2274–2281, 2008.

[152] M. Xing, W. Cao, T. Pang, and X. Ling, "Synthesis of monodisperse spherical Y_2O_2S: Yb, Ho upconversion nanoparticles," *Solid State Communications*, vol. 149, no. 23-24, pp. 911–914, 2009.

[153] T. Sugimoto, "Preparation of monodispersed colloidal particles," *Advances in Colloid and Interface Science*, vol. 28, pp. 65–108, 1987.

[154] T. Zako, H. Nagata, N. Terada, M. Sakono, K. Soga, and M. Maeda, "Improvement of dispersion stability and characterization of upconversion nanophosphors covalently modified with PEG as a fluorescence bioimaging probe," *Journal of Materials Science*, vol. 43, no. 15, pp. 5325–5330, 2008.

[155] S. Tanuma, C. Powell, and D. Penn, "Proposed formula for electron inelastic mean free paths based on calculations for 31 materials," *Surface Science*, vol. 192, no. 1, pp. L849–L857, 1987.

[156] H. Sheua, W. Shiha, W. Chuanga, I. Lib, and C. Yehb, "Crystal structure and phase transitions of Gd (CO_3) OH studied by synchrotron powder diffraction," *Journal of the Chinese Chemical Society*, vol. 57, no. 4B, pp. 938–945, 2010.

[157] Y. Lei, H. Song, L. Yang, L. Yu, Z. Liu, G. Pan, X. Bai, and L. Fan, "Upconversion luminescence, intensity saturation effect, and thermal effect in Gd_2O_3: Er^{3+}, Yb^{3+} nanowires," *The Journal of chemical physics*, vol. 123, p. 174710, 2005.

[158] Z. Heiba, L. Arda, and Y. Hascicek, "Structure and microstructure characterization of the mixed sesquioxides $(Gd_{1-x}Yb_x)_2O_3$ and $(Gd_{1-x}H_{ox})_2O_3$ prepared by sol-gel process," *Journal of applied crystallography*, vol. 38, no. 2, pp. 306–310, 2005.

[159] F. Vetrone, J. Boyer, J. Capobianco, A. Speghini, and M. Bettinelli, "Concentration-dependent near-infrared to visible upconversion in nanocrystalline and bulk y2o3: Er3+," *Chemistry of materials*, vol. 15, no. 14, pp. 2737–2743, 2003.

[160] J. Bünzli and S. Eliseeva, "Basics of lanthanide photophysics," *Lanthanide Luminescence*, pp. 1–45, 2011.

[161] G. Liu and B. Jacquier, *Spectroscopic properties of rare earths in optical materials*, vol. 83. Springer, 2005.

[162] M. Digonnet, *Rare-Earth-Doped Fiber Lasers and Amplifiers, Revised and Expanded*. CRC, 2001.

[163] Q. Zhan, J. Qian, H. Liang, G. Somesfalean, D. Wang, S. He, Z. Zhang, and S. Andersson-Engels, "Using 915-nm laser excited $Tm^{3+}/Er^{3+}/Ho^{3+}$ doped $NaYbF_4$ upconversion nanoparticles for in vitro and deeper in vivo bioimaging without overheating irradiation," *ACS nano*, 2011.

[164] M. Fortin, R. Petoral Jr, F. Söderlind, A. Klasson, M. Engström, T. Veres, P. Käll, and K. Uvdal, "Polyethylene glycol-covered ultra-small Gd_2O_3 nanoparticles for positive contrast at 1.5 T magnetic resonance clinical scanning," *Nanotechnology*, vol. 18, p. 395501, 2007.

[165] M. Ahrn, L. Selegrd, A. Klasson, F. Sderlind, N. Abrikossova, C. Skoglund, T. Bengtsson, M. Engstrm, P. Kll, and K. Uvdal, "Synthesis and characterization of PEGylated Gd_2O_3 nanoparticles for MRI contrast enhancement," *Langmuir*, vol. 26, no. 8, pp. 5753–5762, 2010.

[166] W. Jenks, S. Sadeghi, *et al.*, "SQUIDs for nondestructive evaluation," *Journal of Physics D: Applied Physics*, vol. 30, p. 293, 1997.

[167] S. Singh, K. Kumar, M. Srivastava, D. Rai, and S. Rai, "Magnetic-field-induced optical bistability in multifunctional Gd_2O_3: Er^{3+},Yb^{3+} upconversion nanophosphor," *Optics Letters*, vol. 35, no. 10, pp. 1575–1577, 2010.

[168] L. Abelmann, "Principle of magnetic force microscopy," 2005.

[169] K. Braun, S. Sievers, D. Eberbeck, S. Gustafsson, E. Olsson, H. Schumacher, and U. Siegner, "Quantitative measurement of the magnetic moment of an individual magnetic nanoparticle by magnetic force microscopy," *Arxiv preprint arXiv:1002.3739*, 2010.

[170] A. Rao, M. Schoenenberger, E. Gnecco, T. Glatzel, E. Meyer, D. Brändlin, and L. Scandella, "Characterization of nanoparticles using atomic force microscopy," in *Journal of Physics: Conference Series*, vol. 61, p. 971, IOP Publishing, 2007.

[171] T. Zako, H. Nagata, N. Terada, A. Utsumi, M. Sakono, M. Yohda, H. Ueda, K. Soga, and M. Maeda, "Cyclic RGD peptide-labeled upconversion nanophosphors for tumor cell-targeted imaging," *Biochemical and biophysical research communications*, vol. 381, no. 1, pp. 54–58, 2009.

[172] L. Xiong, Z. Chen, Q. Tian, T. Cao, C. Xu, and F. Li, "High contrast upconversion luminescence targeted imaging *in vivo* using peptide-labeled nanophosphors," *Analytical chemistry*, vol. 81, no. 21, pp. 8687–8694, 2009.

[173] S. Wu, G. Han, D. Milliron, S. Aloni, V. Altoe, D. Talapin, B. Cohen, and P. Schuck, "Non-blinking and photostable upconverted luminescence from single lanthanide-doped nanocrystals," *Proceedings of the National Academy of Sciences*, vol. 106, no. 27, pp. 10917–10921, 2009.

[174] S. Hilderbrand, F. Shao, C. Salthouse, U. Mahmood, and R. Weissleder, "Upconverting luminescent nanomaterials: application to *in vivo* bioimaging," *Chemical Communications*, no. 28, pp. 4188–4190, 2009.

[175] A. Popov, A. Bykov, V. Sokolov, Y. Lysak, A. Nadort, A. Priezzhev, R. Myllylä, and A. Zvyagin, "Upconversion luminophores as a novel tool for deep tissue imaging," in *European Conference on Biomedical Optics*, Optical Society of America, 2011.

[176] S. Nagarajan and Y. Zhang, "Upconversion fluorescent nanoparticles as a potential tool for in-depth imaging," *Nanotechnology*, vol. 22, p. 395101, 2011.

[177] F. Danhier, O. Feron, and V. Préat, "To exploit the tumor microenvironment: Passive and active tumor targeting of nanocarriers for anti-cancer drug delivery," *Journal of Controlled Release*, vol. 148, no. 2, pp. 135–146, 2010.

[178] F. Danhier, B. Ucakar, N. Magotteaux, M. Brewster, and V. Préat, "Active and passive tumor targeting of a novel poorly soluble cyclin dependent kinase inhibitor, JNJ-7706621," *International journal of pharmaceutics*, vol. 392, no. 1, pp. 20–28, 2010.

[179] D. Chatterjee, A. Rufaihah, and Y. Zhang, "Upconversion fluorescence imaging of cells and small animals using lanthanide doped nanocrystals," *Biomaterials*, vol. 29, no. 7, pp. 937–943, 2008.

[180] C. Salthouse, S. Hildebrand, R. Weissleder, and U. Mahmood, "Design and demonstration of a small-animal up-conversion imager," *Optics express*, vol. 16, no. 26, p. 21731, 2008.

[181] S. Elahi and T. Wang, "Future and advances in endoscopy," *Journal of Biophotonics*, 2011.

[182] M. Goetz and T. Wang, "Molecular imaging in gastrointestinal endoscopy," *Gastroenterology*, vol. 138, no. 3, pp. 828–833, 2010.

[183] A. Elsaesser and C. Howard, "Toxicology of nanoparticles," *Advanced Drug Delivery Reviews*, 2011.

[184] T. Cedervall, I. Lynch, S. Lindman, T. Berggård, E. Thulin, H. Nilsson, K. Dawson, and S. Linse, "Understanding the nanoparticle–protein corona using methods to quantify exchange rates and affinities of proteins for nanoparticles," *Proceedings of the National Academy of Sciences*, vol. 104, no. 7, p. 2050, 2007.

[185] M. Al-Rawi, S. Diabaté, and C. Weiss, "Uptake and intracellular localization of submicron and nano-sized SiO_2 particles in HeLa cells," *Archives of toxicology*, vol. 85, no. 7, pp. 813–826, 2011.

[186] K. Yamashita, Y. Yoshioka, K. Higashisaka, K. Mimura, Y. Morishita, M. Nozaki, T. Yoshida, T. Ogura, H. Nabeshi, K. Nagano, *et al.*, "Silica and titanium dioxide nanoparticles cause pregnancy complications in mice," *Nature nanotechnology*, vol. 6, no. 5, pp. 321–328, 2011.

[187] L. Xiong, T. Yang, Y. Yang, C. Xu, and F. Li, "Long-term *in vivo* biodistribution imaging and toxicity of polyacrylic acid-coated upconversion nanophosphors," *Biomaterials*, vol. 31, no. 27, pp. 7078–7085, 2010.